

# Competition of shape and interaction patchiness for self-assembling nanoplates

Xingchen Ye<sup>1†</sup>, Jun Chen<sup>2†</sup>, Michael Engel<sup>4†</sup>, Jaime A. Millan<sup>5†</sup>, Wenbin Li<sup>6</sup>, Liang Qi<sup>7</sup>, Guozhong Xing<sup>3</sup>, Joshua E. Collins<sup>8</sup>, Cherie R. Kagan<sup>1,2,3</sup>, Ju Li<sup>6,7</sup>, Sharon C. Glotzer<sup>4,5\*</sup> and Christopher B. Murray<sup>1,2\*</sup>

**Progress in nanocrystal synthesis and self-assembly enables the formation of highly ordered superlattices. Recent studies focused on spherical particles with tunable attraction and polyhedral particles with anisotropic shape, and excluded volume repulsion, but the effects of shape on particle interaction are only starting to be exploited. Here we present a joint experimental-computational multiscale investigation of a class of highly faceted planar lanthanide fluoride nanocrystals (nanoplates, nanoplatelets). The nanoplates self-assemble into long-range ordered tilings at the liquid-air interface formed by a hexane wetting layer. Using Monte Carlo simulation, we demonstrate that their assembly can be understood from maximization of packing density only in a first approximation. Explaining the full phase behaviour requires an understanding of nanoplate-edge interactions, which originate from the atomic structure, as confirmed by density functional theory calculations. Despite the apparent simplicity in particle geometry, the combination of shape-induced entropic and edge-specific energetic effects directs the formation and stabilization of unconventional long-range ordered assemblies not attainable otherwise.**

Nanocrystals often exhibit well-defined facets that result in a three-dimensional (3D) polyhedral shape<sup>1–5</sup> or, if crystal growth is suppressed in one direction, in a polygonal two-dimensional (2D) shape<sup>4–7</sup>. The assembly of such faceted particles is dominated by driving forces that maximize face-to-face (or, in 2D, edge-to-edge) contact, which is both energetically and entropically favoured. Similar to crystals of spherical colloids dominated by interparticle interactions<sup>8–13</sup>, even perfectly hard nanocrystals can order without explicit attractive interactions at high-enough densities<sup>14–24</sup>; recent simulations predict a rich diversity of entropically stabilized nanocrystal superlattices<sup>25</sup>.

Inherent attractive forces between nanocrystals can add further complexity to their assembly. To grow and stabilize nanocrystals in solution, they are coated with ligand molecules<sup>6,7</sup>, which interact via hydrocarbon chains to generate an effective attraction between the nanocrystals. As crystallographically distinct facets and edges have different atomic structure and density of cationic sites, they can have different densities of ligand molecules and therefore different strength and range of interactions with other facets and edges. Such patchiness of the ligand shell was observed with DNA surface-bound ligands on gold nanoprisms<sup>26,27</sup> and with oleic acid on PbSe nanocrystals<sup>28</sup>, but is not yet exploited for the self-assembly of nanocrystal superlattices.

The delicate balance between entropic and energetic effects in complex self-assembly processes was highlighted in systems of supramolecular rhombi adsorbed on graphite<sup>29–31</sup>. In a similar fashion, complex crystalline assemblies should also be obtainable on a larger scale through rational and predictive design by combining entropic and interaction patchiness made possible by the unique shape of nanocrystals. As a demonstration of this fundamental principle,

we investigated the spontaneous organization of nanoplates into planar superstructures in a hexane wetting layer at the liquid-air interface. We chose lanthanide fluoride (LnF<sub>3</sub>) nanocrystals as model systems because of their diverse anisotropic crystal structures and recent advances in the synthesis of LnF<sub>3</sub> nanomaterials<sup>4,6,32</sup>. A systematic study of nanocrystal growth reveals a correlation between nanocrystal phase stability and lanthanide contraction, which yields a series of monodisperse faceted nanocrystals that include circular, rhombic and irregular hexagonal plates, as well as tetragonal bipyramids. We demonstrate that the rhombic and irregular hexagonal nanoplates represent a fascinating class of planar nanotiles that exhibit rich and subtle phase behaviour.

## Results and discussion

**Synthesis.** Nanocrystals were synthesized by rapid thermal decomposition of lanthanide trifluoroacetate precursors in the presence of oleic acid as a colloidal stabilizer (Fig. 1a). The choice of lanthanide elements and the addition of lithium trifluoroacetate or LiF salts control the nanocrystal composition and the evolution of nanocrystal shape. For lighter Ln<sup>3+</sup> ions (from La to Sm) with larger ionic radii, LnF<sub>3</sub> nanocrystals adopt the trigonal tysonite structure and produce circular nanoplates (Fig. 1d and Supplementary Figs S1 and S2). However, for heavier Ln<sup>3+</sup> ions (from Er to Lu), LiLnF<sub>4</sub> (tetragonal scheelite structure) nanocrystals with a tetragonal-bipyramidal shape are formed (Supplementary Figs S3 and S4). In the middle of the lanthanide series (Ln = Eu–Dy), irregular hexagonal nanoplates with the orthorhombic β-YF<sub>3</sub> structure (space group *Pnma*) are produced, as confirmed by powder X-ray diffraction (XRD) patterns (Fig. 1c and Supplementary Figs S5–S15). High-resolution transmission

<sup>1</sup>Department of Chemistry, University of Pennsylvania, Philadelphia, Pennsylvania 19104, USA, <sup>2</sup>Department of Materials Science and Engineering, University of Pennsylvania, Philadelphia, Pennsylvania 19104, USA, <sup>3</sup>Department of Electrical and Systems Engineering, University of Pennsylvania, Philadelphia, Pennsylvania 19104, USA, <sup>4</sup>Department of Chemical Engineering, University of Michigan, Ann Arbor, Michigan 48109, USA, <sup>5</sup>Department of Materials Science and Engineering, University of Michigan, Ann Arbor, Michigan 48109, USA, <sup>6</sup>Department of Materials Science and Engineering, Massachusetts Institute of Technology, Cambridge, Massachusetts, 02139, USA, <sup>7</sup>Department of Nuclear Science and Engineering, Massachusetts Institute of Technology, Cambridge, Massachusetts, 02139, USA, <sup>8</sup>Intelligent Material Solutions, Inc., Princeton, New Jersey 08540, USA; <sup>†</sup>These authors contributed equally to this work. \*e-mail: sglotzer@umich.edu; cbmurray@sas.upenn.edu

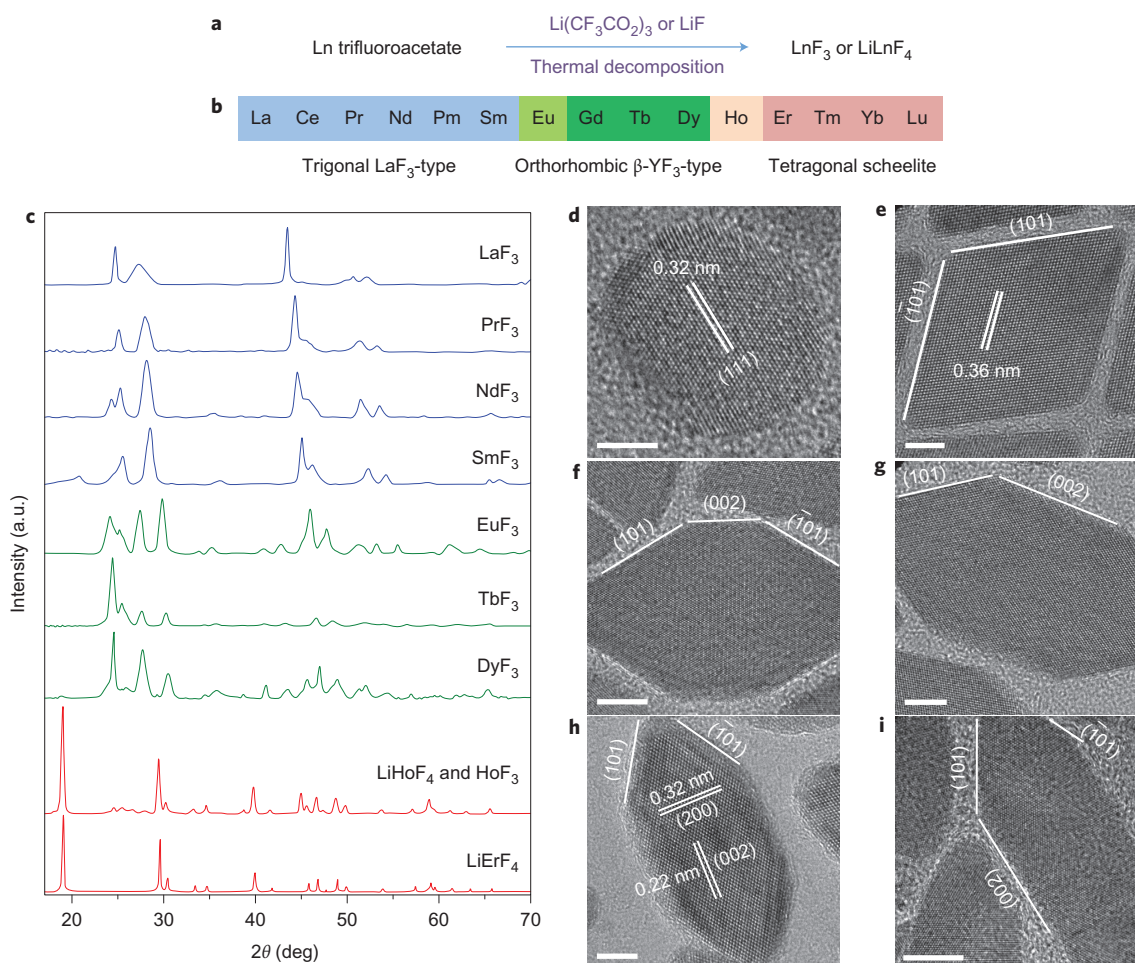


**Figure 1 | Synthesis and structural characterization of monodisperse lanthanide fluoride nanocrystals.** **a**, Schematic representation of the synthesis method. **b**, General trend of stable phases from trigonal  $\text{LnF}_3$  to orthorhombic  $\text{LnF}_3$  and to tetragonal  $\text{LiLnF}_4$  phases as a function of the type of lanthanide ions. Experimental results for  $\text{Eu}^{3+}$  and  $\text{Ho}^{3+}$  show the possibility of coexisting phases. **c**, Powder XRD patterns of different  $\text{LnF}_3$  and  $\text{LiLnF}_4$  nanocrystals. **d-i**, HRTEM images of  $\text{NdF}_3$  (**d**),  $\text{DyF}_3$  (**e**),  $\text{TbF}_3$  (**f**),  $\text{TbF}_3$  (**g**),  $\text{DyF}_3$  (**h**) and  $\text{EuF}_3$  (**i**) nanoplates. Scale bars (**d**), (**e**), (**h**), 5 nm; (**f**), (**g**), (**i**), 10 nm.

electron microscopy (HRTEM) images show that each nanoplate comprises four symmetry-equivalent edges ( $\{101\}$  facets) at the tips with an apex angle of  $68^\circ \pm 0.5^\circ$ , separated by two  $\{002\}$  side facets in the middle (Fig. 1f–i). The plate shape was further confirmed by HRTEM images of nanoplates standing edge-on (Supplementary Fig. S9). The  $\text{Ln}^{3+}$  ions dominated the  $\{010\}$  planes and therefore we postulate that nanocrystal growth along the  $\langle 010 \rangle$  direction was retarded because of the oleic acid coordination of lanthanide cations, which gave rise to the plate morphology. Although systems of four-sided rhombs in supramolecular tilings<sup>29–31</sup> and polymeric platelets fabricated by photolithography<sup>33</sup> have been studied before, the irregular six-sided geometry of  $\text{LnF}_3$  nanoplates has not yet been reported. Our results overlap with these works only in the boundary case of the  $68^\circ$  rhomb (Fig. 1e).

The lateral dimensions of the irregular hexagonal nanoplates can be adjusted by the choice of lanthanide elements and nanocrystal growth conditions, with the plate thickness kept between 4.5 and 7.0 nm. The lanthanide contraction determines the lanthanide fluoride phase stability: lighter  $\text{Ln}^{3+}$  ions with larger ionic radii favour a higher coordination number, as evidenced by the eleven fluoride ions that surround each  $\text{Ln}^{3+}$  ion in the trigonal  $\text{LaF}_3$ -type structure. As the atomic number of the lanthanide increases, crystal structures that feature lower coordination numbers of nine (orthorhombic  $\beta\text{-YF}_3$  type) or eight (tetragonal  $\text{LiYF}_4$  type) dominate<sup>34</sup>, which reflects the effect of cation size and polarizability<sup>32</sup>.

**Interfacial self-assembly.** To study the shape-directed packing behaviour of nanoplates, an interfacial assembly strategy was employed<sup>4,35</sup>. The viscous polar ethylene glycol subphase provided individual nanoplates of sufficient mobility, even at high particle-volume fractions, to anneal out defects and access thermodynamically stable assemblies over extended areas. Face-to-face stacked superstructures are observed in many plate-like colloids<sup>2,6,7,36,37</sup> and are often rationalized on the basis of maximization of local packing fraction and van der Waals interactions between neighbouring plates. In this work, the nanoplate concentration in the spreading solution was adjusted carefully to ensure that uniform planar 2D superstructures dominated (Supplementary Fig. S16). The as-synthesized nanoplates were subjected to several rounds of purification steps using a solvent/non-solvent combination to minimize the amount of free oleic acid molecules that may act as depletants and induce lamellar face-to-face stacking during self-assembly.

A library of 2D superlattices self-assembled from rhombic and irregular hexagonal nanoplates of different aspect ratios is shown in Fig. 2. For rhombic nanoplates, the superlattices display  $cm\bar{m}$  symmetry as manifested by the small-angle electron-diffraction pattern (Fig. 2a and Supplementary Fig. S17). The clear-cut edges allow the nanoplates to be crystallographically registered in the superlattices, as confirmed by the bright spots in the wide-angle electron-diffraction pattern that arises from the periodicity of

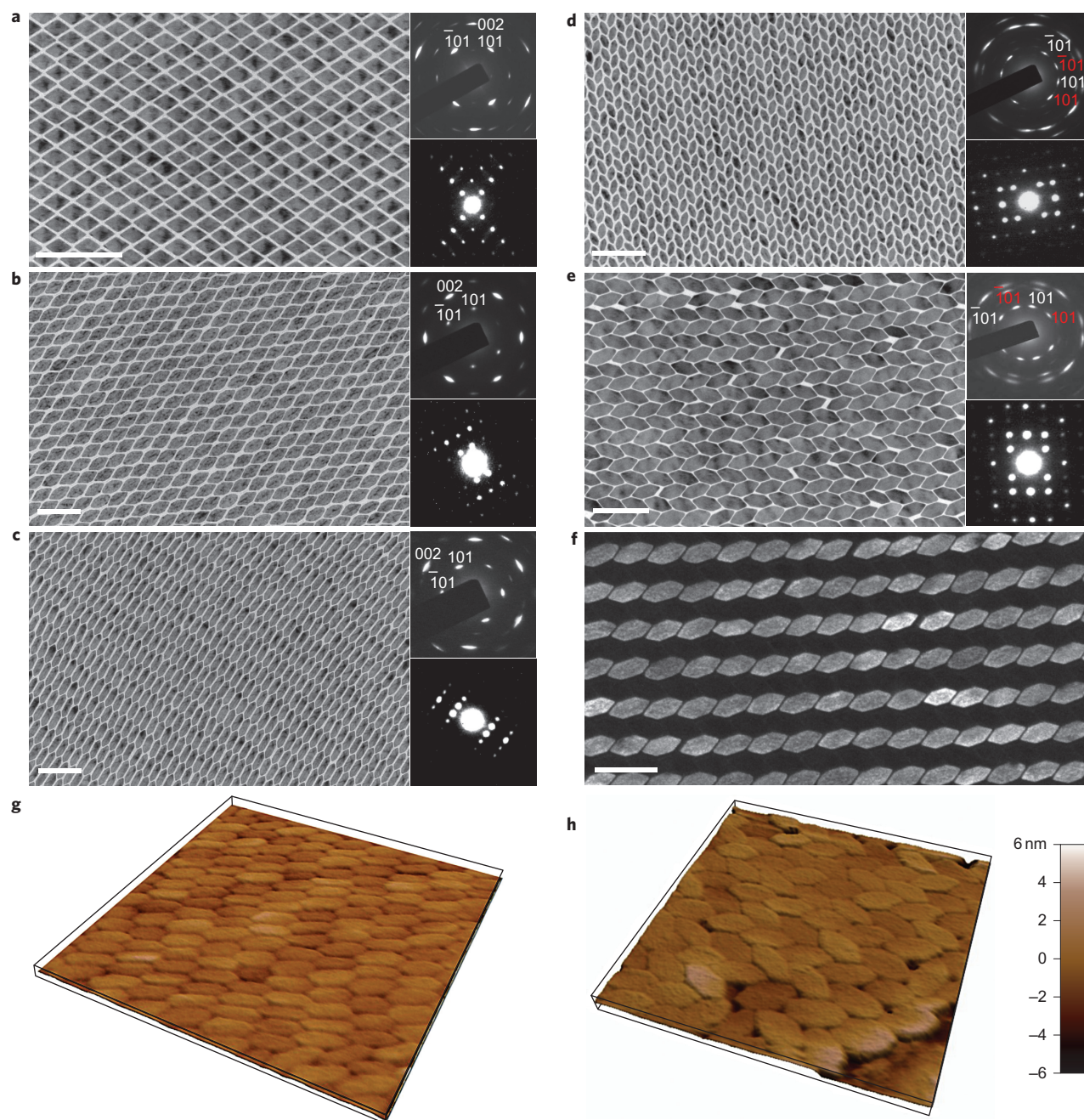


**Figure 2 | 2D superlattices self-assembled from lanthanide fluoride nanoplates. a–c,** Parallel arrangements of DyF<sub>3</sub> rhombohedral nanoplates (a), small aspect ratio TbF<sub>3</sub> hexagonal nanoplates (b) and EuF<sub>3</sub> large aspect ratio hexagonal nanoplates (c). **d,e,** Alternating arrangements of intermediate aspect ratio hexagonal nanoplates of composition DyF<sub>3</sub> (d) and TbF<sub>3</sub> (e); for each, TEM images are shown on the left, and wide-angle and small-angle (upper right and lower right, respectively) electron-diffraction patterns. **f,** Dark-field TEM image of the same area as shown in (e). Scale bars, **a–f,** 100 nm. **g,h,** AFM 3D topography images of EuF<sub>3</sub> (g) and TbF<sub>3</sub> (h) nanoplate superlattices. The scan sizes are 450 nm × 450 nm (g) and 500 nm × 500 nm (h).

atomic lattice planes. Moreover, point defects or stacking faults are commonly seen in the rhombic nanoplate superlattice (Supplementary Fig. S34), which was predicted by simulations of random rhombus tiling<sup>31,38</sup>, and observed experimentally in molecular rhombus tilings<sup>29</sup>. Further symmetry breaking of the nanoplate's shape anisotropy from rhombus to irregular hexagon offers dramatic packing precision. For nanoplates with either a short or long middle segment ( $\{002\}$  side facets) relative to the tip dimension ( $\{101\}$  side facets), we observed only a parallel arrangement in which nanoplates pack densely and preferentially align along their  $[100]$  axis (Fig. 2b,c,g and Supplementary Figs S18–S21).

However, for nanoplates with an intermediate middle segment, a striking alternating arrangement that resembles a herringbone packing occurred exclusively. Examples are DyF<sub>3</sub> and TbF<sub>3</sub> nanoplates that are similar in aspect ratio but differ in overall dimensions (Fig. 2d,e,h and Supplementary Figs S22–S25). The simultaneous in-plane positional and orientational ordering of the irregular hexagonal nanoplate superlattices is also reflected in the corresponding electron-diffraction patterns and, more remarkably, in the dark-field TEM image of the TbF<sub>3</sub> nanoplate superlattice, in which only one set of evenly spaced linear chains of orientationally invariant nanoplates is visible (Fig. 2f). Therefore, unprecedented control

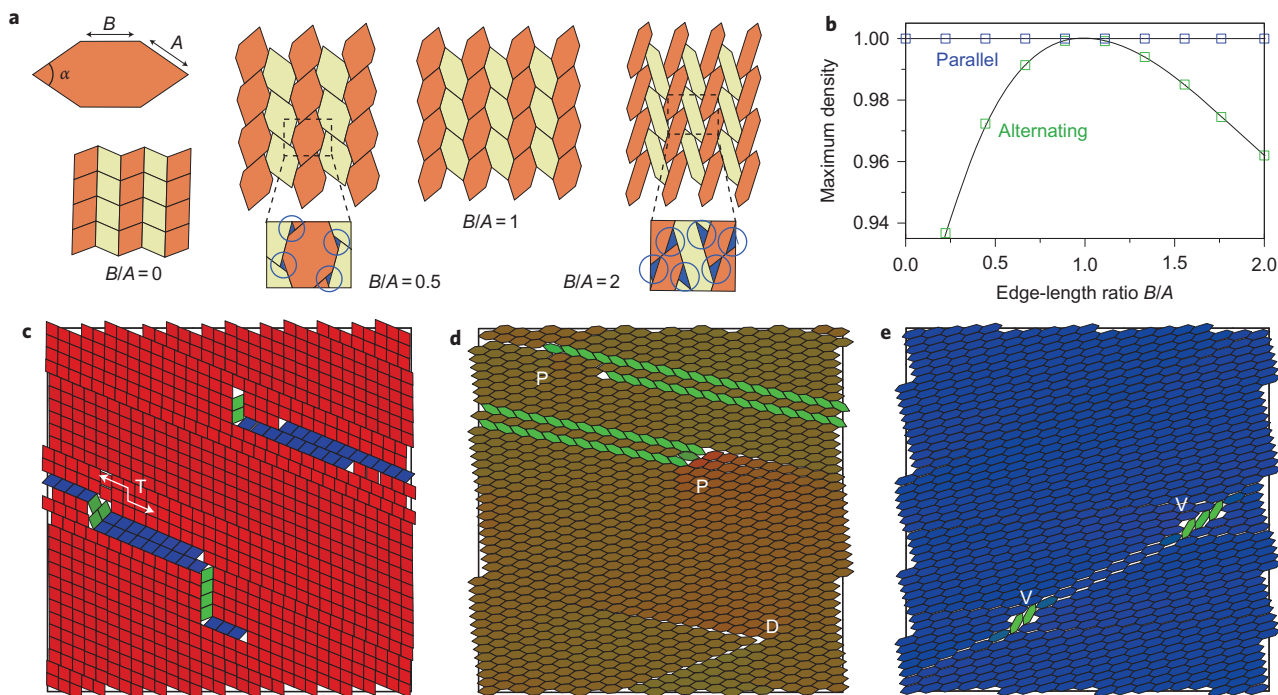


**Figure 3 | Monte Carlo simulations of hard polygonal plates.** **a**, The geometry of the particles is characterized by the opening angle  $\alpha = 68^\circ$  and the two edge lengths  $A$  and  $B$  parallel to (101) and (001), respectively. **b**, Alternating arrangements are only space filling for  $B/A = 0$  and  $B/A = 1$ , and otherwise have voids. This is apparent in the densest packings as a function of the aspect ratio. Parallel arrangements are always space filling. **c–e**, Final particle configurations assembled in simulation from disordered starting configurations. Simulation conditions mimic experimental conditions for nanoplate assembly. The particles assemble into the parallel arrangement for all choices of the edge ratio; shown are  $B/A = 0$  (**c**),  $B/A = 1$  (**d**) and  $B/A = 2$  (**e**). Owing to the periodic boundary conditions, structural defects in the form of twin layer (T), partial dislocations (P), dislocation (D) and vacancies (V) remained in the system. Similar defects are also frequently observed in experiments.

over shape monodispersity of the  $\text{LnF}_3$  nanoplates provided a unique opportunity to apply shape anisotropy for directing assembly along a preferred pathway.

**Monte Carlo simulation of hard plates.** To identify the physical mechanism that drives the assembly, we performed Monte Carlo computer simulations of nanoplates constrained to a 2D plane. Such a constraint mimics the experimental conditions during the final stage of the hexane-evaporation process, which we interpret as follows. A thin layer of hexane on top of the ethylene glycol solubilizes the nanoplates before the hexane is dried completely. When the thickness of the hexane layer as it evaporates becomes comparable to the largest dimension of an individual nanoplate, the plates are forced to orient horizontally. As the nanoplates do not clump together face-to-face (maximizing contact) prior to the formation of a single layer, there are probably no strong attractions between them. Only when the hexane layer evaporates further and pushes the nanoplates together are they close enough for their tethers (oleic acid ligands) to interact strongly. This picture is supported by the observation that when the nanoplate concentration is increased in the spreading solution, lamellar face-to-face stacking becomes the dominant structure (Supplementary Fig. S16).

The geometry of the nanoplates is an elongated hexagon characterized by two parameters, the opening angle  $\alpha$  and the edge-length ratio  $B/A$  (Fig. 3a). Although the angle is fixed to  $\alpha = 68^\circ$  by the crystallographic relationships among the nanocrystal facets in the orthorhombic  $\text{LnF}_3$  structure, the edge-length ratio can be varied from a degenerate rhomb ( $B/A = 0$ ) to the equilateral elongated hexagon ( $B/A = 1$ ) and a strongly elongated hexagon ( $B/A = 2$ ) through the choice of lanthanide elements and nanocrystal growth conditions.

To a first approximation, we considered plates without interaction except excluded volume effects. Hard-particle systems maximize entropy during equilibration at constant volume. In the limit of high pressure the plates maximized packing, because the pressure term dominated the entropy term in the Gibbs free energy. Although elongated hexagons can fill space for all aspect ratios, the tilings were not always unique. Two candidate structures competed. For all values of  $B/A$ , the parallel arrangement was space filling. Alternating arrangements were space filling only for  $B/A = 0$  and  $B/A = 1$  with relative particle rotations of  $\alpha$  and  $\alpha/2$ , respectively. For other edge-length ratios, small voids remained between the plates (Fig. 3a,b).

We simulated the self-assembly of hard elongated hexagons by slowly compressing the disordered fluid. The compression was chosen to mimic the conditions present during the evaporation process responsible for nanoplate assembly in experiments. We observed that elongated hexagons of all aspect ratios assembled exclusively into single crystals that corresponded to the parallel arrangement with few point defects and stacking faults (Fig. 3c–e, Supplementary Figs S26–S29 and Supplementary Movies S1–S3). The  $68^\circ$  opening angle of the rhombs is important for an efficient alignment. For comparison, experiments of rhomb-shaped molecular tiles with an opening angle of  $60^\circ$  on graphite surfaces showed a strong tendency to form a random hexagonal tiling<sup>29,30</sup>. Indeed, when we simulated  $60^\circ$  rhombs, only random tilings were observed. The preference of the parallel arrangement was confirmed by free-energy calculations. We obtained free-energy differences of  $F_{\text{alt}} - F_{\text{para}} = (0.047 \pm 0.005)k_B T$  for both  $B/A = 0$  and  $B/A = 1$  (Supplementary Fig. S30). The differences depend only slightly on packing fraction and are only 3% of the entropy jump  $(T\Delta S)_{\text{melt}} = (P\Delta V)_{\text{melt}} = (1.7 \pm 0.1)k_B T$  during melting for the

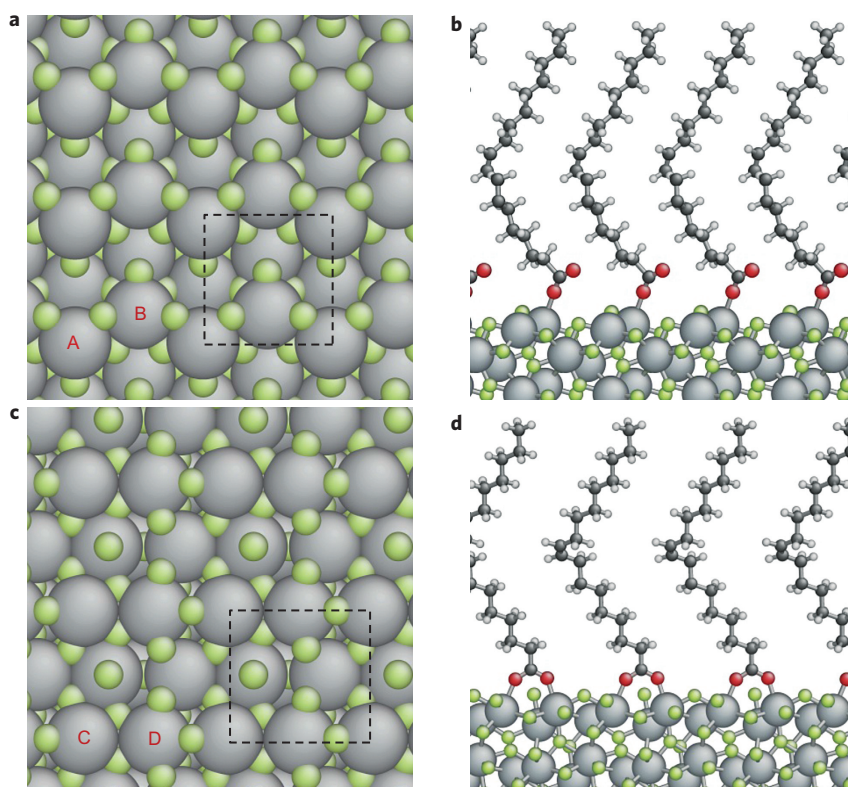


**Figure 4 | Atomic structure of  $\text{DyF}_3$  surfaces.** **a–d**, DFT calculations revealed the structure of the (001) surface (**a,b**) and the (101) surface (**c,d**). The pristine surfaces are shown in the top view (**a,c**) and surfaces with adsorbed oleic acid are viewed from the side (**b,d**). The depicted atoms are Dy (grey), F (green), C (black), O (red) and H (white). The dashed squares in **a,c** are primitive unit cells on the surfaces. Letters A, B, C and D indicate different types of surface Dy atoms that have fewer nearest-neighbour F atoms than bulk Dy atoms. For each bulk Dy atom, there are nine nearest-neighbour F atoms. On the (001) surface, this number is seven for A and eight for B, and on the (101) surface both C and D have seven nearest-neighbour F atoms.

equilateral elongated hexagon. Hence, entropy alone always favours parallel alignment and never stabilizes an alternating pattern.

**Density functional theory (DFT) calculations.** To explain the appearance of the alternating arrangement for equilateral elongated hexagons, interparticle interactions were taken into account explicitly. We performed DFT calculations to assess the relative strength of van der Waals interactions between nanoplate edges induced by a difference in the coverage density of oleic acid ligands/tethers. As shown in Supplementary Section S3, the van der Waals interaction between the nanoplate inorganic cores can be neglected in the edge-to-edge configuration. Of particular interest is the atomistic origin of possible interaction anisotropies between the crystallographically distinct nanoplate edges, which we later identify as the reason for the formation of the alternating pattern.

We obtained the most-stable atomic structures of  $\text{DyF}_3$  (001) and (101) surfaces (edges) by DFT calculations, as shown in Fig. 4a,c. We also calculated the surface dipoles of pristine edges and edges with adsorbed formate ( $\text{HCOO}$ ). In both cases the dipoles on these two edges had similar values (Supplementary Section S2). This demonstrates that dipolar interactions cannot be responsible for edge-interaction anisotropy. Furthermore, zeta-potential measurements indicated that the  $\text{LnF}_3$  nanoplates were nearly neutral, and therefore the contribution of electrostatic forces to the interparticle interactions was negligible (Supplementary Fig. S36). However, the surface atomic structures in Fig. 4a,c show that Dy atoms on the (101) edge have fewer nearest-neighbour F atoms than those on the (001) edge, which suggests that Dy atoms on the (101) edge should have a stronger adsorption ability than those on the (001) edge. Indeed, DFT calculations showed that

only one oxygen atom of each oleic acid molecule was coordinated to a Dy atom on the (001) edge, as opposed to two on the (101) edge (Fig. 4c,d and Supplementary Movies S5 and S6). As a result, the adsorption energy of oleic acid molecules on the (001) edge was 0.1 eV, compared to 0.7 eV on the (101) edge, which suggests a significant difference in the surface coverage density of oleic acid ligands between these two edges. Although DFT calculations were performed *in vacuo*, the calculated adsorption-energy difference should be robust regardless of the presence of solvents. In light of the large difference in adsorption energies, we believe that secondary solvent effects, such as an induced conformation change of alkyl chains of ligands<sup>39</sup>, will not significantly change the relative effective interaction between different types of nanoplate edges.

**Interaction asymmetry between nanoplate edges.** We introduced an empirical model for the interaction between neighbouring particles for use in Monte Carlo simulations. As the particles do not possess significant charges or dipole moments, they interact only locally with an attractive van der Waals interaction induced by their oleic acid tethers (Fig. 5a). We further assumed that the interaction energy was linearly proportional to the contact area of the tethers, which means it was proportional to the edge-to-edge contact length in the 2D model. In our interaction model (see Methods and Supplementary Fig. S31) the potential energy was minimal for a parallel arrangement with neighbour distance equal to twice the tether length. It remained to choose an attraction strength  $\xi_{A-A}$ ,  $\xi_{B-B}$  and  $\xi_{A-B}$  for each pair of edge types. For the equilateral elongated hexagon, by adding up all the neighbour contributions to the potential energy, we achieved a total energy difference  $E_{\text{alt}} - E_{\text{para}} \propto 4\xi_{A-B} - 2\xi_{A-A} - 2\xi_{B-B}$ . The alternating arrangement is preferred if the contact of unlike

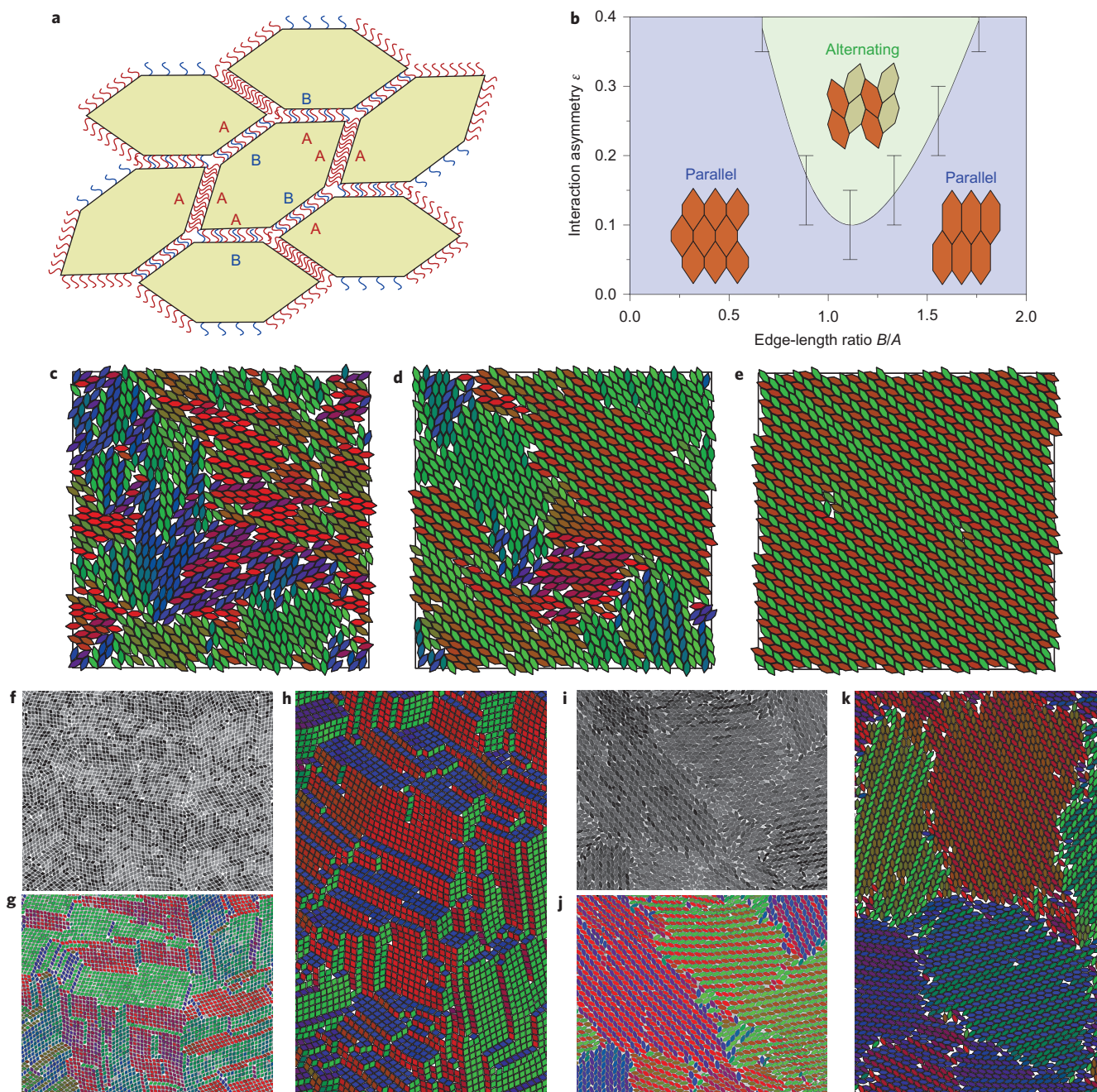


**Figure 5 | Modelling and simulation of interacting lanthanide fluoride nanoplates.** **a**, Oleic acid tethers cause an effective attraction of nanoplate edges that is asymmetric with respect to the two edge types A and B. **b**, The phase diagram as a function of edge-length ratio obtained from Monte Carlo simulations shows the stability regions of the parallel arrangement and the alternating arrangement. An interaction asymmetry greater than zero is required to stabilize the alternating arrangement. Error bars span from the lowest  $\epsilon$  that exclusively forms the alternating arrangement to the highest  $\epsilon$  that exclusively forms the parallel arrangement. **c–e**, Simulation results for the interaction asymmetry  $\epsilon = 0.2$  demonstrate the formation of the alternating arrangement (from left to right: early-, middle- and late-stage assembly). **f–k**, Electron microscopy snapshots in original contrast (**f,i**) and coloured using image processing (**g,j**) are compared to simulation results (**h,k**). A close similarity of the local order is apparent for  $B/A = 0$  (**f–h**) and  $B/A = 1$  (**i–k**).

edges is energetically advantageous, on average, compared to the contact of like edges, that is if the interaction asymmetry  $\epsilon (= 2\xi_{A-B}/(\xi_{A-A} + \xi_{B-B}) - 1) > 0$ . Indeed, this was confirmed in the simulation (Fig. 5b). A slight preference for contact of unlike edges ( $\epsilon = 0.2$ ) resulted in alternating patterns (Fig. 5c–e, Supplementary Figs S32 and S33, and Supplementary Movie S4). The introduction of interactions to the rhomb system led to a polycrystal, which closely resembles the experimental results (Supplementary Fig. S34). For  $B/A$  either sufficiently greater or smaller than one, entropy dominated and the parallel

arrangement prevailed again. Fast compression of large systems resulted in polycrystalline assemblies with excellent agreement between simulations and experimental findings (Fig. 5f–k).

In close-packed nanocrystal superlattices, the interparticle distances can be regarded as an indication of the strength of van der Waals attractions that arise from partially interdigitated ligands that connect opposing edges. In the parallel arrangement of self-assembled superlattices of irregular hexagonal nanoplates, the B–B distance was consistently larger than the A–A distance regardless of the nanoplate aspect ratio (Supplementary Fig. S37). As

configurations in which the A–A distance was larger than the B–B distance and the reverse have very similar packing densities, they are entropically degenerate. Therefore, the experimentally observed non-uniformity in interparticle distances implies an asymmetry in the attractions between A–A and B–B edges. Finally, from DFT calculations we know that the B edges were much less covered by the oleic acid tethers compared to the A edges, which suggests  $\xi_{A-A} > \xi_{B-B}$ . However, A–B and A–A distances are very similar for nanoplates in the alternating arrangement (and are also close to the A–A distance in superlattices of rhombic nanoplates), which suggests  $\xi_{A-B} \approx \xi_{A-A}$ . The result is an interaction asymmetry  $\varepsilon > 0$  (Supplementary Fig. S38).

## Conclusions

In conclusion, we report here the synthesis of a family of highly faceted planar nanotiles with rich and subtle self-assembly behaviour. The aspect ratio of the nanoplates is tunable broadly by exploiting the trend of  $\text{LnF}_3$  nanocrystal formation as a function of the type of lanthanide ions. Our results demonstrate that a combination of particle shape and directional attractions that result from the patchy coverage of ligands around the nanoplate edges is responsible for the self-assembly of nanocrystal superlattices different in structure from those that result from entropic forces alone. Controlled synthesis of shaped and faceted nanoplates not only enables the study of interplay between energy and entropy during self-assembly, but also provides further opportunity to amplify the interaction asymmetry through edge- and facet-selective chemical modification.

## Methods

**Nanocrystal synthesis.** Lanthanide fluoride nanocrystals were synthesized using thermal decomposition of  $\text{Ln}(\text{CF}_3\text{COO})_3$  in the presence of lithium salts ( $\text{Li}(\text{CF}_3\text{COO})$  or  $\text{LiF}$ ). Details are provided in Supplementary Sections S1 and S6.

**Assembly of lanthanide fluoride nanocrystals into superlattices.** A  $1.5 \times 1.5 \times 1 \text{ cm}^3$  Teflon well was half-filled with ethylene glycol. Nanocrystal solution (15  $\mu\text{l}$ ) was drop-cast onto the ethylene glycol surface and the well was then covered by a glass slide to allow slow evaporation of hexane solvent. After 30 minutes, the nanocrystal film was transferred onto a TEM grid (300 mesh) and was further dried under vacuum to remove extra ethylene glycol.

**Monte Carlo simulation.** Nanoplates were represented as perfectly hard polyhedra. Checks for overlaps were performed as in Haji-Akbari *et al.*<sup>15</sup> and Damasceno *et al.*<sup>16</sup>. A system of hard polyhedra was crystallized by slowly increasing the pressure until ordering was observed. Fast compression at the end of the simulation removed thermal disorder. Interacting nanoplates interacted via an attractive force (described below) in addition to hard-core repulsion. If interactions were present, then the pressure was kept fixed at the value at which the hard particle system crystallized and the temperature was decreased slowly until ordering occurred. We confirmed that the phase behaviour was not sensitive to the choice of pressure. System sizes ranged from 900 to 5,041 particles. Simulation times were typically several tens of millions of Monte Carlo cycles (in one cycle, each particle attempted to translate or rotate once on average). In simulation snapshots, particles were coloured according to their orientation. Free-energy calculations employed thermodynamic integration from an Einstein crystal (Frenkel–Ladd method for anisotropic hard particles).

**Interaction model.** Each pair of nanoplate edges with edge lengths  $l_1$  and  $l_2$  interacts via a pair potential chosen to mimic qualitatively the effect of oleic acid tethers. Indices were chosen such that  $l_1 \geq l_2$ . The potential energy depends on three parameters opening angle  $\theta$ , parallel shift  $d_{\parallel}$  and normal distance  $d_{\perp}$  (see Supplementary Fig. S31). In this case, the potential energy separates as  $V(\theta, d_{\parallel}, d_{\perp}) = -\xi V(\theta)V(d_{\parallel})V(d_{\perp})$  with attraction strength  $\xi > 0$  and

$$V(\theta) = 1 - \left( \frac{1 - \cos(\theta)}{1 - \cos(\theta_0)} \right)^2$$

$$V(d_{\parallel}) = \begin{cases} l_2, & \text{if } d_{\parallel} \leq (l_1 - l_2)/2 \\ (l_1 + l_2)/2 - d_{\parallel}, & \text{if } d_{\parallel} > (l_1 - l_2)/2 \end{cases}$$

$$V(d_{\perp}) = 1 - (1 - d_{\perp}/d_0)^2$$

for  $\cos(\theta) < \cos(\theta_0) = 0.95$ ,  $d_{\parallel} < (l_1 + l_2)/2$ ,  $d_{\perp} < 2d_0 = 0.4 \text{ \AA}$  and 0 otherwise.

**Image processing.** TEM images that showed nanoplatelet assembly were processed using a  $5 \times 5$  Sobel operator for edge detection. Regions of pixels with uniform contrast bounded by edges were identified as nanoplates. The particle orientation was determined from the direction of the largest eigenvalue of the inertia tensor. Particles were coloured according to a circular red–green–blue colour scheme.

**DFT calculations.** DFT calculations with spin-polarized conditions were performed using the Vienna *ab initio* simulation package (VASP) with a plane-wave basis set<sup>40</sup>. Projector augmented wave (PAW) potentials with the Perdew–Burke–Ernzerhof (PBE) exchange-correlation functionals were used. The clean  $\text{DyF}_3$  (001) and (101) surfaces were built from a fully relaxed bulk orthorhombic crystal structure with lattice constants  $a = 6.341 \text{ \AA}$ ,  $b = 6.764 \text{ \AA}$  and  $c = 4.248 \text{ \AA}$ . Detailed procedures for the calculations of optimized surface structures and the adsorptions of formate ( $\text{HCOO}$ ) and oleate ( $\text{CH}_3(\text{CH}_2)_7\text{CH} = \text{CH}(\text{CH}_2)_7\text{COO}$ ) are described in Supplementary Section S2.

Received 26 October 2012; accepted 5 April 2013;  
published online 12 May 2013

## References

1. Glotzer, S. C. & Solomon, M. J. Anisotropy of building blocks and their assembly into complex structures. *Nature Mater.* **6**, 557–562 (2007).
2. Jones, M. R. *et al.* DNA-nanoparticle superlattices formed from anisotropic building blocks. *Nature Mater.* **9**, 913–917 (2010).
3. Li, F., Josephson, D. P. & Stein, A. Colloidal assembly: the road from particles to colloidal molecules and crystals. *Angew. Chem. Int. Ed.* **50**, 360–388 (2011).
4. Ye, X. *et al.* Morphologically controlled synthesis of colloidal upconversion nanophosphors and their shape-directed self-assembly. *Proc. Natl Acad. Sci. USA* **107**, 22430–22435 (2010).
5. Langille, M. R., Zhang, J., Personick, M. L., Li, S. & Mirkin, C. A. Stepwise evolution of spherical seeds into 20-fold twinned icosahedra. *Science* **337**, 954–957 (2012).
6. Zhang, Y. W., Sun, X., Si, R., You, L. P. & Yan, C. H. Single-crystalline and monodisperse  $\text{LaF}_3$  triangular nanoplates from a single-source precursor. *J. Am. Chem. Soc.* **127**, 3260–3261 (2005).
7. Saunders, A. E., Ghezelbash, A., Smilgies, D. M., Sigman, M. B. & Korgel, B. A. Columnar self-assembly of colloidal nanodisks. *Nano Lett.* **6**, 2959–2963 (2006).
8. Shevchenko, E. V., Talapin, D. V., Kotov, N. A., O'Brien, S. & Murray, C. B. Structural diversity in binary nanoparticle superlattices. *Nature* **439**, 55–59 (2006).
9. Leunissen, M. E. *et al.* Ionic colloidal crystals of oppositely charged particles. *Nature* **437**, 235–240 (2005).
10. Yethiraj, A. & Van Blaaderen, A. A colloidal model system with an interaction tunable from hard sphere to soft and dipolar. *Nature* **421**, 513–517 (2003).
11. Chen, Q., Bae, S. C. & Granick, S. Directed self-assembly of a colloidal kagome lattice. *Nature* **469**, 381–384 (2011).
12. Macfarlane, R. J. *et al.* Nanoparticle superlattice engineering with DNA. *Science* **334**, 204–208 (2011).
13. Bishop, K. J. M., Willmer, C. E., Soh, S. & Grzybowski, B. A. Nanoscale forces and their uses in self-assembly. *Small* **5**, 1600–1630 (2009).
14. Zhao, K., Bruinsma, R. & Mason, T. G. Entropic crystal–crystal transitions of Brownian squares. *Proc. Natl Acad. Sci. USA* **108**, 2684–2687 (2011).
15. Haji-Akbari, A. *et al.* Disordered, quasicrystalline and crystalline phases of densely packed tetrahedra. *Nature* **462**, 773–777 (2009).
16. Damasceno, P. F., Engel, M. & Glotzer, S. C. Crystalline assemblies and densest packings of a family of truncated tetrahedra and the role of directional entropic forces. *ACS Nano* **6**, 609–614 (2012).
17. Agarwal, U. & Escobedo, F. A. Mesophase behaviour of polyhedral particles. *Nature Mater.* **10**, 230–235 (2011).
18. Misztal, K. *et al.* Hierarchical self-assembly of suspended branched colloidal nanocrystals into superlattice structures. *Nature Mater.* **10**, 872–876 (2011).
19. Henzie, J., Grünwald, M., Widmer-Cooper, A., Geissler, P. L. & Yang, P. Self-assembly of uniform polyhedral silver nanocrystals into densest packings and exotic superlattices. *Nature Mater.* **11**, 131–137 (2011).
20. Bodnarchuk, M. I., Kovalenko, M. V., Heiss, W. & Talapin, D. V. Energetic and entropic contributions to self-assembly of binary nanocrystal superlattices: temperature as the structure-directing factor. *J. Am. Chem. Soc.* **132**, 11967–11977 (2010).
21. Evers, W. H. *et al.* Entropy-driven formation of binary semiconductor–nanocrystal superlattices. *Nano Lett.* **10**, 4235–4241 (2010).
22. Chen, Z., Moore, J., Radtke, G., Siringhaus, H. & O'Brien, S. Binary nanoparticle superlattices in the semiconductor–semiconductor system: CdTe and CdSe. *J. Am. Chem. Soc.* **129**, 15702–15709 (2007).
23. Chen, Z. & O'Brien, S. Structure direction of II–VI semiconductor quantum dot binary nanoparticle superlattices by tuning radius ratio. *ACS Nano* **2**, 1219–1229 (2008).
24. Dong, A., Ye, X., Chen, J. & Murray, C. B. Two-dimensional binary and ternary nanocrystal superlattices: the case of monolayers and bilayers. *Nano Lett.* **11**, 1804–1809 (2011).

25. Damasceno, P. F., Engel, M. & Glotzer, S. C. Predictive self-assembly of polyhedra into complex structures. *Science* **337**, 453–457 (2012).
26. Jones, M. R., Macfarlane, R. J., Prigodich, A. E., Patel, P. C. & Mirkin, C. A. Nanoparticle shape anisotropy dictates the collective behavior of surface-bound ligands. *J. Am. Chem. Soc.* **133**, 18865–18869 (2011).
27. Glotzer, S. C. Nanotechnology: shape matters. *Nature* **481**, 450–452 (2012).
28. Bealing, C. R., Baumgardner, W. J., Choi, J. J., Hanrath, T. & Hennig, R. G. Predicting nanocrystal shape through consideration of surface–ligand interactions. *ACS Nano* **6**, 2118–2127 (2012).
29. Blunt, M. O. *et al.* Random tiling and topological defects in a two-dimensional molecular network. *Science* **322**, 1077–1081 (2008).
30. Stannard, A. *et al.* Broken symmetry and the variation of critical properties in the phase behaviour of supramolecular rhombus tilings. *Nature Chem.* **4**, 112–117 (2012).
31. Whitelam, S., Tamblyn, I., Beton, P. & Garrahan, J. Random and ordered phases of off-lattice rhombus tiles. *Phys. Rev. Lett.* **108**, 1–4 (2012).
32. Wang, F. *et al.* Simultaneous phase and size control of upconversion nanocrystals through lanthanide doping. *Nature* **463**, 1061–1065 (2010).
33. Zhao, K. & Mason, T. G. Twinning of rhombic colloidal crystals. *J. Am. Chem. Soc.* **134**, 18125–18131 (2012).
34. Zalkin, A. & Templeton, D. The crystal structures of  $\text{YF}_3$  and related compounds. *J. Am. Chem. Soc.* **75**, 2453–2458 (1953).
35. Dong, A., Chen, J., Vora, P. M., Kikkawa, J. M. & Murray, C. B. Binary nanocrystal superlattice membranes self-assembled at the liquid–air interface. *Nature* **466**, 474–477 (2010).
36. Van der Kooij F. M., Kassapidou, K. & Lekkerkerker, H. M. W. Liquid crystal phase transitions in suspensions of polydisperse plate-like particles. *Nature* **406**, 868–871 (2000).
37. Paik, T., Ko, D.-K., Gordon, T. R., Doan-Nguyen, V. & Murray, C. B. Studies of liquid crystalline self-assembly of  $\text{GdF}_3$  nanoplates by in-plane, out-of-plane SAXS. *ACS Nano* **5**, 8322–8230 (2011).
38. Stannard, A., Blunt, M. O., Beton, P. H. & Garrahan, J. P. Entropically stabilized growth of a two-dimensional random tiling. *Phys. Rev. E* **82**, 041109 (2010).
39. Roke, S., Berg, O., Buitenhuis, J., Van Blaaderen, A. & Bonn, M. Surface molecular view of colloidal gelation. *Proc. Natl Acad. Sci. USA* **103**, 13310–13314 (2006).

40. Kresse, G. & Furthmüller, J. Efficient iterative schemes for *ab initio* total-energy calculations using a plane-wave basis. *Phys. Rev. B* **54**, 11169–11186 (1996).

## Acknowledgements

X.Y. and C.B.M. acknowledge support from the Office of Naval Research Multidisciplinary University Research Initiative on Optical Metamaterials through award N00014-10-1-0942. J.C. acknowledges support from the Materials Research Science and Engineering Center program of the National Science Foundation (NSF) under award DMR-1120901. C.B.M. is also grateful to the Richard Perry University Professorship for support of his supervisor role. M.E., J.A.M. and S.C.G. acknowledge support by the Assistant Secretary of Defense for Research and Engineering, US Department of Defense (N00244-09-1-0062). Any opinions, findings, and conclusions or recommendations expressed in this publication are those of the authors and do not necessarily reflect the views of the DOD/ASD (R&E). W.L., L.Q. and J.L. acknowledge support from the NSF (DMR-1120901). G.X. and C.R.K. acknowledge support from the US Department of Energy, Office of Basic Energy Sciences, Division of Materials Sciences and Engineering (Award DE-SC0002158). Correspondence and requests for materials should be addressed to S.C.G. and C.B.M.

## Author contributions

X.Y. and J.E.C. carried out nanocrystal syntheses. X.Y. and J.C. performed nanocrystal self-assembly and structural characterization. M.E. conceived the Monte Carlo simulations. J.A.M. performed and analysed the Monte Carlo simulations. W.L. and L.Q. performed DFT calculations. G.X. conducted atomic force microscopy (AFM) characterization. S.C.G. and C.B.M. designed the study and supervised the project. All authors discussed the results and co-wrote the manuscript.

## Additional information

Supplementary information is available in the [online version](#) of the paper. Reprints and permissions information is available online at [www.nature.com/reprints](http://www.nature.com/reprints). Correspondence and requests for materials should be addressed to S.C.G. and C.B.M.

## Competing financial interests

The authors declare no competing financial interests.

## Competition of Shape and Interaction Patchiness for Self-Assembling Nanoplates

Xingchen Ye<sup>1†</sup>, Jun Chen<sup>2†</sup>, Michael Engel<sup>4†</sup>, Andres J. Millan<sup>5†</sup>, Wenbin Li<sup>6</sup>, Liang Qi<sup>7</sup>, Guozhong Xing<sup>3</sup>, Joshua E. Collins<sup>8</sup>, Cherie R. Kagan<sup>1,2,3</sup>, Ju Li<sup>6,7</sup>, Sharon C. Glotzer<sup>4,5\*</sup>, Christopher B. Murray<sup>1,2\*</sup>

<sup>1</sup>*Department of Chemistry, <sup>2</sup>Department of Materials Science and Engineering, and <sup>3</sup>Department of Electrical and Systems Engineering, University of Pennsylvania, Philadelphia, Pennsylvania 19104, USA.*

<sup>4</sup>*Department of Chemical Engineering, and <sup>5</sup>Department of Materials Science and Engineering, University of Michigan, Ann Arbor, Michigan 48109, USA.*

<sup>6</sup>*Department of Materials Science and Engineering, <sup>7</sup>Department of Nuclear Science and Engineering, Massachusetts Institute of Technology, Cambridge, MA 02139, USA.*

<sup>8</sup>*Intelligent Material Solutions, Inc., Princeton, New Jersey 08540, USA.*

<sup>†</sup>These authors contributed equally to this work

\*To whom correspondence should be addressed. E-mails: [sglotzer@umich.edu](mailto:sglotzer@umich.edu), [cbmurray@sas.upenn.edu](mailto:cbmurray@sas.upenn.edu).

## Table of Contents

1. Experimental methods .....	3
<i>Text</i>	
2. Detailed description of the methods for DFT calculations.....	3
<i>Text</i>	
3. Estimating the role of van der Waals interactions.....	5
<i>Text</i>	
4. Supplementary movies .....	7
<i>Summary of Movies S1 - S6</i>	
5. Supplementary references.....	8
<i>References 1 - 16</i>	
6. Synthesis of rare earth fluoride nanocrystals.....	9
<i>Table S1</i>	
<i>Figures S1 - S15</i>	
7. Self-assembled LnF <sub>3</sub> nanoplate superlattices.....	24
<i>Figures S16 - S25</i>	
8. Monte Carlo simulations and comparison to experiments .....	34
<i>Figures S26 - S34</i>	
9. Additional results from DFT calculations.....	43
<i>Figure S35</i>	
10. Experimental results for particle forces and interactions .....	44
<i>Figures S36 - S39</i>	

## 1. Experimental methods

All syntheses were carried out using standard Schlenk techniques. Oleic acid (OA; technical grade, 90%), 1-Octadecene (ODE; technical grade, 90%), Li(CF<sub>3</sub>COO), LiF and ethylene glycol (EG) were purchased from Sigma Aldrich. Ln(CF<sub>3</sub>COO)<sub>3</sub> were prepared according to the literature method.<sup>1</sup> A typical protocol for the synthesis of rare earth fluoride nanocrystals is described below: certain amount of lithium salts (Li(CF<sub>3</sub>COO) or LiF) and 3.264 mmol Ln(CF<sub>3</sub>COO)<sub>3</sub> (see Table S1 for details) together with 15mL of OA and 15mL of ODE were added to a three-necked flask. The mixture was then heated under vacuum at 110°C for 60 min to form a transparent, light yellow solution. The reaction flask was purged with N<sub>2</sub> for 5min and was then placed into a molten NaNO<sub>3</sub>/KNO<sub>3</sub> (1:1 mass ratio) salt bath that was stabilized at ~342°C. After a certain time of reaction at 330°C under N<sub>2</sub> flow and vigorous magnetic stirring, the solution was cooled down by adding ~15mL of ODE. The products were isolated by adding ethanol and centrifugation. No size-selective fractionation is necessary. The rare earth fluoride nanocrystals were dispersed in hexane with nanocrystal concentration of ~2.0 mg/mL further characterization and self-assembly.

**Structural characterization.** Transmission electron microscopy (TEM) images and electron diffraction patterns were taken on a JEM-1400 microscope operating at 120kV. High-resolution TEM (HRTEM) images were taken on a JEOL2010F microscope operating at 200kV. Scanning electron microscopy (SEM) was performed on a JEOL 7500F HRSEM operating at 2 kV. Power X-ray diffraction (XRD) patterns were obtained on the Rigaku Smartlab diffractometer at a scanning rate of 0.1° min<sup>-1</sup>. Samples for XRD measurements were prepared by depositing hexane solutions of nanocrystals onto a glass substrate. Atomic force microscopy (AFM) images were acquired by using a MFP-3D AFM (Asylum Research) operating in the tapping mode.

## 2. Detailed description of the methods for DFT calculations

All density functional theory (DFT) calculations were performed using the Vienna ab-initio simulation package (VASP) with a plane wave basis set<sup>2,3</sup>. Projector augmented wave (PAW) potentials<sup>4</sup> with the Perdew-Burke-Ernzerhof (PBE) exchange-correlation functional<sup>5</sup> were used under spin-polarized condition. Partial occupancies of eigenstates were determined by Gaussian smearing with sigma = 0.1 eV. The cut-off energy for the plane wave basis set was 400 eV. The clean DyF<sub>3</sub> (001) and (101) surfaces were built from fully relaxed bulk orthorhombic crystal structure with lattice constants  $a = 6.341 \text{ \AA}$ ,  $b = 6.764 \text{ \AA}$  and  $c = 4.248 \text{ \AA}$ , in close agreement with the experimental data<sup>6</sup>.

The DyF<sub>3</sub> surfaces were modeled by six-layer symmetrical slabs separated in a 1 × 1 supercell. Brillouin zone integration was performed on a grid of 5 × 5 × 1 *k* points. The total energy of the final optimized structure was calculated with more accurate tetrahedron zone summation with Blöchl correction<sup>7</sup>.

To determine the surface structure of pristine DyF<sub>3</sub> (001) and (101) surfaces, we varied the surface stoichiometry of both surfaces and calculated the corresponding total energies. Thermodynamic analysis<sup>8</sup> showed that both DyF<sub>3</sub> (001) and (101) surfaces satisfy bulk stoichiometry with Dy : F ratio of 1:3, which is understandable as DyF<sub>3</sub> is an ionic crystal. The surface energies of most stable DyF<sub>3</sub> (001) and (101) surfaces were calculated to be 0.031 eV/Å<sup>2</sup> and 0.038 eV/Å<sup>2</sup>, respectively. Both surfaces possess negative electric dipoles.

To explore the possibility of adsorption-induced dipole moment change and to study the difference in adsorption energy between DyF<sub>3</sub> (001) and (101) surfaces, we put formate (HCOO\*) onto surfaces on both sides of the slab and calculate their binding energies and dipole moments. Formate has a similar binding unit as oleic acid but fewer atoms, which allows faster calculation. Possible binding sites were identified by investigating the surface Dy atoms with less-than-bulk coordination numbers and considering their spatial arrangements. Binding sites were chosen based on: (1) Dy atoms with lowest coordinate number are preferred binding sites; (2) a preferred binding configuration coordinates both two oxygen atoms to Dy atoms. After positioning the molecules on the DyF<sub>3</sub> surfaces, the structure was allowed to fully relax except two fixed DyF<sub>3</sub> layers in the middle. The binding energies of formate on DyF<sub>3</sub> surfaces were calculated from the optimized structure. For the DyF<sub>3</sub> (001) surface, the binding energy is 0.63 eV, and for the DyF<sub>3</sub> (101) surface the binding energy is 1.10 eV. Both surfaces with adsorbed species possess a negative dipole moment, with nearly the same magnitude of -0.15 Debye/Å<sup>2</sup>.

For adsorption of oleic acid on DyF<sub>3</sub> surfaces, we adopted an unsymmetrical 1 × 1 slab model with only one oleic acid molecule adsorbed on one surface to make the calculation amenable in DFT. The slab has three layers of DyF<sub>3</sub> atoms and only the top two layers were allowed to relax. An oleic acid molecule (more accurately CH<sub>3</sub>(CH<sub>2</sub>)<sub>7</sub>CH=CH(CH<sub>2</sub>)<sub>7</sub>COO\*) was put in the vicinity of the adsorption sites, which were determined to be preferred by the calculations of formate adsorption. A vacuum layer of 15 Å separates the surfaces between the periodic images. First-principle molecular dynamics (MD) simulations were then used to relax the structure at 400 K, with a timestep of 0.5 femto-seconds. After the adsorption geometry became stable as seen in the MD run, the configuration was taken out and conjugated gradient minimization was used to optimize the structure. The total energy was then calculated

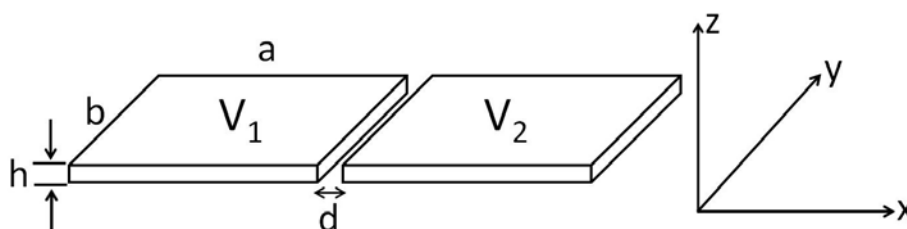
from the structure using tetrahedron zone summation, and dipole correction<sup>9</sup> was applied along the non-periodic direction. The binding energy of oleic acid was determined by comparing the energy of the adsorbed configuration with the summed energy of the pristine surface plus unadsorbed oleic acid. The binding energy of an oleic acid molecule on the DyF<sub>3</sub> (001) surface was determined to be 0.12 eV, while the binding energy on the DyF<sub>3</sub> (101) surface is 0.70 eV. This large difference in binding energy can be accounted for by the observation that both oxygen atoms are bound to Dy atoms for the (101) surface. In contrast, only one oxygen atom can bind to Dy atoms for the (001) surface, due to a higher number of nearest F atoms that weaken the adsorption ability of surface Dy atoms. We have also run first-principle MD for an extended period of time (several nanoseconds) for both DyF<sub>3</sub> surfaces and find that the two oxygen atoms of oleic acid remain bound to the DyF<sub>3</sub> (101) surface, while there is always only one oxygen bound to the (001) surface.

We want to emphasize that although the DFT calculation is performed *in vacuo*, which is standard practice in DFT calculation, the calculated adsorption energies are robust regardless of the presence of solvents because chemical bonding is a local phenomenon. Binding energies are determined by the intrinsic electronic structure of adsorbates and adsorbents, and are thus relatively insensitive to the presence of solvents. This is especially true in our case, as the solvent hexane does not contain functional groups and therefore will not adsorb onto DyF<sub>3</sub> surfaces or modify the surface electronic structure.

### 3. Estimating the role of van der Waals interactions

In this supplementary section, we demonstrate that the van der Waals (vdW) forces acting between the cores of two rare earth fluoride nanoplates is much weaker than the vdW forces acting between their oleic acid tethers. The importance of the organic tethers for the effective nanoparticle interaction has also been discussed in recent reports on nanoparticle superlattices and superlattice membranes<sup>10–12</sup>.

We estimate the vdW forces between nanoplatelet cores in the following configuration:



Following a calculation by Rocco and Hoover<sup>13</sup> we estimate the interaction of two thin platelets. We simplified the problem by approximating the rhombohedral particle by a thin rectangular shape. The interaction strength and its decay as a function of separation are captured well by the rectangular shape. The result for the strength of the interaction is

$$\Phi = -\rho^2 \lambda \int_{V_1} dV_1 \int_{V_2} dV_2 \frac{1}{r^6} = -\frac{A}{\pi^2} h^2 K_6 \approx -\frac{A}{\pi^2} h^2 \left( \frac{\pi b}{32d^3} \right) = -\frac{Abh^2}{32\pi d^3},$$

where  $A = \pi^2 \rho^2 \lambda$  is the Hamaker constant. Since the Hamaker constants for  $\text{EuF}_3$ ,  $\text{TbT}_3$  or  $\text{DyF}_3$  are not found in the literature, we use the Hamaker constant of another common fluoride compound,  $\text{CaF}_2$ , measured in an aqueous medium<sup>14</sup>,  $6 \times 10^{-21} \text{J} \approx 37.5 \text{meV}$ . Thus, the vdW attraction between two nanoplates (with  $d = 2.3 \text{nm}$ ,  $h = 5 \text{nm}$ , and  $b = 30 \text{nm}$ ) can be estimated as:

$$\Phi = \frac{(37.5 \text{ meV}) \cdot 30 \cdot 5^2}{32\pi \cdot (2.3)^3} \approx 23 \text{ meV} \approx 0.9 k_B T \text{ (at } 25^\circ \text{C)}$$

Experimental values for the contact edge length  $b$  range from 13nm to 33nm, depending on the exact shape and the packing configuration (parallel vs. alternating, see Fig. S39). The value  $b = 30 \text{nm}$  is a good estimate. It is important to point out that:

- 1) Since Hamaker constants in a hydrocarbon medium are generally lower than Hamaker constants in water<sup>15</sup>, our calculated vdW attraction (23meV) represents an upper bound.
- 2) The vdW attraction of 23 meV between our inorganic nanoplates is close to values obtained for sub-10nm spherical semiconductor nanoparticles<sup>11</sup>. The smaller size of the nanospheres is compensated by the reduced height of the nanoplates.

The vdW attraction between the cores is comparable to the thermal energy at room temperature and therefore small. Furthermore, the strength of the vdW attraction is identical in the parallel and the alternating configuration and therefore cannot distinguish between the two.

On the other hand, the vdW attraction between neighboring alkyl chains of oleic acid ligands is of great importance and dominates over the vdW attractions between platelet cores. Since the length of an oleic acid molecule in its extended configuration is about 2nm and the nearest interparticle separation in the superlattices is about 2.2nm (much smaller than twice the length of an oleic acid molecule), it is reasonable to conclude that the alkyl chains interpenetrate or become interdigitated. Besides, ligand-ligand

interactions are more effective if the particle surfaces are flat (e.g. nanoplates) rather than curved (e.g. spherical nanoparticles)<sup>16</sup>.

The vdW attraction between two nearest parallel hydrocarbon tails of stearic acid molecule in a close-packed configuration has been estimated to be 364 meV/molecule<sup>11</sup>. Given the structural similarity between oleic acid and stearic acid molecules, this value suggests that the ligand-ligand VdW attraction could be an order of magnitude larger than the VdW attraction between the nanoplate themselves when the ligand chains are forced to pack and completely interdigitate between nearest nanoplates. Such a complete interdigitation might be achieved after a complete evaporation of the solvent.

We note that the calculation of the total vdW interaction energy arising from the ligands requires determining the spatial distribution and molecular conformation of the oleic acid on each of the nanoplate side facets, which is not possible at the moment.

#### 4. Supplementary movies

Movie S1: Hard rhombs ( $N = 900$ ) with opening angle  $68^\circ$  and edge length ratio  $B/A = 0$  self-assemble over 40 million sweeps. The volume of the box is slowly increased until crystallization sets in. Snapshots of the simulation are shown in Fig. S26.

Movie S2: Hard equilateral elongated hexagons ( $N = 1024$ ) with edge length ratio  $B/A = 1$  self-assemble over 7 million sweeps. The system is run a constant pressure. Snapshots of the simulation are shown in Fig. S28.

Movie S3: Hard, strongly elongated hexagons ( $N = 900$ ) with edge length ratio  $B/A = 2$  self-assemble over 8 million sweeps. Snapshots of the simulation are shown in Fig. S29.

Movie S4: Interacting equilateral elongates hexagons ( $N = 1024$ ) with edge length ratio  $B/A = 1$  and interaction asymmetry  $\varepsilon = 0.2$  self-assemble relatively fast over 3.5 million sweeps. Snapshots of the simulation are shown in Fig. S32.

Movie S5: Oleic acid tethers are only weakly bound to the  $\text{DyF}_3$  (001) surface. Each molecule is typically bound at only one site to the nanoplatelet and can fluctuate by thermal motion. Periodic boundary conditions are employed.

Movie S6: In contrast, oleic acid tethers can bind much stronger to the  $\text{DyF}_3$  (101) surface. Each molecule is now typically bound at two sites to the nanoplatelet. Periodic boundary conditions are employed.

## 5. Supplementary references

1. Roberts, J. E. Lanthanum and neodymium salts of trifluoroacetic acid. *J. Am. Chem. Soc.* **83**, 1087–1088 (1961).
2. Kresse, G. & Furthmüller, J. Efficient iterative schemes for ab initio total-energy calculations using a plane-wave basis. *Phys. Rev. B* **54**, 11169–11186 (1996).
3. Kresse, G. & Furthmüller, J. Efficiency of ab-initio total energy calculations for metals and semiconductors using a plane-wave basis set. *Comput. Mater. Sci.* **6**, 15–50 (1996).
4. Blöchl, P. E. Projector augmented-wave method. *Phys. Rev. B* **50**, 17953–17979 (1994).
5. Perdew, J. P., Burke, K. & Ernzerhof, M. Generalized gradient approximation made simple. *Phys. Rev. Lett.* **77**, 3865–3868 (1996).
6. Zalkin, A. & Templeton, D. H. The crystal structures of YF<sub>3</sub> and related compounds. *J. Am. Chem. Soc.* **75**, 2453–2458 (1953).
7. Blöchl, P. E., Jepsen, O. & Andersen, O. K. Improved tetrahedron method for Brillouin-zone integrations. *Phys. Rev. B* **49**, 16223–16233 (1994).
8. Moll, N., Kley, A., Pehlke, E. & Scheffler, M. GaAs equilibrium crystal shape from first principles. *Phys. Rev. B* **54**, 8844–8855 (1996).
9. Makov, G. & Payne, M. C. Periodic boundary conditions in ab initio calculations. *Phys. Rev. B* **51**, 4014–4022 (1995).
10. Mueggenburg, K. E., Lin, X.-M., Goldsmith, R. H. & Jaeger, H. M. Elastic membranes of close-packed nanoparticle arrays. *Nature Mater.* **6**, 656–660 (2007).
11. Chen, Z., Moore, J., Radtke, G., Siringhaus, H. & O'Brien, S. Binary nanoparticle superlattices in the semiconductor-semiconductor system: CdTe and CdSe. *J. Am. Chem. Soc.* **129**, 15702–15709 (2007).
12. Landman, U. & Luedtke, W. D. Small is different: energetic, structural, thermal, and mechanical properties of passivated nanocluster assemblies. *Faraday Discuss.* **125**, 1–22 (2004).
13. De Rocco, A. G. & Hoover, W. G. On the interaction of colloidal particles. *Proc. Natl. Acad. Sci. U. S. A.* **46**, 1057–1065 (1960).
14. Perez, L. A. & Nancollas, G. H. Kinetics of crystallization and flocculation of calcium fluoride. *Colloids Surf.* **52**, 231–240 (1991).
15. Shevchenko, E. V, Talapin, D. V, Murray, C. B. & O'Brien, S. Structural characterization of self-assembled multifunctional binary nanoparticle superlattices. *J. Am. Chem. Soc.* **128**, 3620–3637 (2006).
16. Glotzer, S. C. Nanotechnology: Shape matters. *Nature* **481**, 450–452 (2012).

## 6. Synthesis of rare earth fluoride nanocrystals

**Table S1.** Synthetic conditions of  $\text{LnF}_3$  ( $\text{Ln} = \text{La} - \text{Ho}$ ) and  $\text{LiLnF}_4$  ( $\text{Ln} = \text{Ho}, \text{Er}$ ) nanocrystals. Unless otherwise specified, OA/ODE = 15 mL/15 mL and a reaction temperature of 330°C are used for all syntheses.

Reactants		Reaction Time	Nanocrystal composition	Nanocrystal Morphology	Relevant Figures
Lithium salt	$\text{Ln}(\text{CF}_3\text{CO}_2)_3$				
LiF or $\text{Li}(\text{CF}_3\text{CO}_2)_3$	$\text{Ln}(\text{CF}_3\text{CO}_2)_3$ ( $\text{Ln} = \text{La}, \text{Pr}, \text{Nd}, \text{Sm}$ ) 3.264 mmol	30-60 min	$\text{LaF}_3, \text{PrF}_3, \text{NdF}_3,$ or $\text{SmF}_3$	circular plate	S1, S2
$\text{Li}(\text{CF}_3\text{CO}_2)_3$ 3.372 mmol	$\text{Ho}(\text{CF}_3\text{CO}_2)_3$ 3.264 mmol	30 min	$\text{HoF}_3$ and $\text{LiHoF}_4$	rhombohedral and tetragonal bipyramid plate	S3a-f
$\text{Li}(\text{CF}_3\text{CO}_2)_3$ 3.372 mmol	$\text{Er}(\text{CF}_3\text{CO}_2)_3$ 3.264 mmol	22 min	$\text{LiErF}_4$	tetragonal bipyramid plate	S3g, S3h
$\text{Li}(\text{CF}_3\text{CO}_2)_3$ 3.372 mmol	$\text{Eu}(\text{CF}_3\text{CO}_2)_3$ 3.264 mmol	45 min	orthorhombic $\text{EuF}_3$	irregular hexagonal plate	S5a, S5b
$\text{Li}(\text{CF}_3\text{CO}_2)_3$ 5.058 mmol	$\text{Eu}(\text{CF}_3\text{CO}_2)_3$ 3.264 mmol	45 min	orthorhombic $\text{EuF}_3$	irregular hexagonal plate	1i, S5c-f
LiF 3.372 mmol	$\text{Eu}(\text{CF}_3\text{CO}_2)_3$ 3.264 mmol	45 min	orthorhombic and hexagonal $\text{EuF}_3$	circular and irregular hexagonal plate	S6a, S6b
LiF 6.744 mmol	$\text{Eu}(\text{CF}_3\text{CO}_2)_3$ 3.264 mmol	45 min	orthorhombic and hexagonal $\text{EuF}_3$	circular and irregular hexagonal plate	S6c, S6d
LiF 10.116 mmol	$\text{Eu}(\text{CF}_3\text{CO}_2)_3$ 3.264 mmol	45 min	orthorhombic and hexagonal $\text{EuF}_3$	circular and irregular hexagonal plate	S6e, S6f
None	$\text{Eu}(\text{CF}_3\text{CO}_2)_3$ 3.264 mmol	45 min	hexagonal $\text{EuF}_3$	triangular and hexagonal plate	S8
$\text{Li}(\text{CF}_3\text{CO}_2)_3$ 3.372 mmol	$\text{Tb}(\text{CF}_3\text{CO}_2)_3$ 3.264 mmol	22 min	orthorhombic $\text{TbF}_3$	irregular hexagonal plate	1g, S9a- S9c
$\text{Li}(\text{CF}_3\text{CO}_2)_3$ 4.215 mmol	$\text{Tb}(\text{CF}_3\text{CO}_2)_3$ 3.264 mmol	25 min	orthorhombic $\text{TbF}_3$	irregular hexagonal plate	1f, S9d- S9f
LiF 3.372 mmol	$\text{Tb}(\text{CF}_3\text{CO}_2)_3$ 3.264 mmol	45 min	orthorhombic $\text{TbF}_3$	rhombohedral plate	S10
LiF 3.372 mmol	$\text{Dy}(\text{CF}_3\text{CO}_2)_3$ 3.264 mmol	20 min	orthorhombic $\text{DyF}_3$	irregular hexagonal plate	1h, S12b, S13d-f
LiF 3.372 mmol	$\text{Dy}(\text{CF}_3\text{CO}_2)_3$ 3.264 mmol	30 min	orthorhombic $\text{DyF}_3$	rhombohedral plate	1e, S12d, S13a-c
LiF 5.058 mmol	$\text{Dy}(\text{CF}_3\text{CO}_2)_3$ 3.264 mmol	22 min	orthorhombic $\text{DyF}_3$	rhombohedral plate	S14a

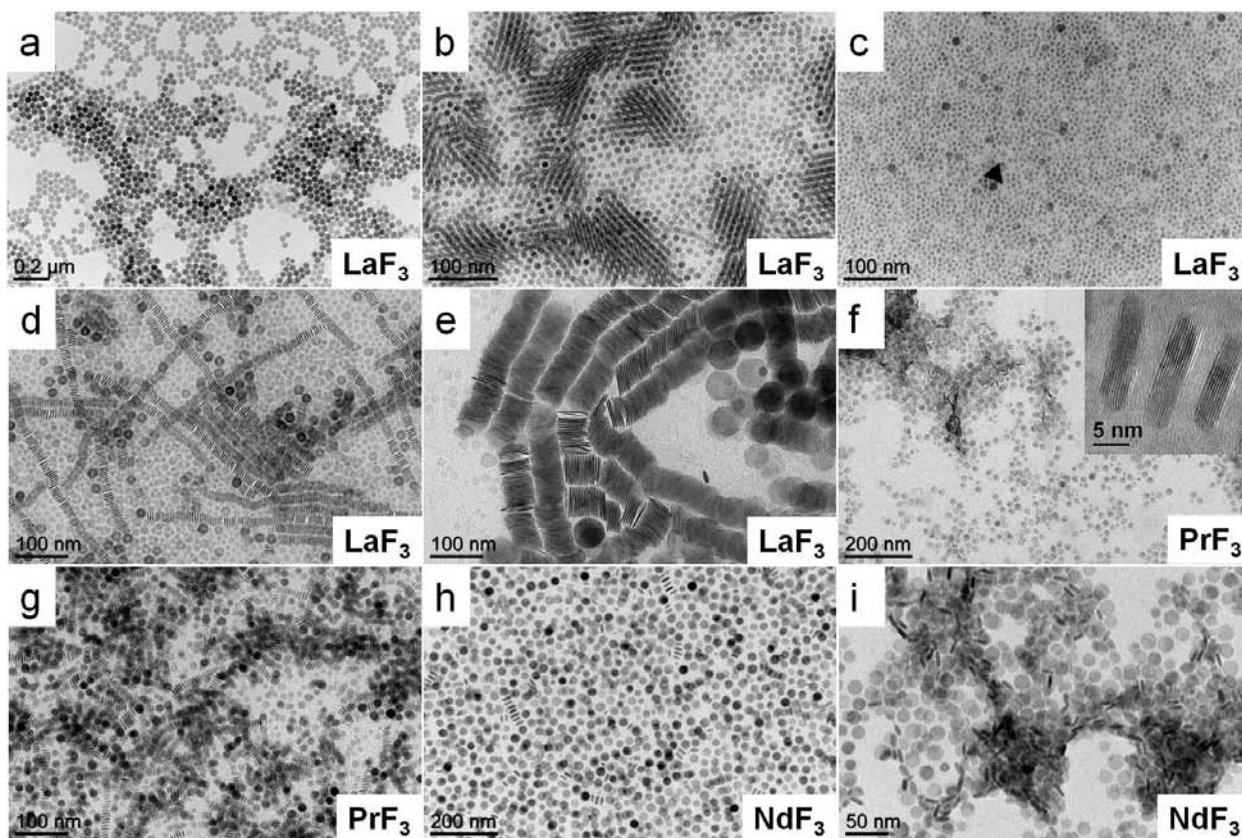


**Figure S1.** (a) TEM image of LaF<sub>3</sub> nanoplates synthesized using 6.744 mmol LiF with a reaction time of 45 min. (b) TEM image of LaF<sub>3</sub> nanoplates synthesized using 3.372 mmol LiF with a reaction time of 30 min. (c) TEM image of LaF<sub>3</sub> nanocrystals synthesized without any lithium salts with a reaction time of 45 min. (d) TEM image of LaF<sub>3</sub> nanoplates synthesized using 3.372 mmol Li(CF<sub>3</sub>CO<sub>2</sub>)<sub>3</sub> with a reaction time of 30 min. (e) TEM image of LaF<sub>3</sub> nanoplates synthesized using 5.058 mmol Li(CF<sub>3</sub>CO<sub>2</sub>)<sub>3</sub> with a reaction time of 45 min. (f) TEM image of PrF<sub>3</sub> nanoplates synthesized using 3.372 mmol Li(CF<sub>3</sub>CO<sub>2</sub>)<sub>3</sub> with a reaction time of 45 min. Inset is the HRTEM image of PrF<sub>3</sub> nanoplates standing on the edge. (g) TEM images of PrF<sub>3</sub> nanoplates synthesized using 5.058 mmol Li(CF<sub>3</sub>CO<sub>2</sub>)<sub>3</sub> with a reaction time of 45 min. (h) TEM image of NdF<sub>3</sub> nanoplates synthesized using 3.372 mmol Li(CF<sub>3</sub>CO<sub>2</sub>)<sub>3</sub> with a reaction time of 45 min. (i) TEM image of NdF<sub>3</sub> nanoplates synthesized using 5.058 mmol Li(CF<sub>3</sub>CO<sub>2</sub>)<sub>3</sub> with a reaction time of 60 min.

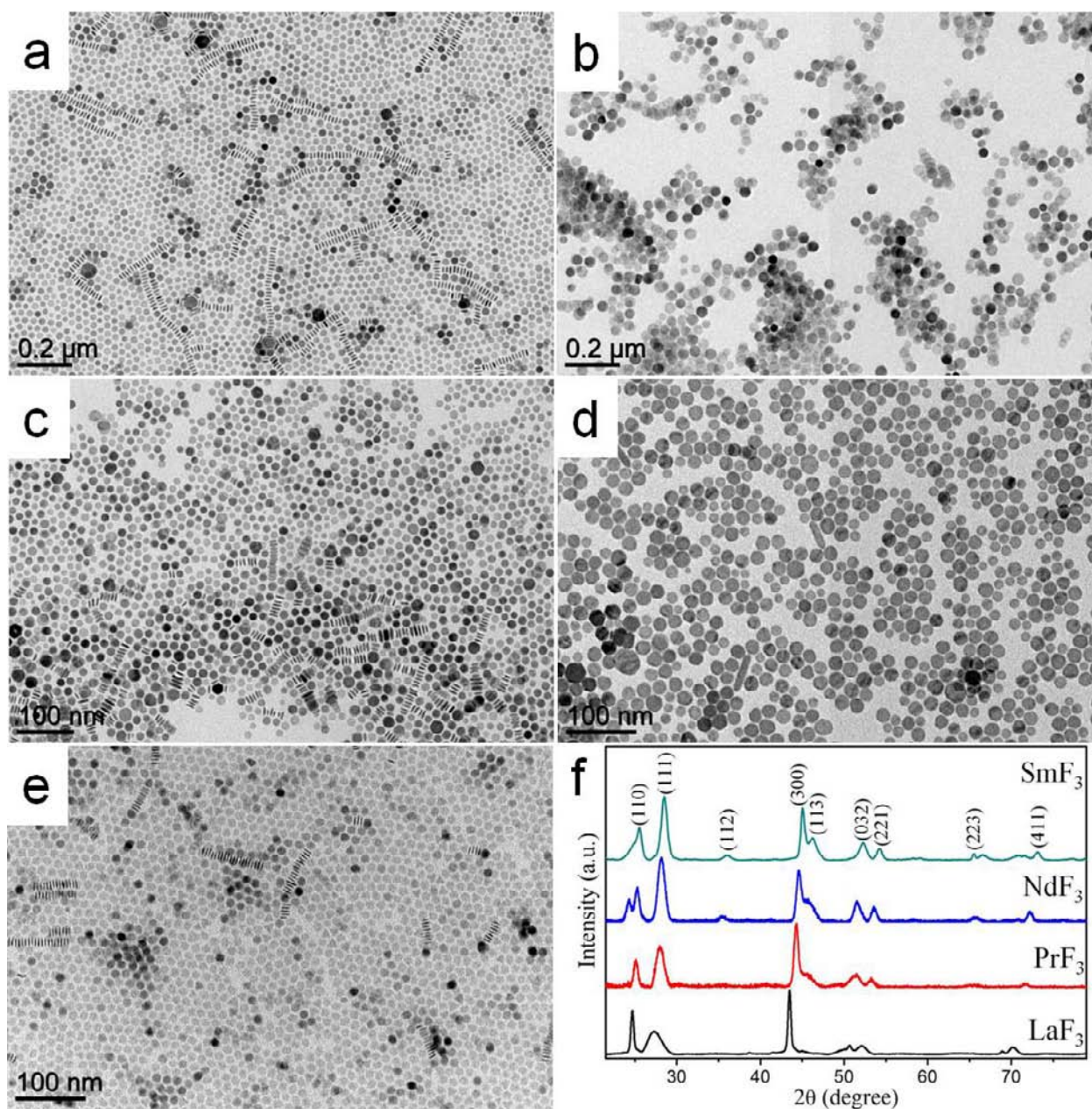


**Figure S2.** (a) TEM image of SmF<sub>3</sub> nanoplates synthesized using 3.372 mmol Li(CF<sub>3</sub>CO<sub>2</sub>)<sub>3</sub> with a reaction times of 40 min. (b) TEM image of SmF<sub>3</sub> nanoplates synthesized using 5.058 mmol Li(CF<sub>3</sub>CO<sub>2</sub>)<sub>3</sub> with a reaction time of 40 min. (c) TEM image of SmF<sub>3</sub> nanoplates synthesized using 3.372 mmol LiF with a reaction time of 40 min. (d) TEM image of SmF<sub>3</sub> nanoplates synthesized using 6.744 mmol LiF with a reaction time of 40 min. (e) TEM image of SmF<sub>3</sub> nanoplates synthesized without any lithium salts with a reaction time of 45 min. (f) Powder XRD patterns of hexagonal phase LaF<sub>3</sub>, PrF<sub>3</sub>, NdF<sub>3</sub> and SmF<sub>3</sub> nanoplates.

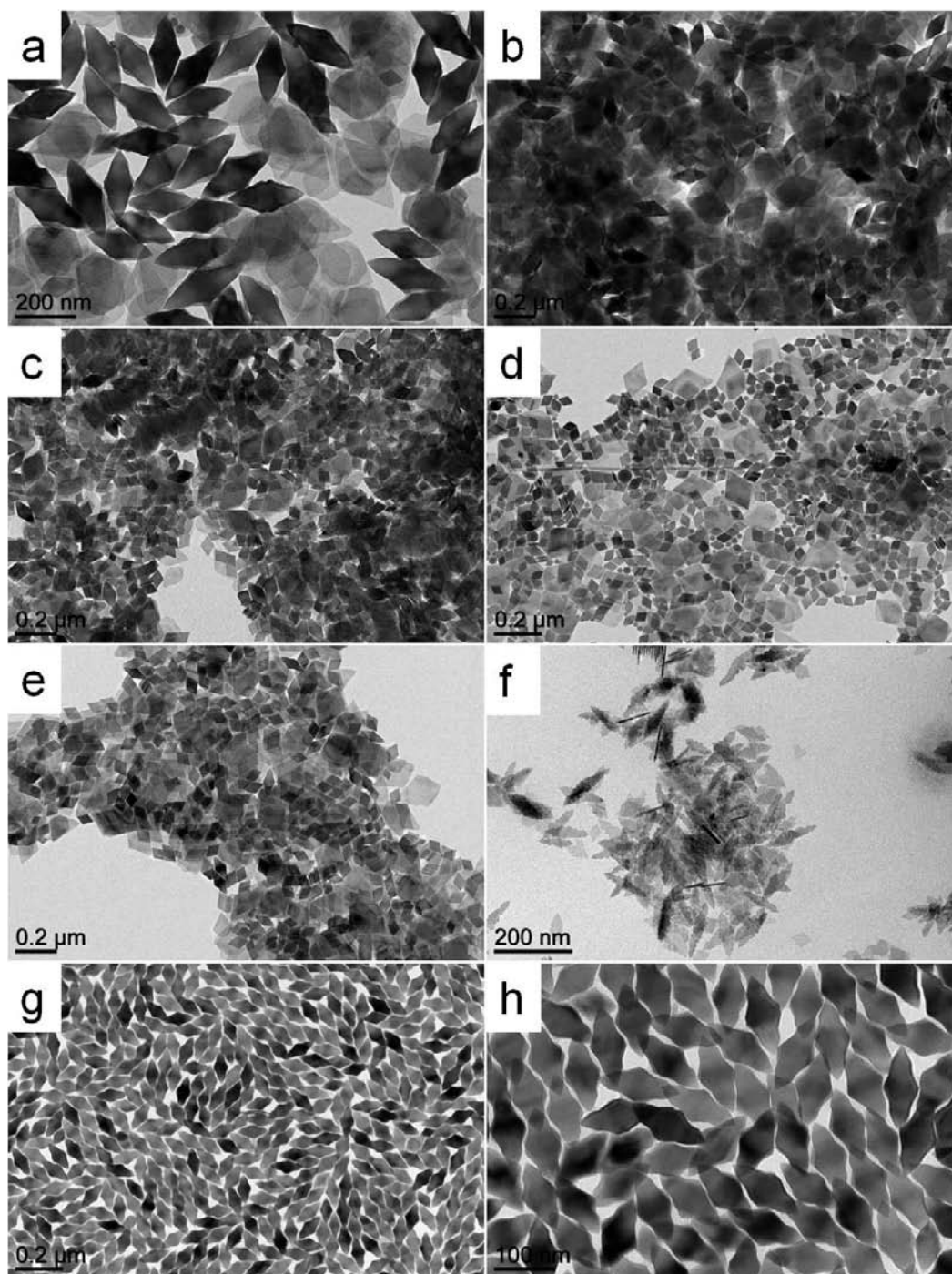


**Figure S3.** TEM images of LiHoF<sub>4</sub> and HoF<sub>3</sub> nanoplates synthesized using (a) 3.372 mmol Li(CF<sub>3</sub>CO<sub>2</sub>)<sub>3</sub>, (b) 5.058 mmol Li(CF<sub>3</sub>CO<sub>2</sub>)<sub>3</sub>, (c) 3.372 mmol LiF, (d) 6.774 mmol LiF and (e) 10.116 mmol LiF with a reaction time of 30 min. (f) TEM image of HoF<sub>3</sub> nanoplates synthesized without any lithium salts with a reaction time of 60 min. (g-h) TEM images of LiErF<sub>4</sub> tetragonal bipyramids synthesized using 3.372 mmol Li(CF<sub>3</sub>CO<sub>2</sub>)<sub>3</sub> with a reaction time of 23 min.

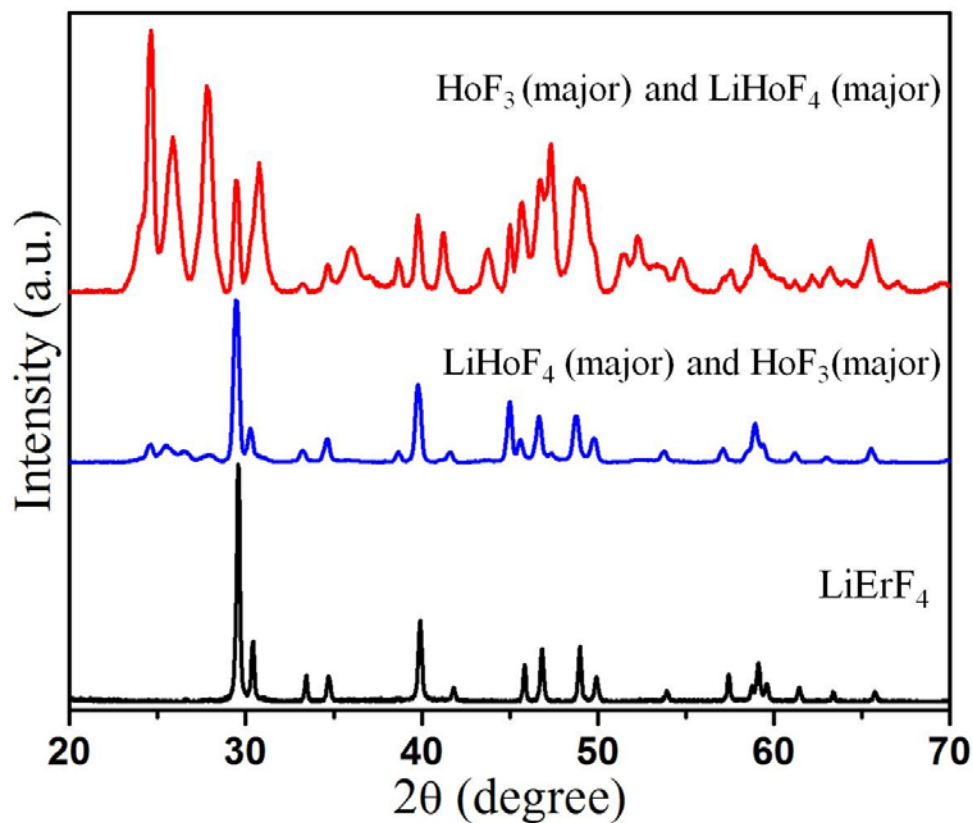


**Figure S4.** Powder XRD patterns of LiHoF<sub>4</sub> and HoF<sub>3</sub> nanoplates synthesized using 3.372 mmol LiF (red curve) and 3.372 mmol Li(CF<sub>3</sub>CO<sub>2</sub>)<sub>3</sub> (blue curve) with a reaction time of 30 min. Powder XRD pattern of LiErF<sub>4</sub> tetragonal bipyramids synthesized using 3.372 mmol Li(CF<sub>3</sub>CO<sub>2</sub>)<sub>3</sub> with a reaction time of 23 min (black curve).

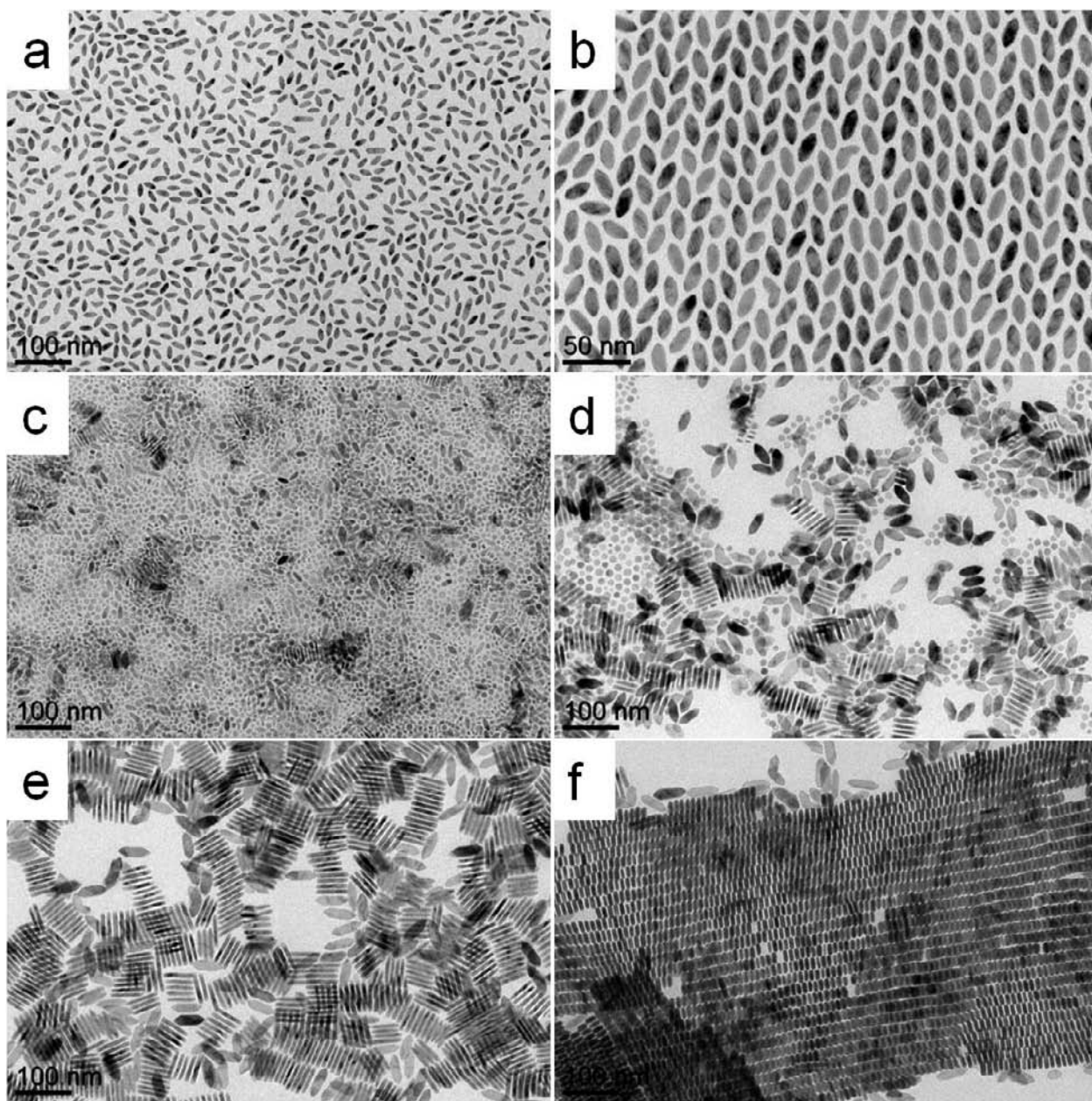


**Figure S5.** (a-b) TEM images of  $\text{EuF}_3$  nanoplates synthesized using 3.372 mmol  $\text{Li}(\text{CF}_3\text{CO}_2)_3$ . The  $\text{EuF}_3$  nanoplates have dimensions similar to the  $\text{DyF}_3$  nanoplates shown in Figure 1h and also exhibit alternating packing motif in self-assembled superlattices. (c-f) TEM images of  $\text{EuF}_3$  nanoplates synthesized using 5.058 mmol  $\text{Li}(\text{CF}_3\text{CO}_2)_3$  with reaction times of 15 min (c), 30 min (d), 45 min (e) and 60 min (f).

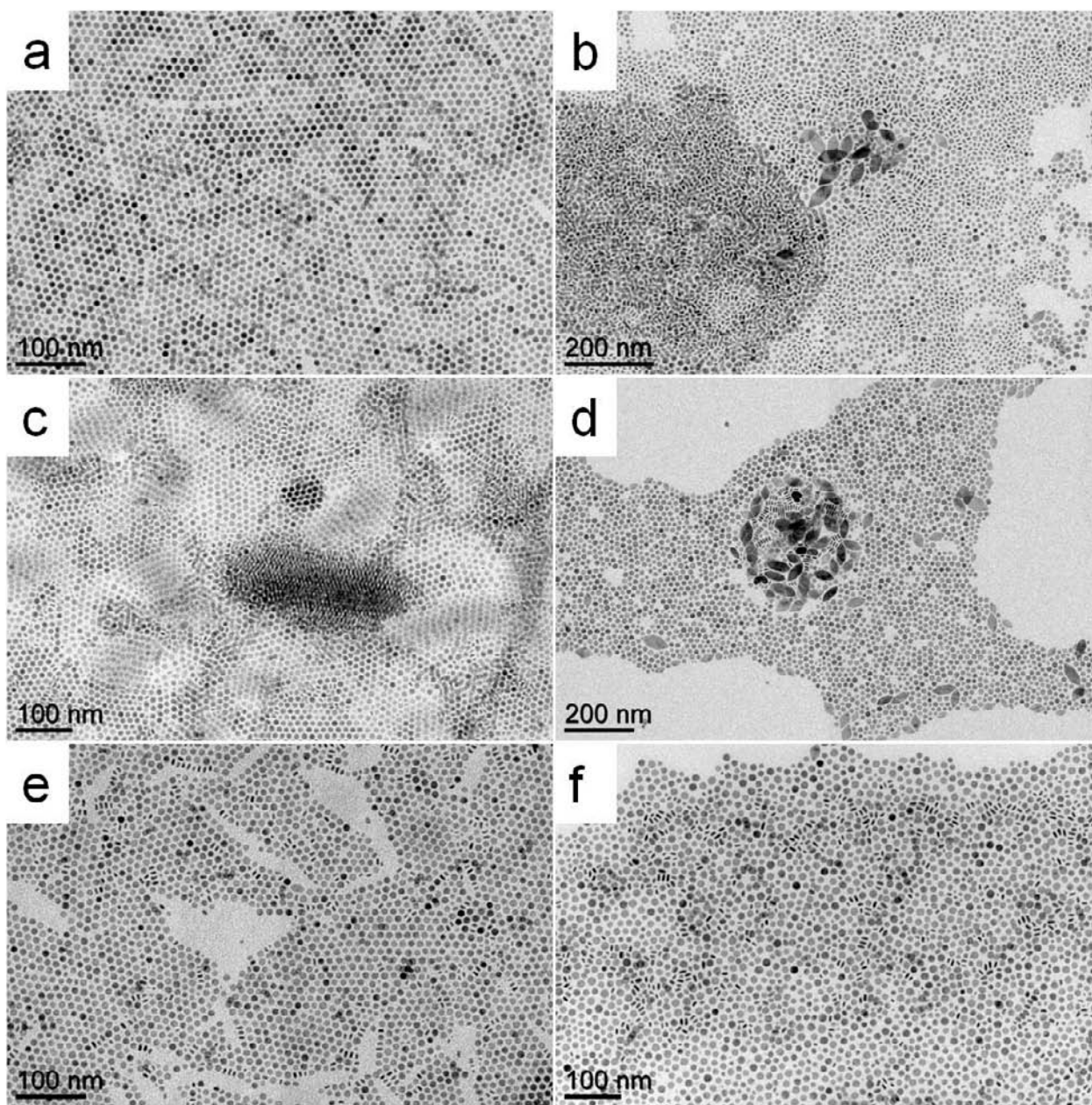


**Figure S6.** TEM images of  $\text{EuF}_3$  nanoplates synthesized using 3.372 mmol LiF with reaction times of (a) 30 min and (b) 45 min. TEM images of  $\text{EuF}_3$  nanoplates synthesized using 6.744 mmol LiF with reaction times of (c) 30 min and (d) 45 min. TEM images of  $\text{EuF}_3$  nanoplates synthesized using 10.116 mmol LiF with reaction times of (e) 30 min and (f) 45 min.

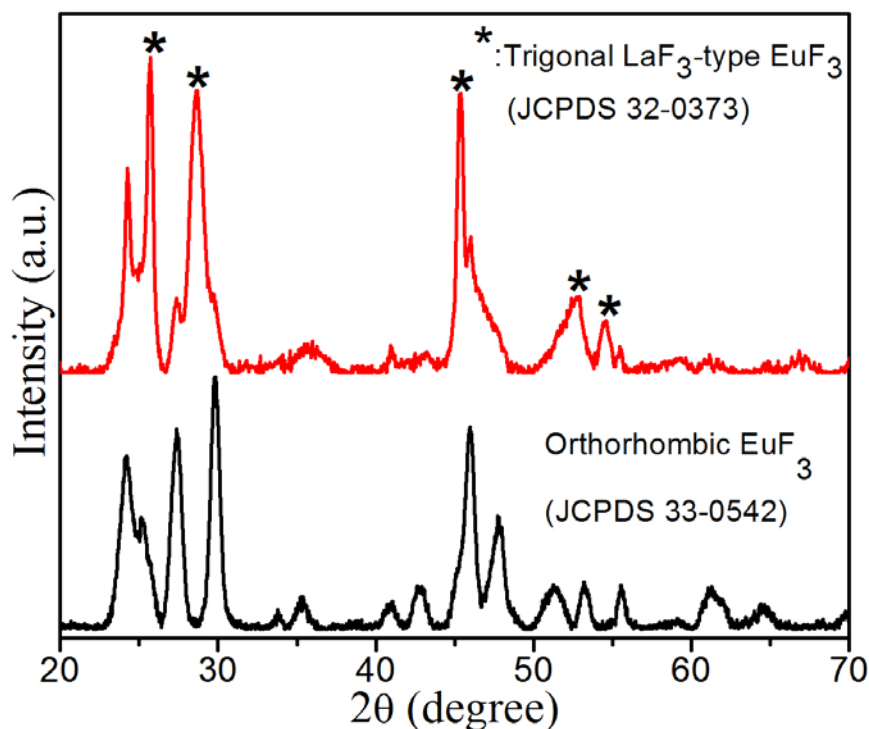


**Figure S7.** Powder XRD patterns of orthorhombic phase  $\text{EuF}_3$  nanoplates synthesized using 5.058 mmol  $\text{Li}(\text{CF}_3\text{CO}_2)_3$  with a reaction time of 45 min (black curve) and  $\text{EuF}_3$  nanoplates (both orthorhombic and hexagonal phase are present) synthesized using 6.744 mmol  $\text{LiF}$  with a reaction time of 45 min (red curve).

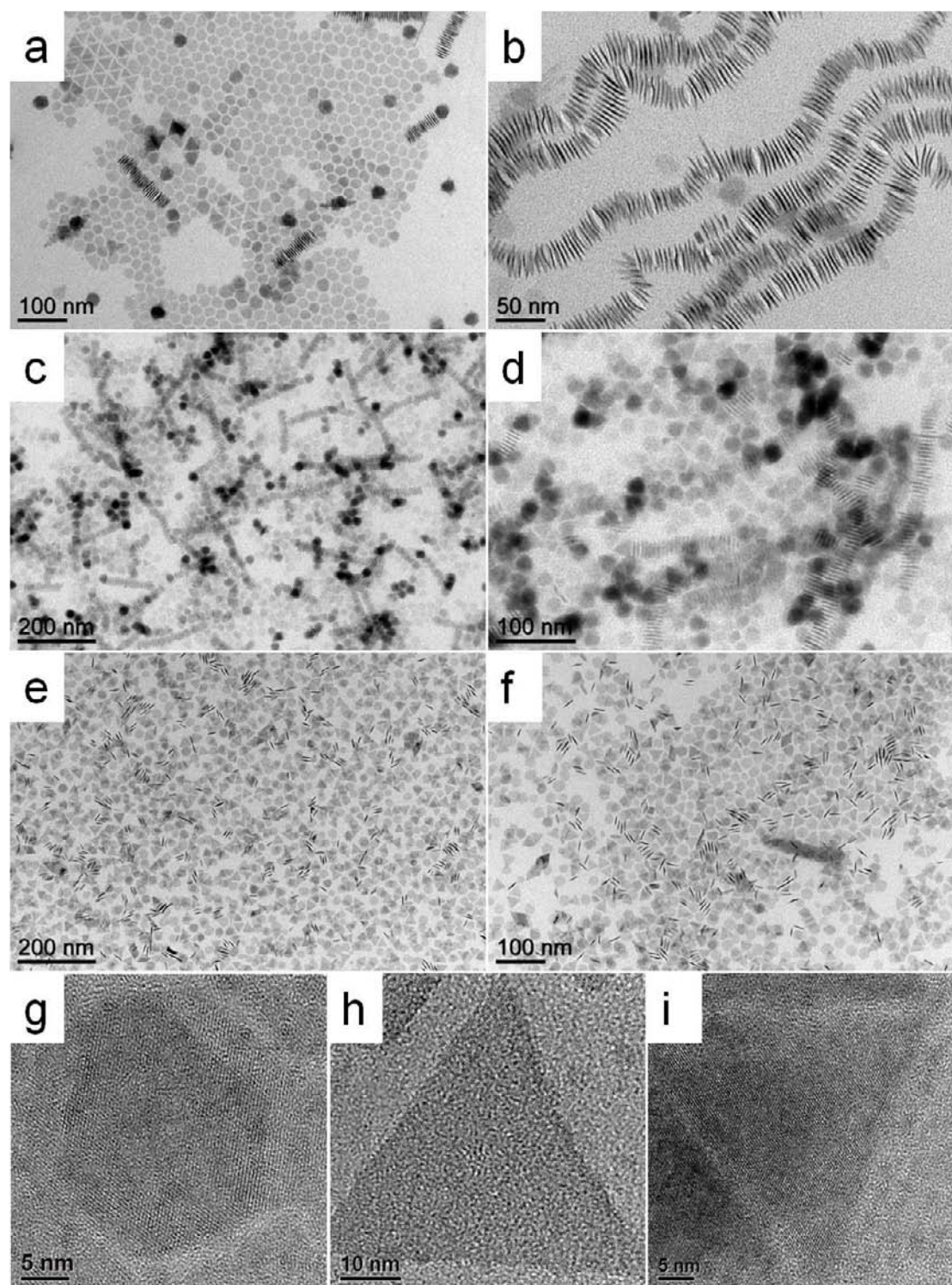


**Figure S8.** TEM images of EuF<sub>3</sub> nanoplates synthesized without any lithium salts with reaction times of (a, b) 25 min, (c, d) 45 min and (e, f) 60 min. (g-i) HRTEM images of EuF<sub>3</sub> nanoplates shown in (e) and (f).

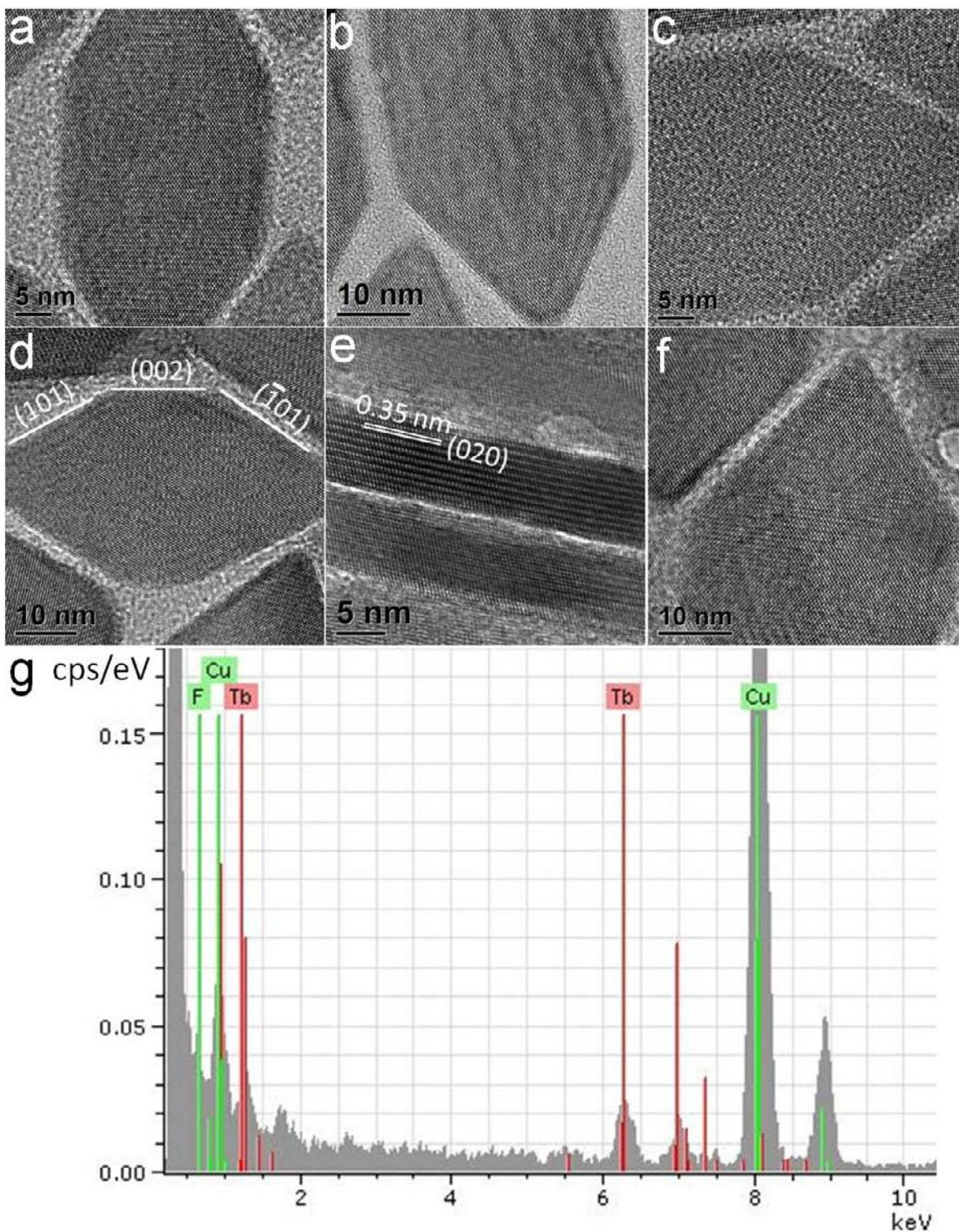


**Figure S9.** (a-c) Additional HRTEM images of TbF<sub>3</sub> nanoplates synthesized using 3.372 mmol Li(CF<sub>3</sub>CO<sub>2</sub>)<sub>3</sub> with a reaction time of 22 min. (d-f) Additional HRTEM images and (g) EDX spectrum of TbF<sub>3</sub> nanoplates synthesized using 4.215 mmol Li(CF<sub>3</sub>CO<sub>2</sub>)<sub>3</sub> with a reaction time of 25 min. Image (e) shows TbF<sub>3</sub> nanoplates standing on the edge.

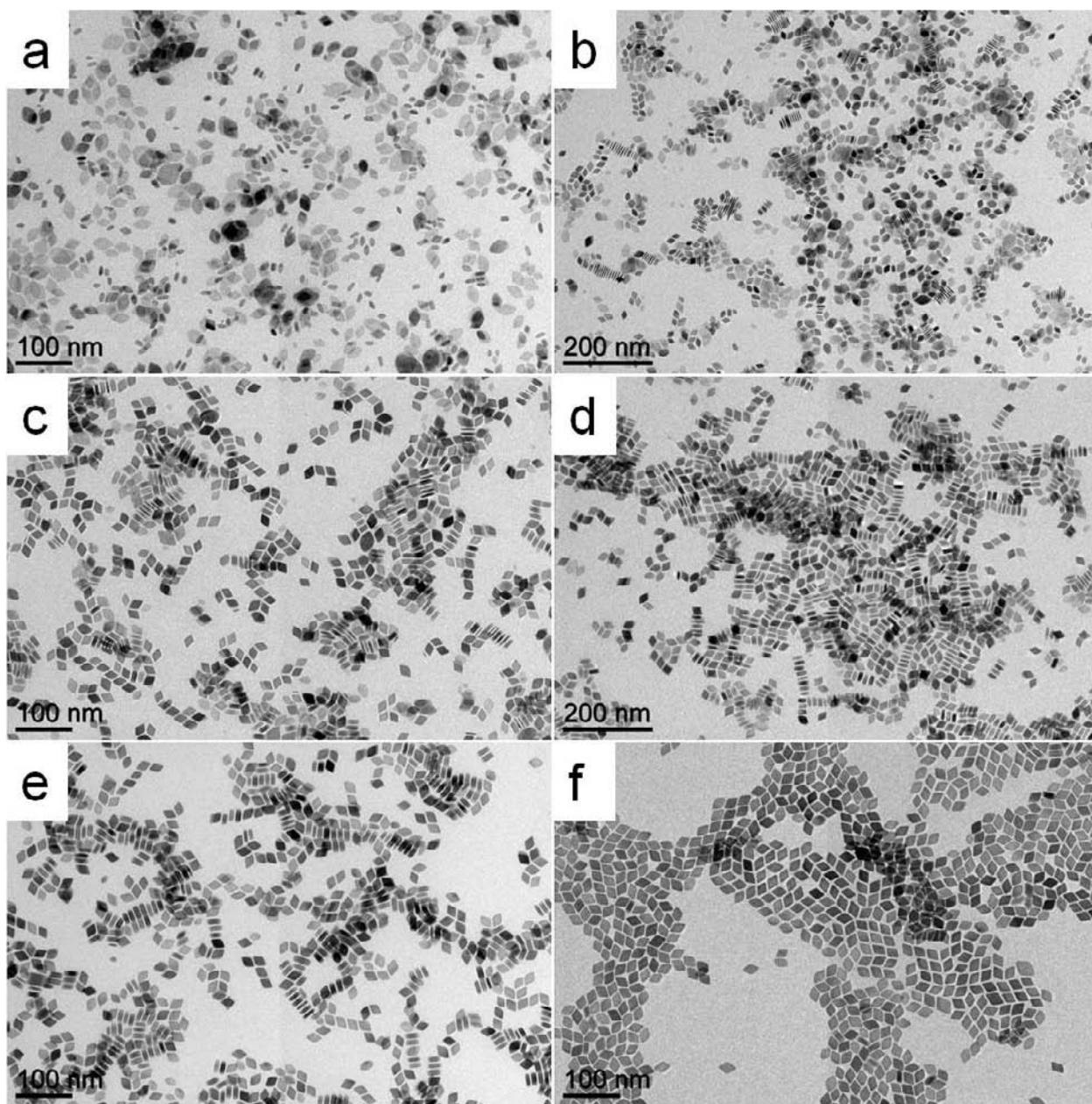


**Figure S10.** TEM images of TbF<sub>3</sub> nanoplates synthesized using 3.372 mmol LiF with reaction times of (a) 10 min, (b) 15 min, (c) 22 min, (d) 30 min, (e) 37 min and (f) 45 min.

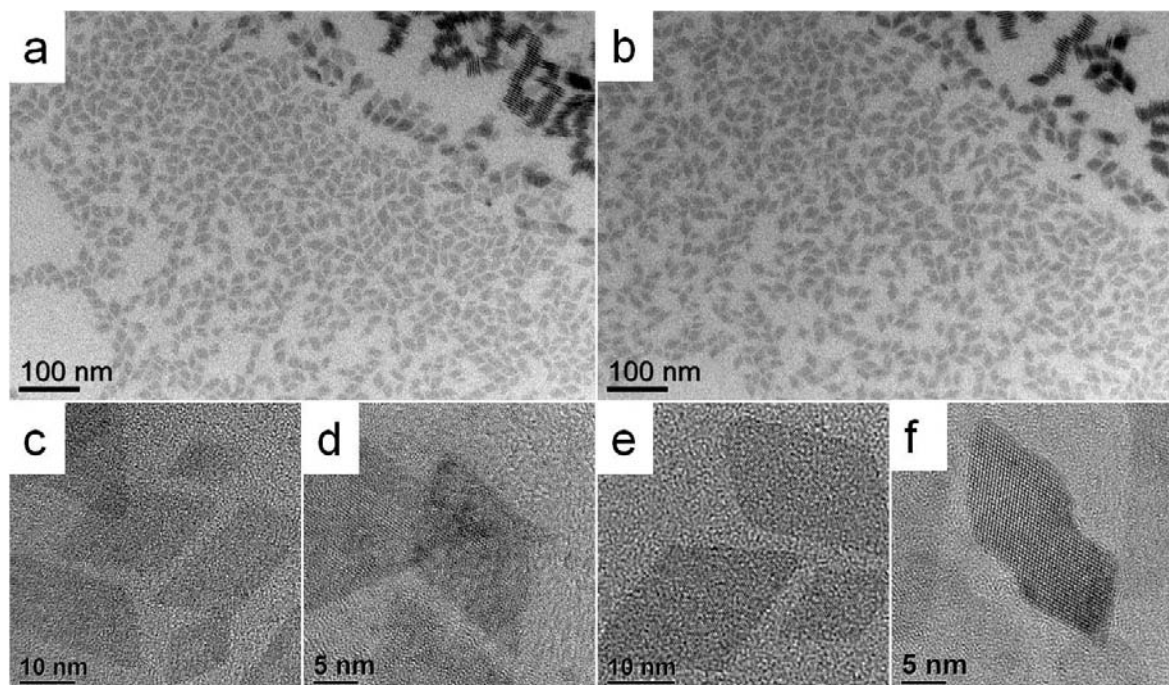


**Figure S11.** (a, b) TEM images and (c-f) HRTEM images of TbF<sub>3</sub> nanoplates synthesized without any lithium salts with a reaction time of 45 min.

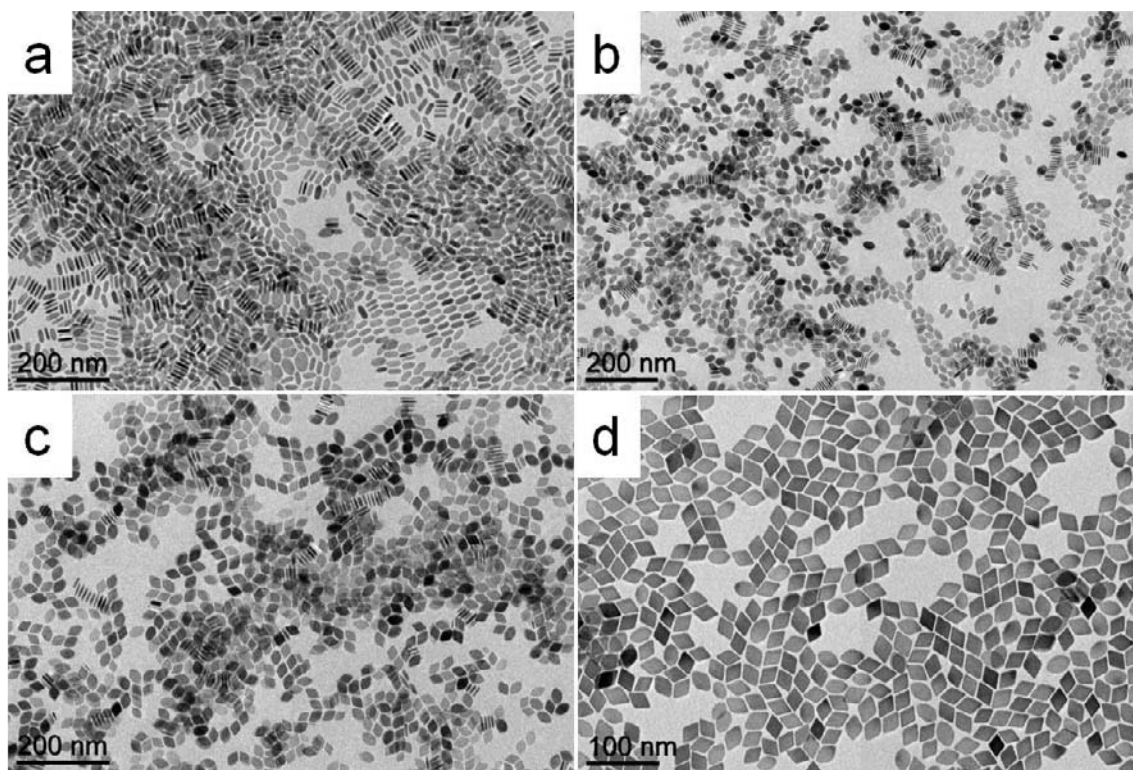


**Figure S12.** TEM images of DyF<sub>3</sub> nanoplates synthesized using 3.372 mmol LiF with reaction times of (a) 15 min, (b) 20 min, (c) 25 min and (d) 30 min.

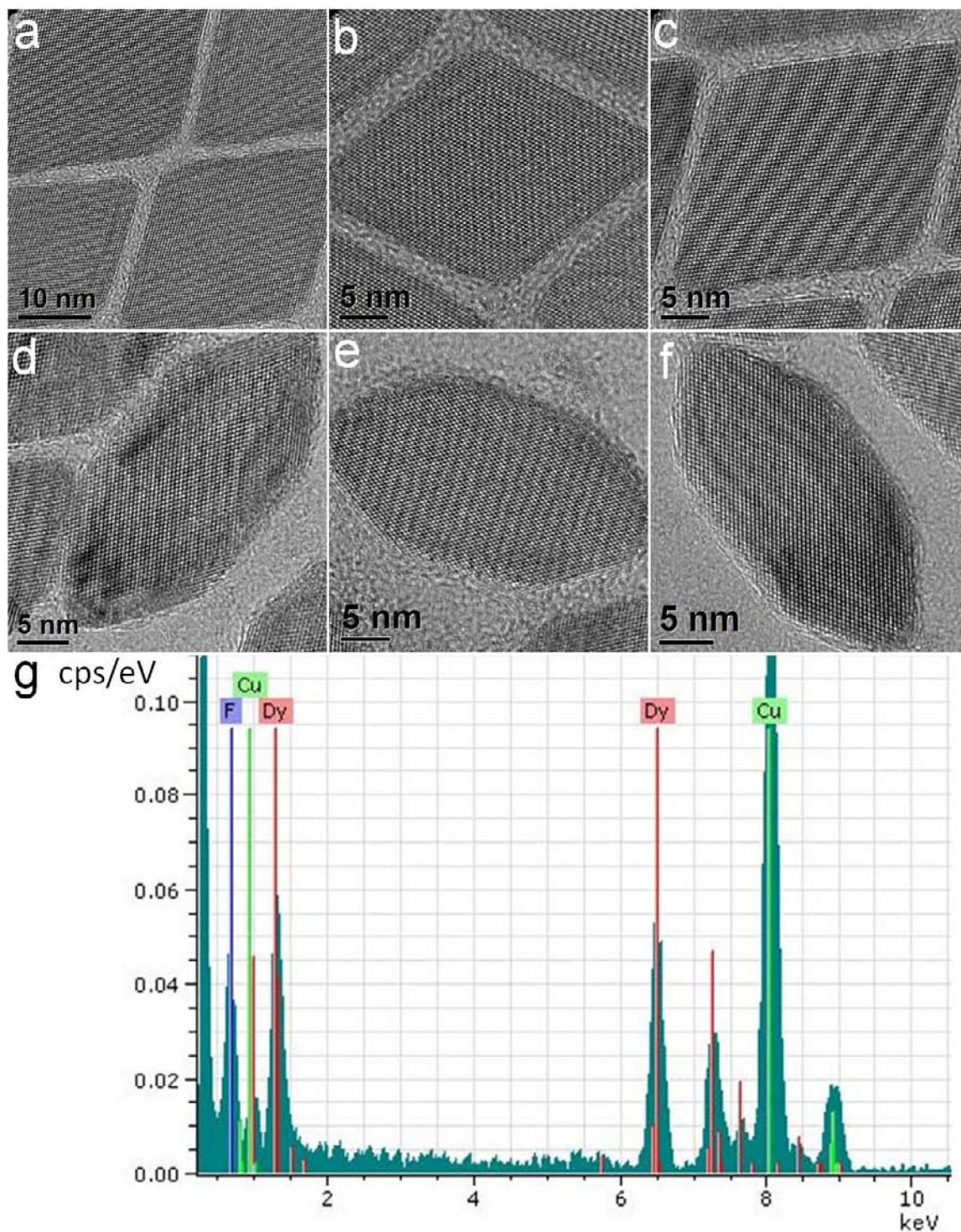


**Figure S13.** (a-c) Additional HRTEM images of DyF<sub>3</sub> nanoplates synthesized using 3.372 mmol LiF with a reaction time of 30 min. (d-f) Additional HRTEM images and (g) EDX spectrum of DyF<sub>3</sub> nanoplates synthesized using 3.372 mmol LiF with a reaction time of 20 min.

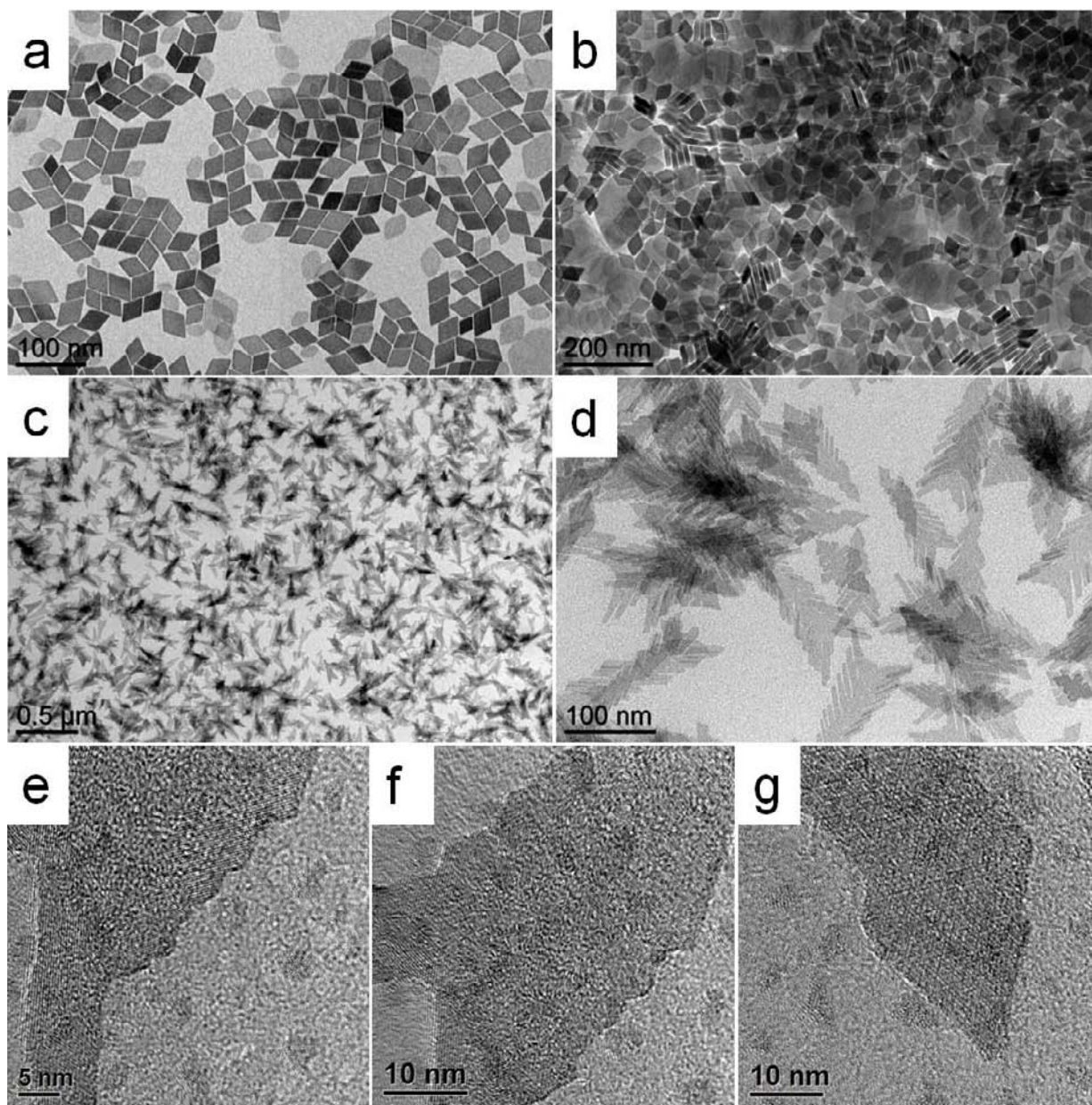


**Figure S14.** (a-b) TEM images of DyF<sub>3</sub> nanoplates synthesized using 5.058 mmol Li(CF<sub>3</sub>CO<sub>2</sub>)<sub>3</sub> with reaction times of 22 min (a) and 45 min (b). (c-d) TEM images and (e-g) HRTEM images of DyF<sub>3</sub> nanoplates synthesized without any lithium salts with a reaction time of 30 min.

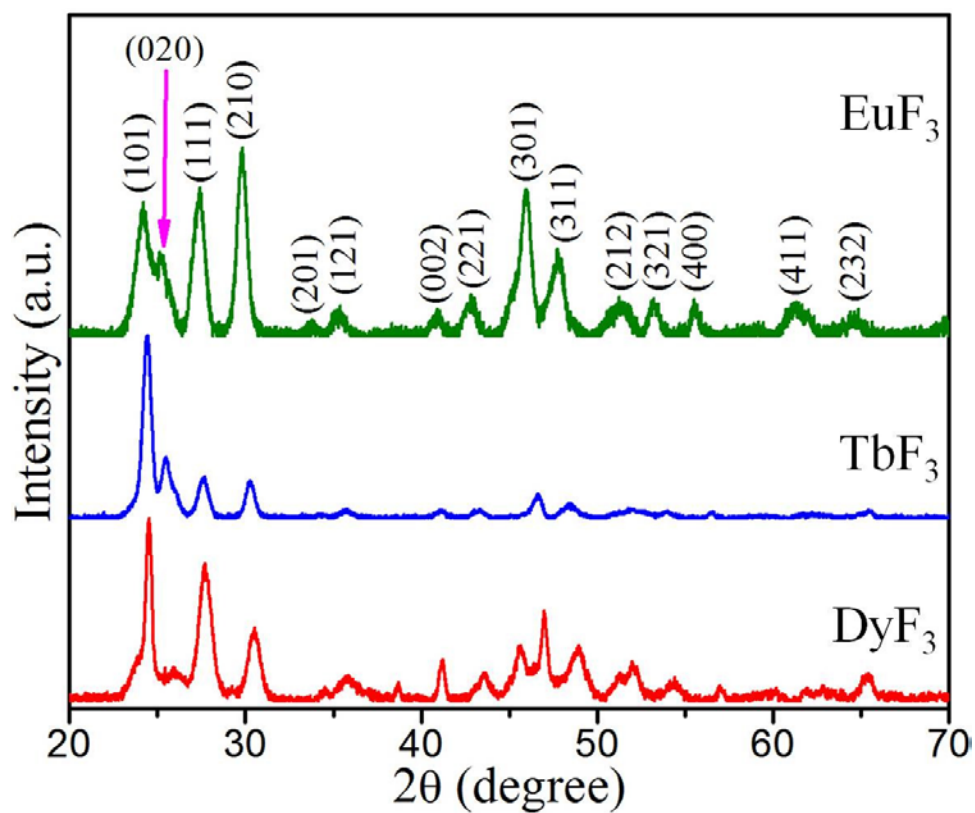


**Figure S15.** Powder XRD patterns of orthorhombic phase EuF<sub>3</sub>, TbF<sub>3</sub> and DyF<sub>3</sub> nanoplates.

## 7. Self-assembled $\text{LnF}_3$ nanoplate superlattices

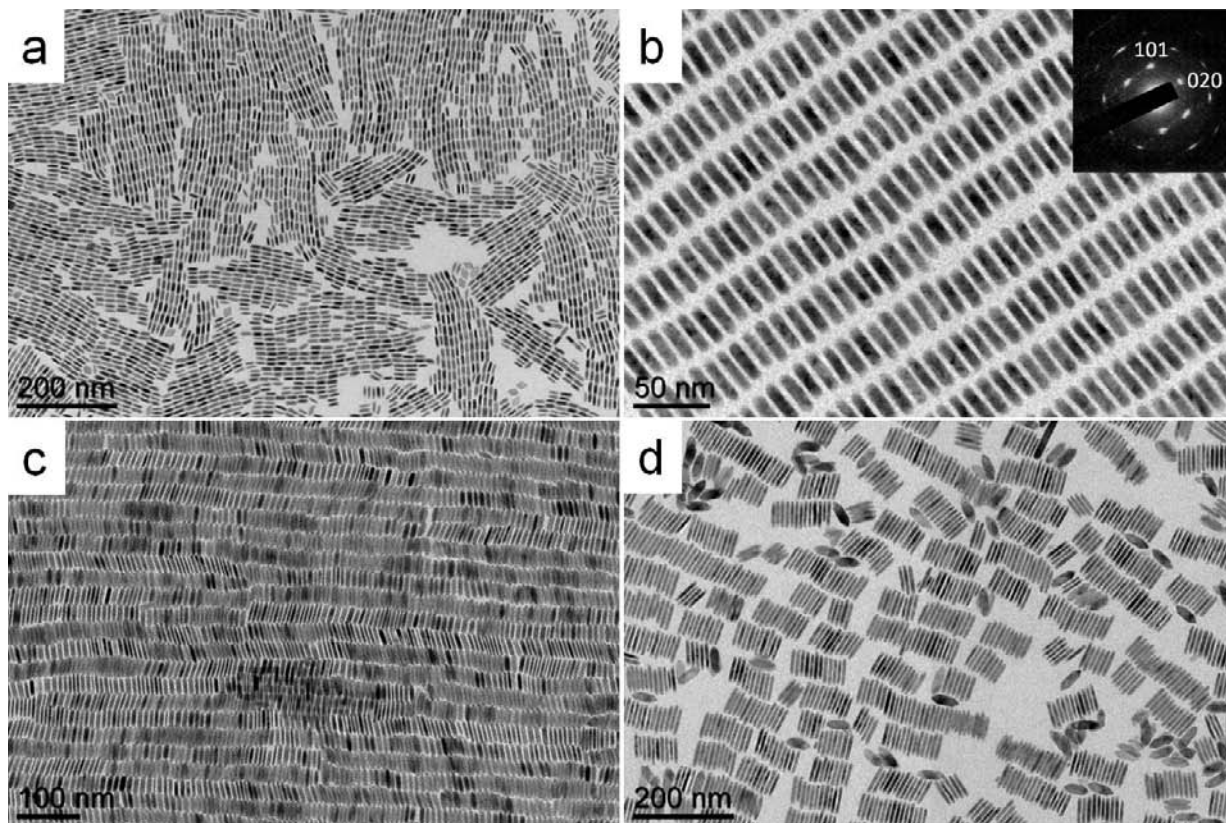


**Figure S16.** TEM images of face-to-face stacking of nanoplates resulting from a higher concentration of nanoplates in the spreading solution. (a)  $\text{DyF}_3$  rhombohedral nanoplates (same sample used for self-assembly of 2D superlattices shown in Figure 2a). (b)  $\text{DyF}_3$  hexagonal nanoplates of an intermediate aspect ratio (same sample used for self-assembly of two-dimensional superlattices shown in Figure 2d). Inset: corresponding wide-angle electron diffraction pattern. (c-d)  $\text{EuF}_3$  hexagonal nanoplates of a large aspect ratio (same sample used for self-assembly of two-dimensional superlattices shown in Figure 2c).

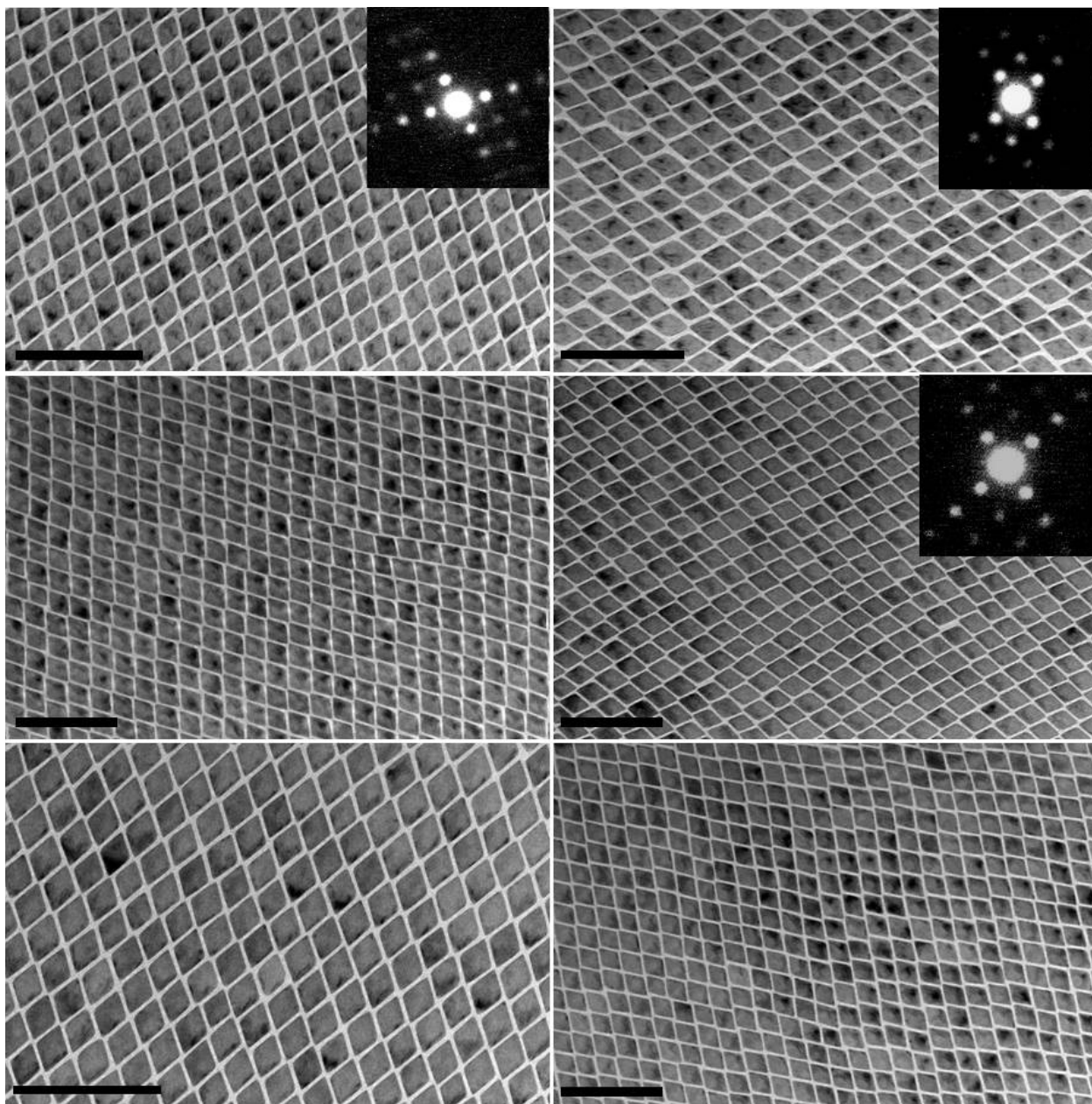


**Figure S17.** Additional TEM images of self-assembled  $\text{DyF}_3$  rhombohedral nanoplate superlattices. Insets are the corresponding small-angle electron diffraction patterns. All scale bars represent 100 nm.

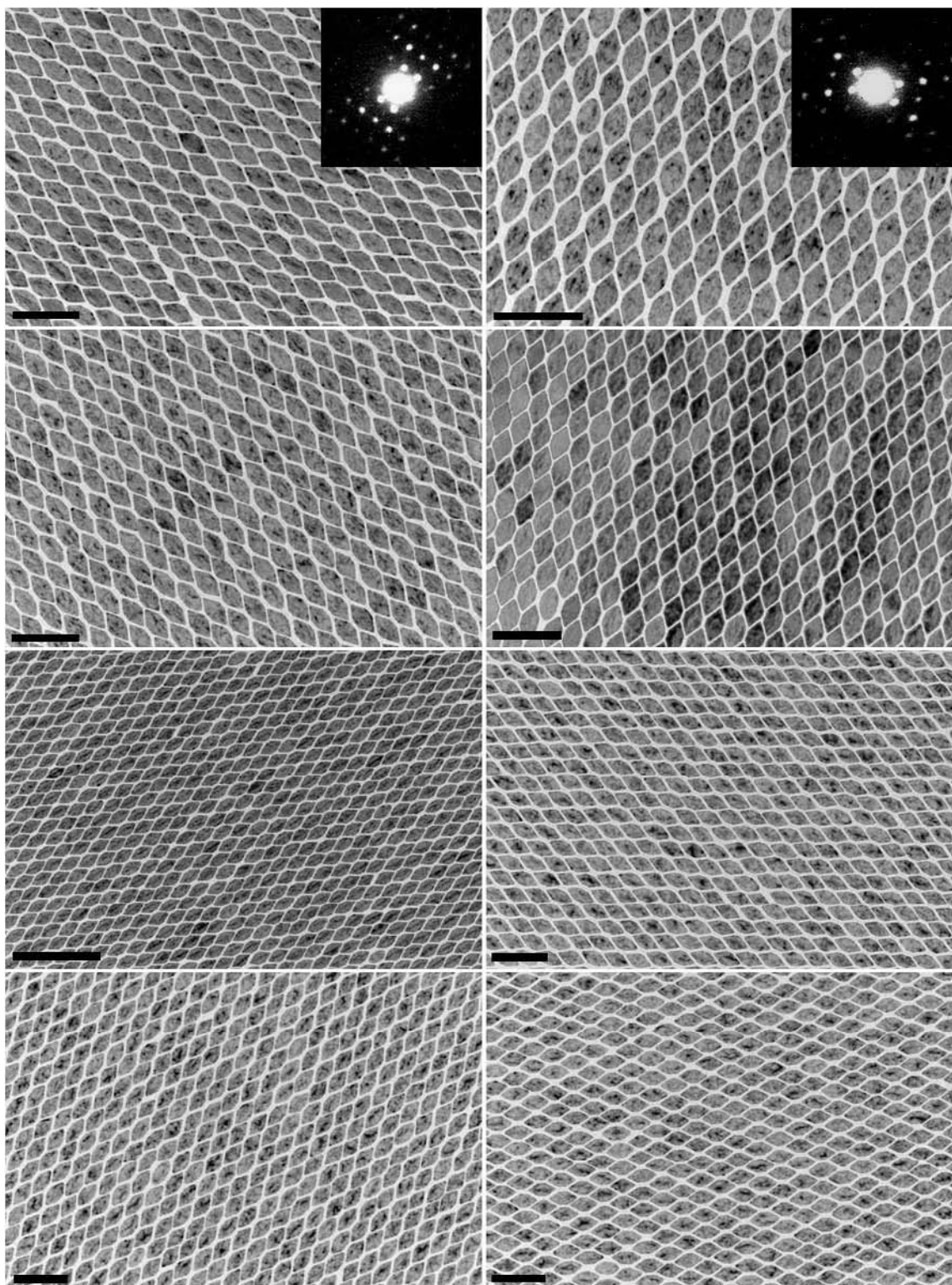


**Figure S18.** Additional TEM images of self-assembled  $\text{TbF}_3$  nanoplate superlattices showing parallel packing. Insets are the corresponding small-angle electron diffraction patterns. All scale bars represent 100 nm.

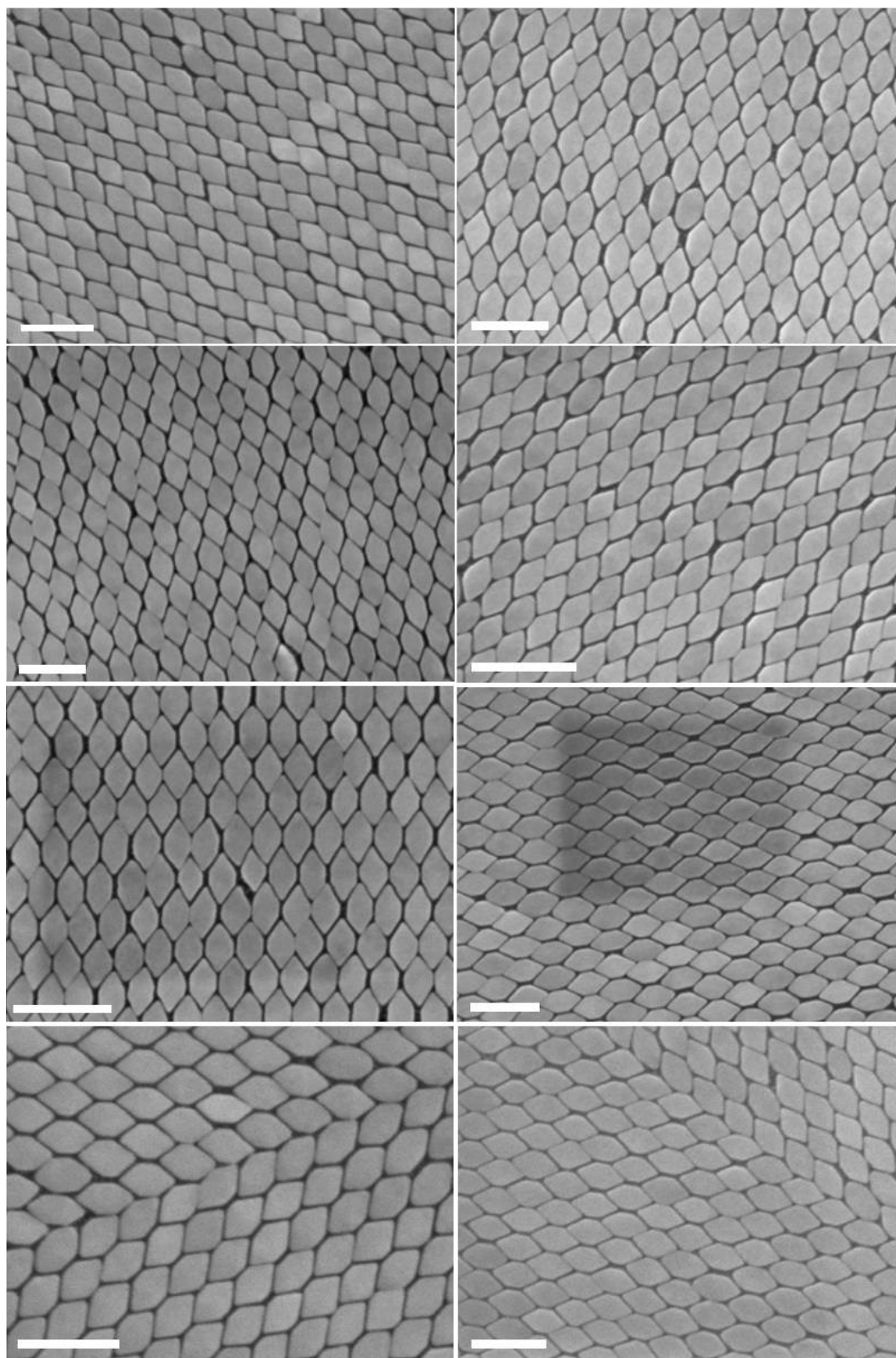


**Figure S19.** HRSEM images of self-assembled  $\text{TbF}_3$  nanoplate superlattices with parallel packing. All scale bars represent 100 nm.

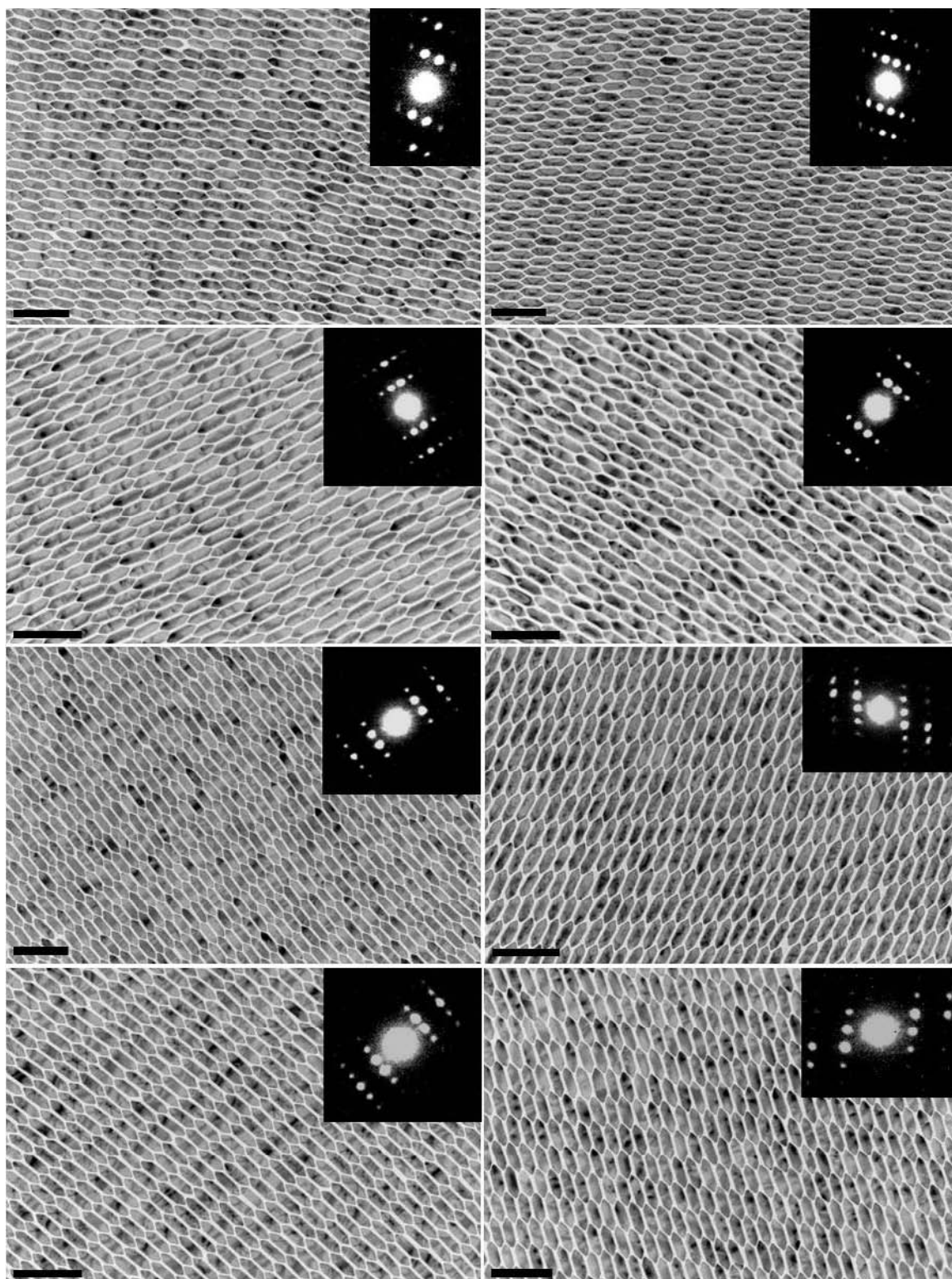


**Figure S20.** Additional TEM images of self-assembled  $\text{EuF}_3$  nanoplate superlattices showing parallel packing. Insets are the corresponding small-angle electron diffraction patterns. All scale bars represent 100 nm.

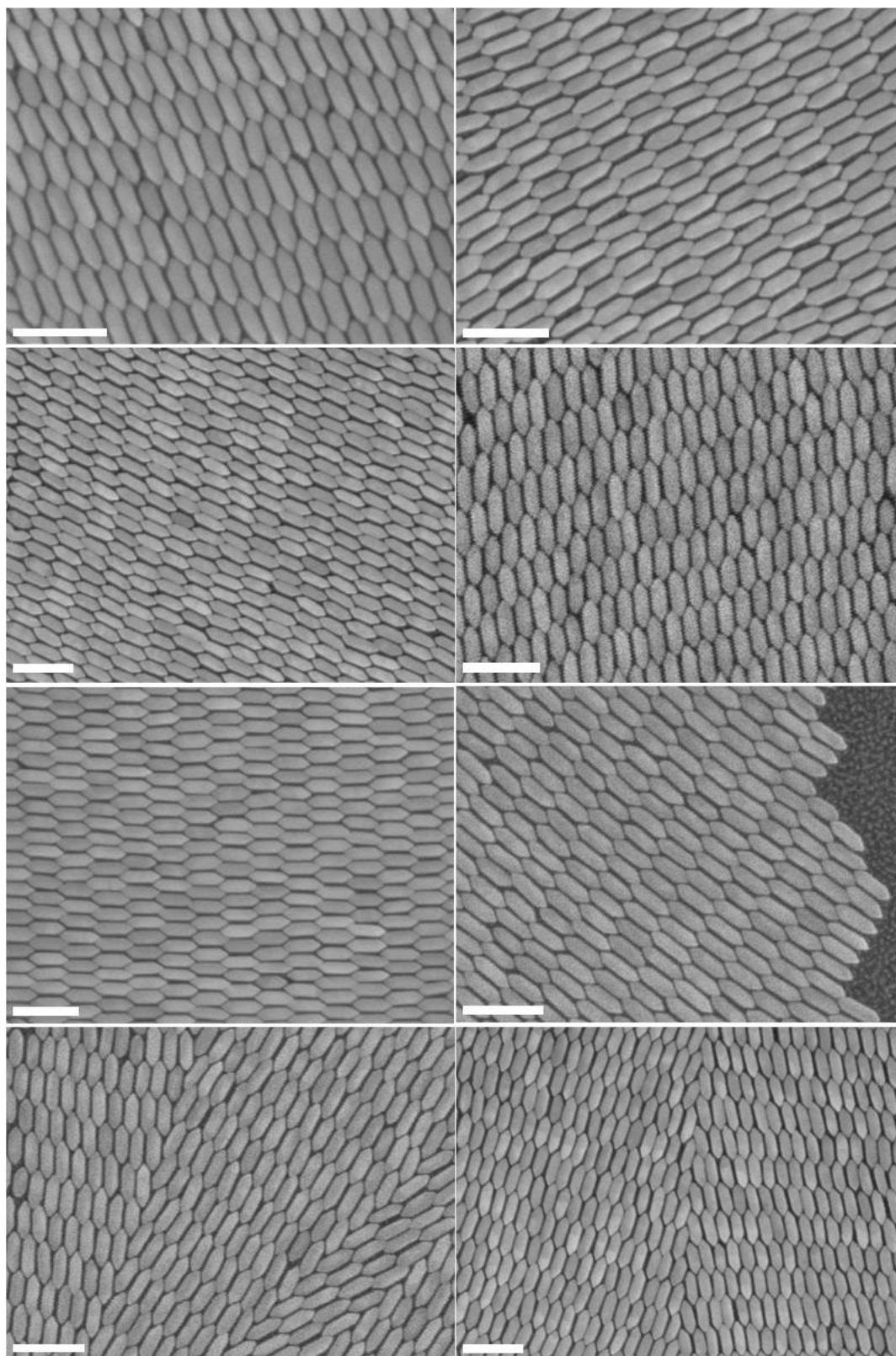


**Figure S21.** HRSEM images of self-assembled  $\text{EuF}_3$  nanoplate superlattices showing parallel packing. All scale bars represent 100 nm.

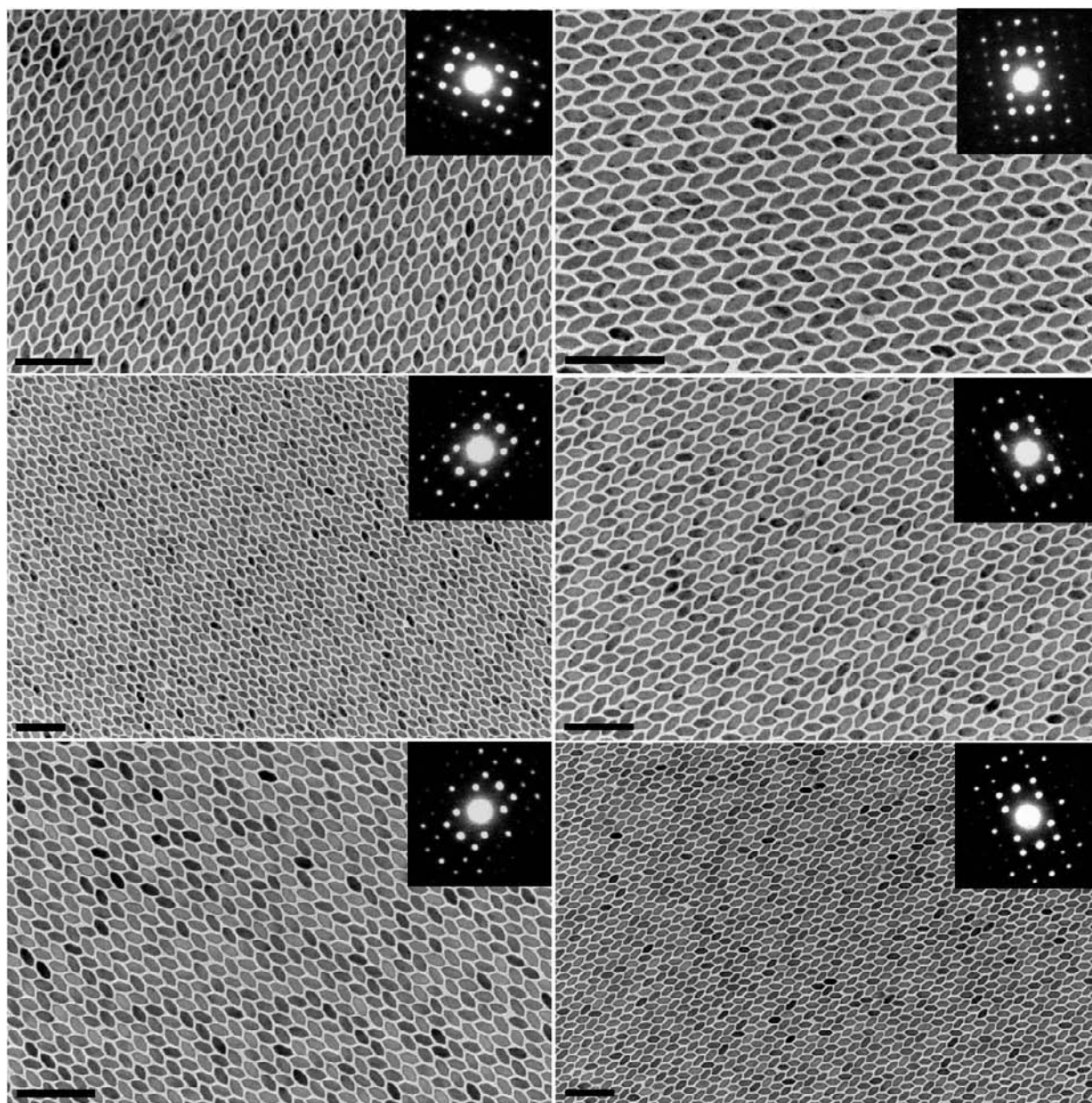


**Figure S22.** Additional TEM images of self-assembled DyF<sub>3</sub> nanoplate superlattices showing alternating packing. Insets are the corresponding small-angle electron diffraction patterns. All scale bars represent 100 nm.

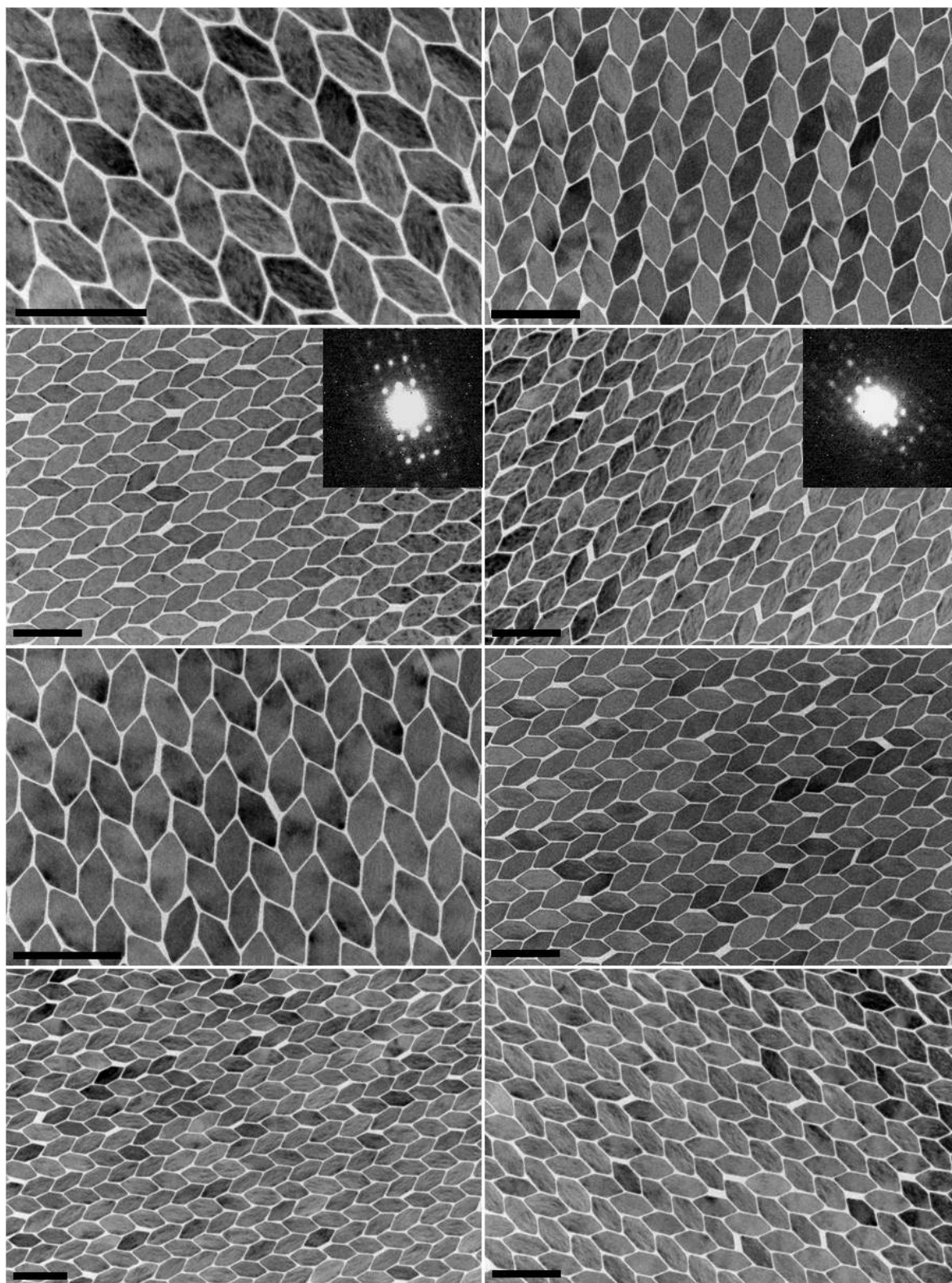


**Figure S23.** Additional TEM images of self-assembled  $\text{TbF}_3$  nanoplate superlattices showing alternating packing. Insets are the corresponding small-angle electron diffraction patterns. All scale bars represent 100 nm.

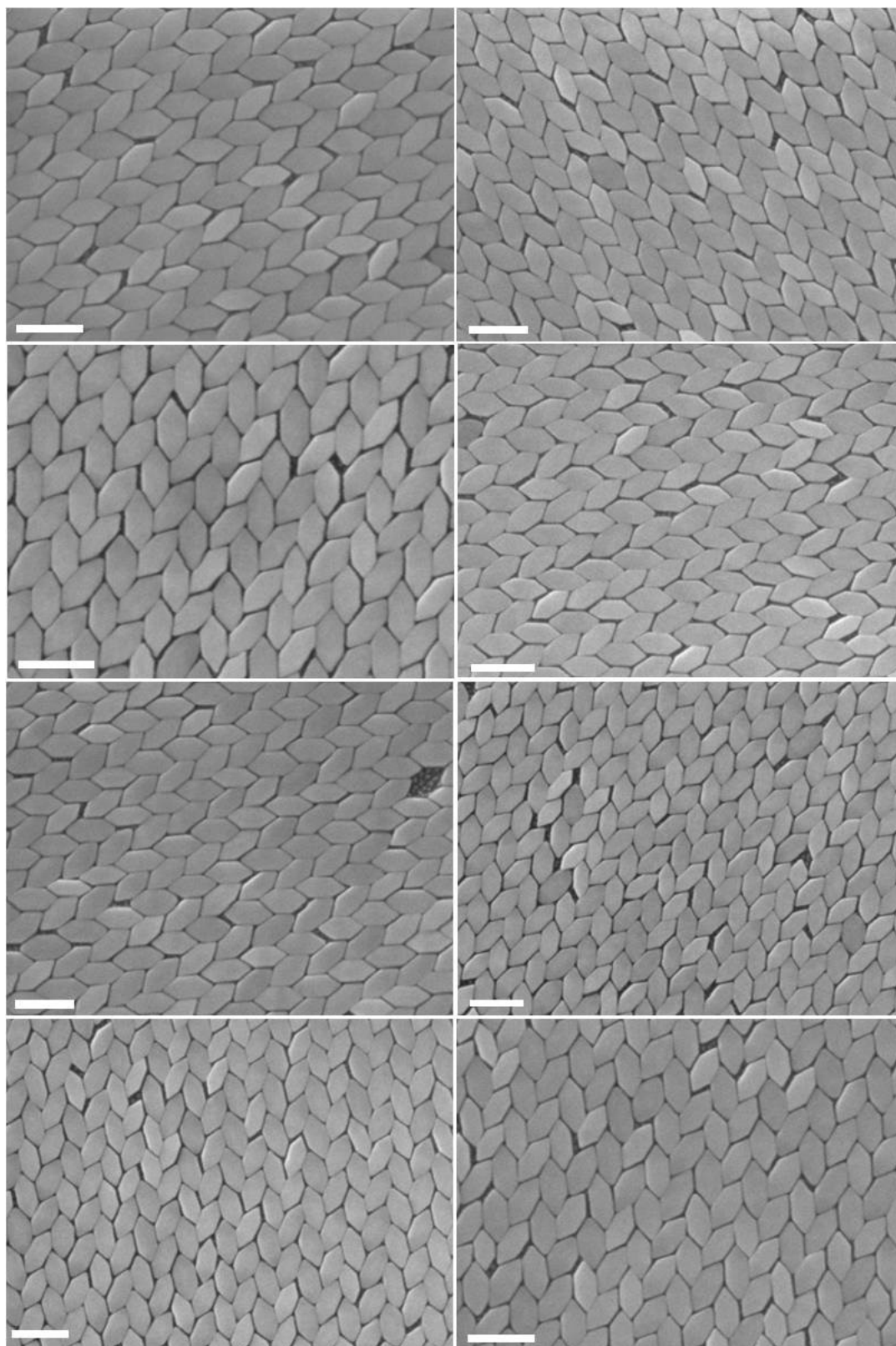


**Figure S24.** HRSEM images of self-assembled  $\text{TbF}_3$  nanoplate superlattices showing alternating packing. All scale bars represent 100 nm.

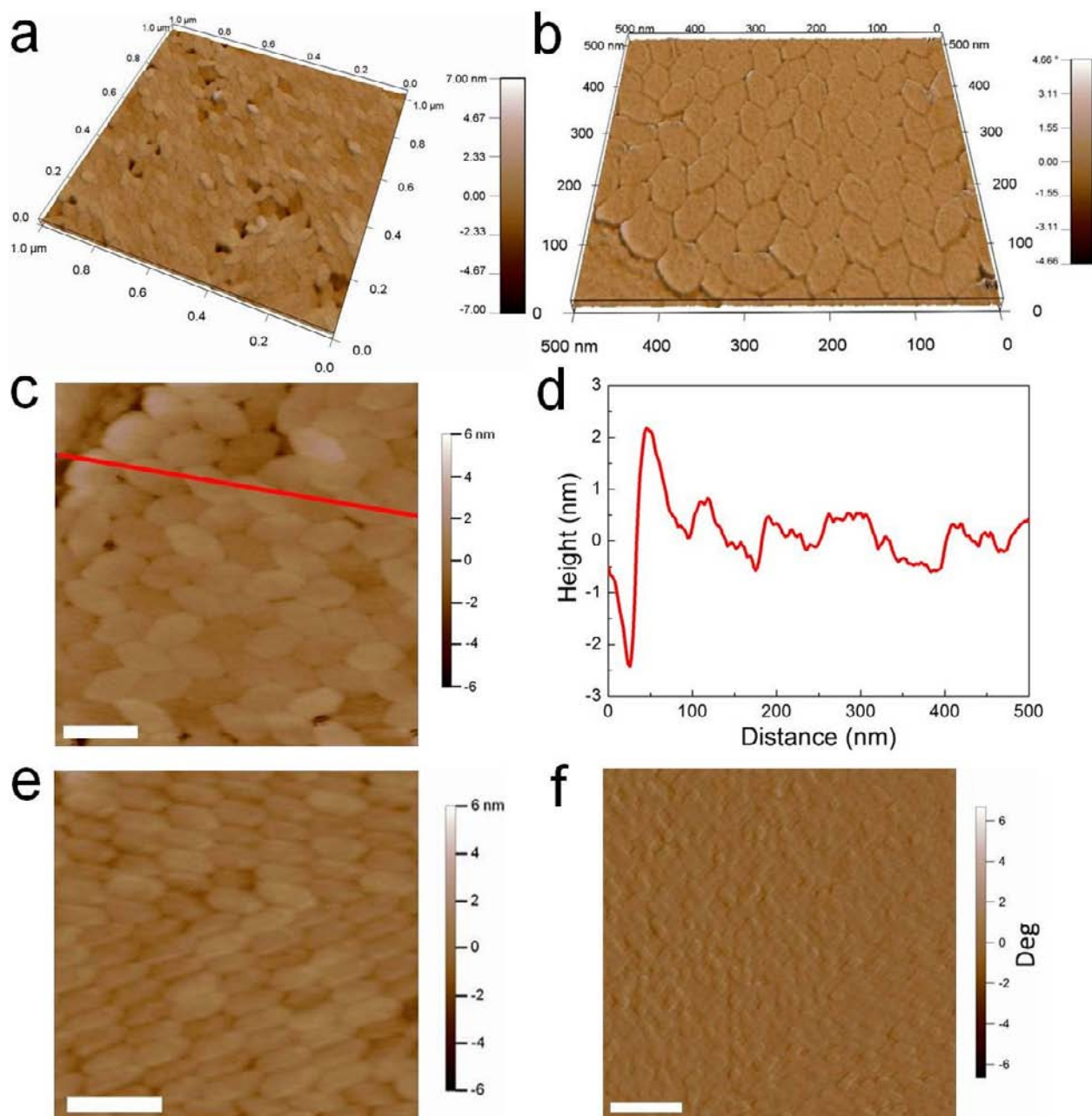


**Figure S25.** Additional AFM images of self-assembled rare earth fluoride nanoplate superlattices. **a-b**, AFM three-dimensional topography images of  $\text{TbF}_3$  nanoplate superlattices showing alternating packing. **c**, AFM height image of  $\text{TbF}_3$  nanoplate superlattices showing alternating packing and **d**, height analysis of the line profile indicated in (c). **e**, AFM height image of a grain boundary in  $\text{EuF}_3$  nanoplate superlattices showing parallel packing. **f**, AFM phase image of self-assembled  $\text{DyF}_3$  rhombohedral nanoplate superlattices. Scan sizes: a)  $1 \mu\text{m} \times 1 \mu\text{m}$ , b)  $500 \text{ nm} \times 500 \text{ nm}$ . Scale bars: c)  $100 \text{ nm}$ , e)  $100 \text{ nm}$ , f)  $200 \text{ nm}$ .

## 8. Monte Carlo simulations and comparison to experiments

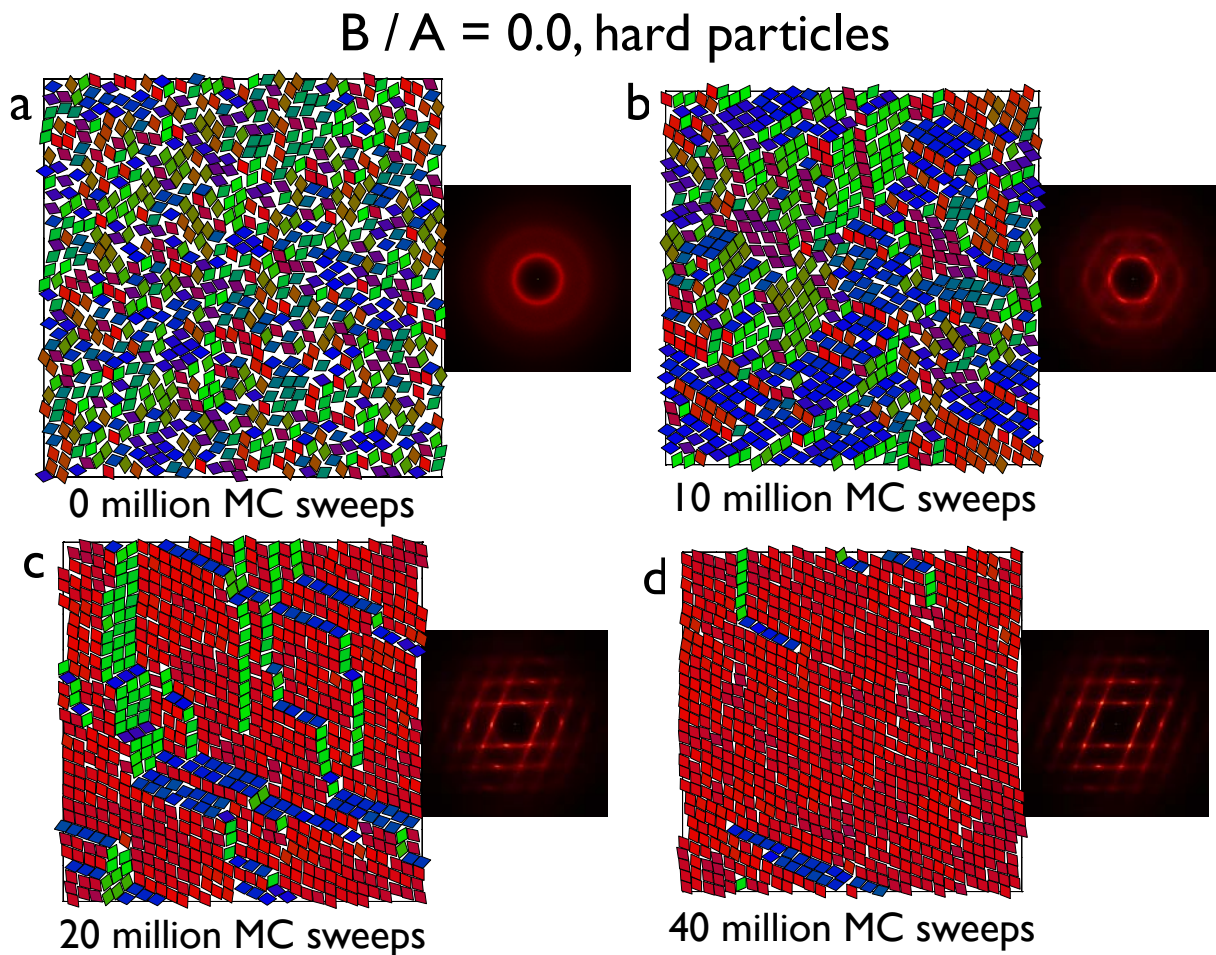


**Figure S26.** Hard rhombs with opening angle  $68^\circ$  assemble into a parallel tiling. Here the pressure is slowly increased during several ten million MC cycles. Starting from the disordered initial state (a) the system orders locally (b). (c) The order slowly grows until most of the rhombs are oriented identically. Worm-like stacking faults are frequently observed. (d) The stacking faults disappear very slowly by rotational jumps of the rhombs. Diffraction images are shown on the right hand sides of the subfigures.

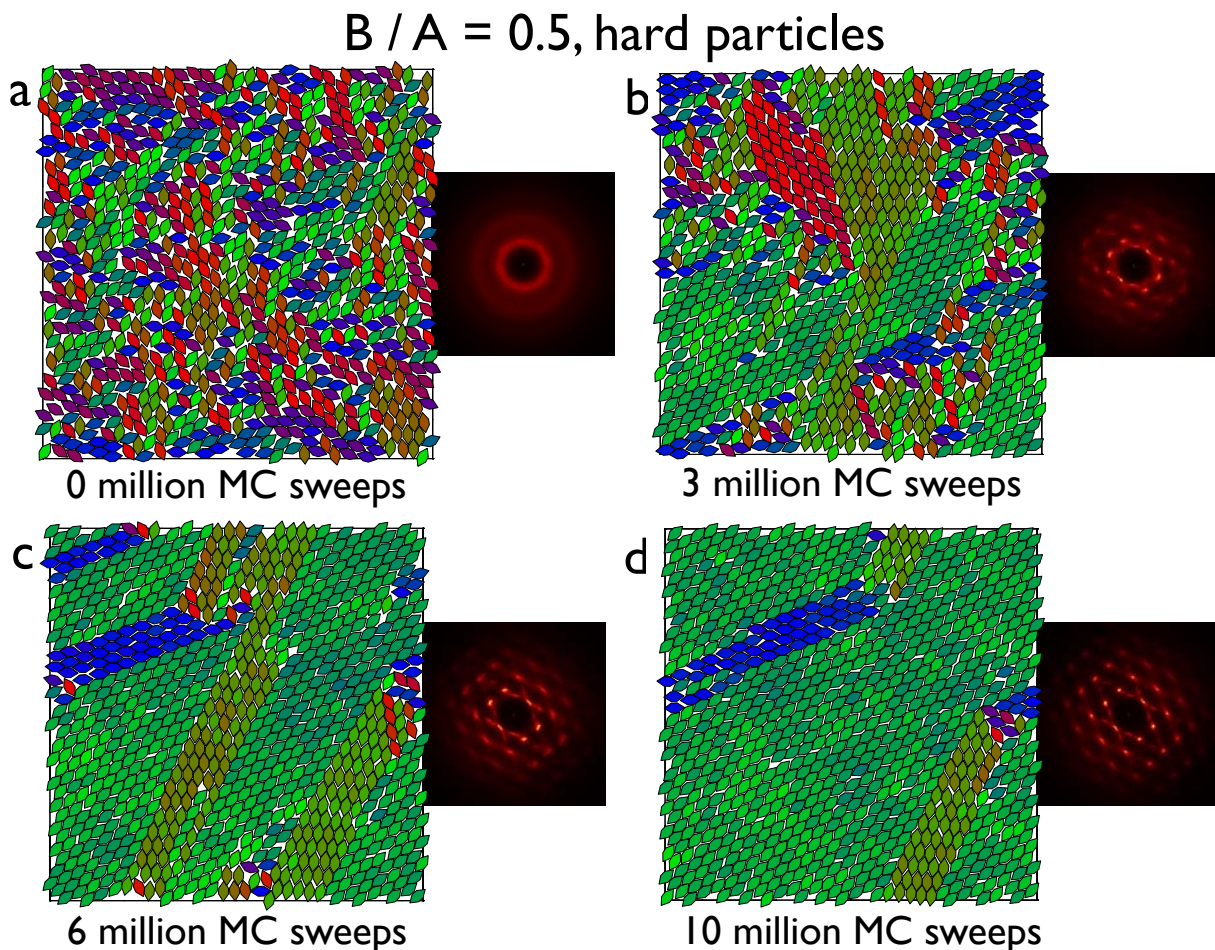


**Figure S27.** The assembly of slightly elongated hard rhombs of irregular hexagonal shape. The irregular hexagons assemble much faster than rhombs, because stacking faults can only occur in connection with small vacancies. The system again forms a parallel arrangement. Growth is fastest along the long symmetry axis of the particles.

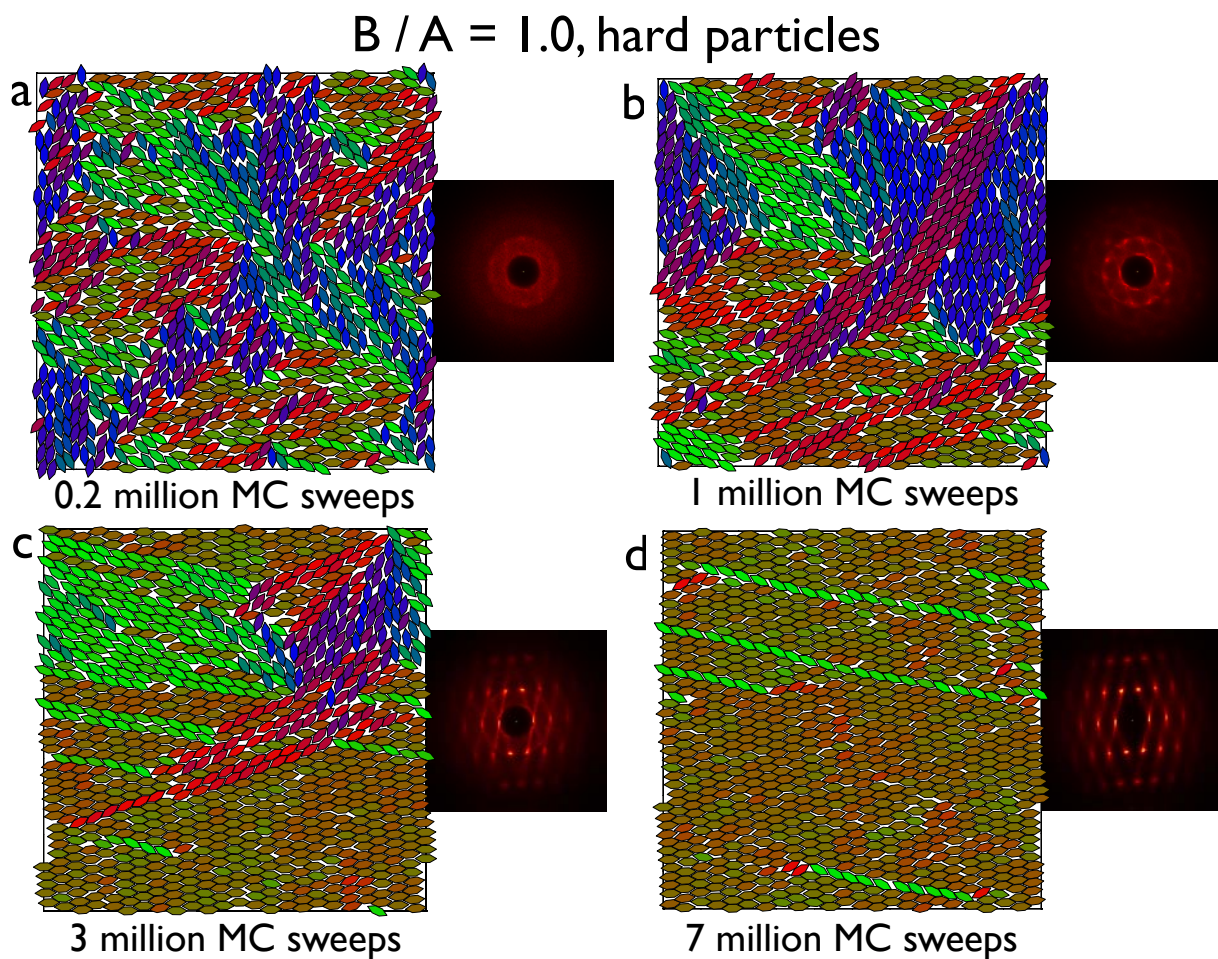


**Figure S28.** Assembly of equilateral elongated rhombs. These irregular particles can assemble equally well into a parallel space-filling tiling or an alternating space-filling tiling. Without interactions, the particles entropically prefer the parallel arrangement. The simulation is run at constant pressure.

$B / A = 2.0$ , hard particles

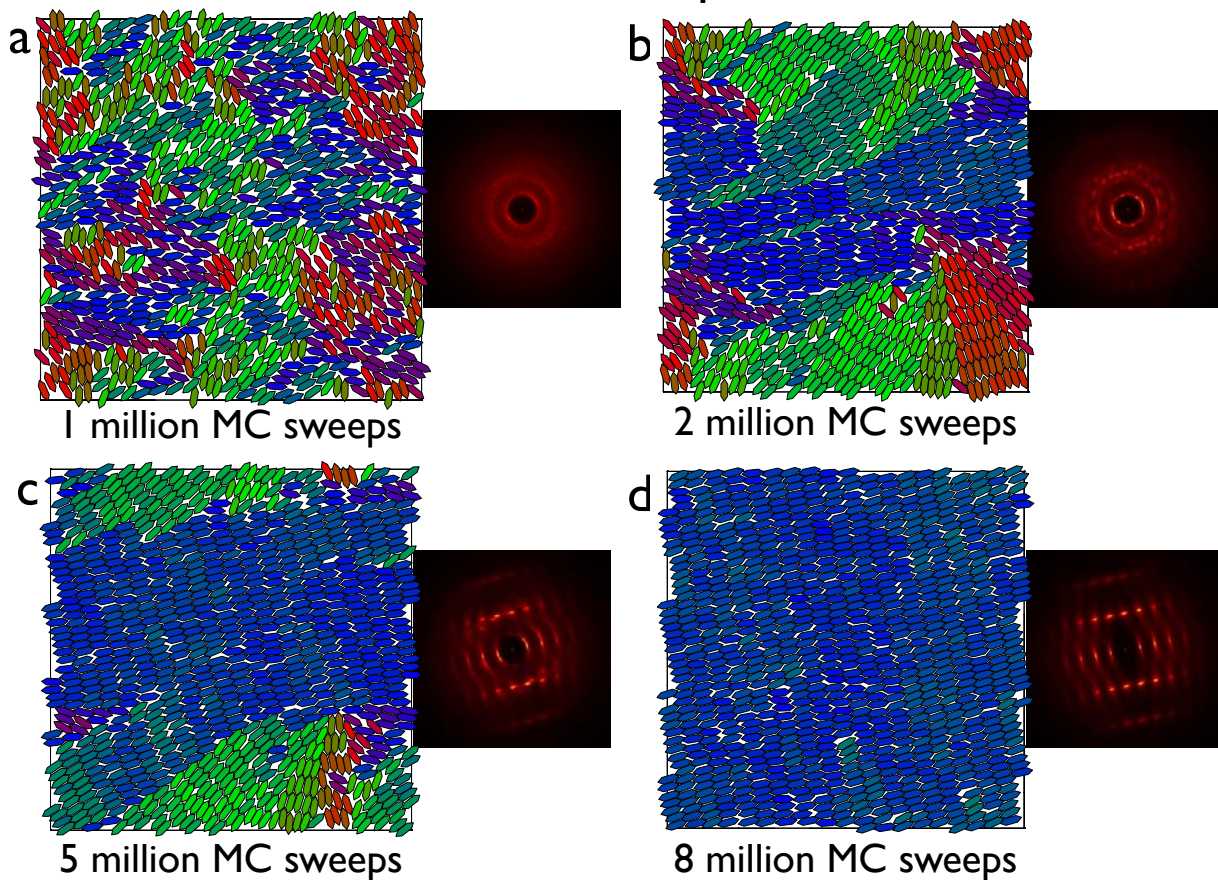


**Figure S29.** Strongly elongated hexagons align quickly (a) and assemble into the parallel pattern. Stacking faults have relatively low angles and single domains can be obtained robustly in simulation.

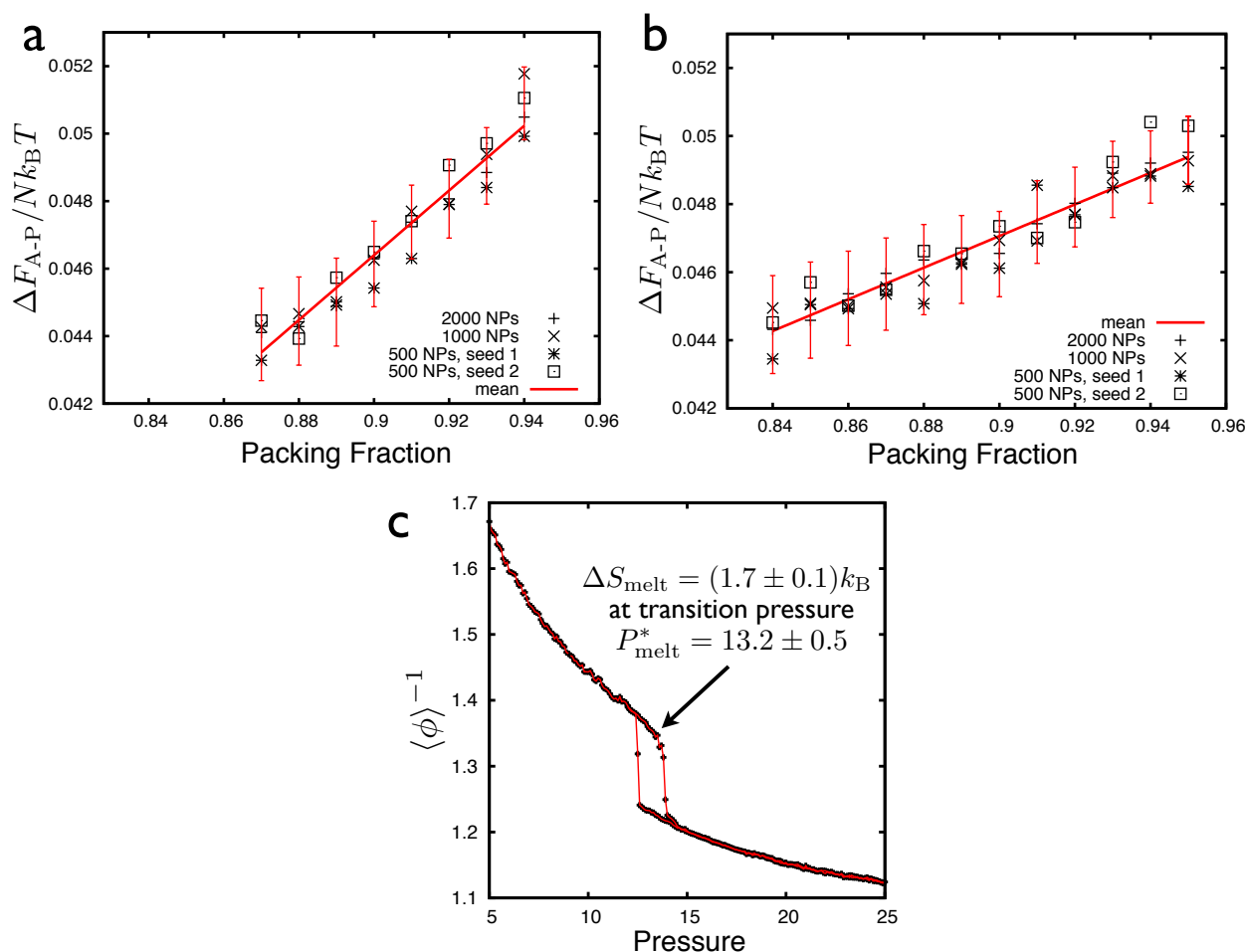


**Figure S30.** (a,b) Free energy difference  $\Delta F_{A-P} = F_{\text{Alt}} - F_{\text{Para}}$  between the alternating and the parallel pattern for hard (a) rhombi with  $B/A = 0$  and (b) equilateral elongated hexagons with  $B/A = 1$ . Both plots show a positive free energy difference, which demonstrates that the parallel arrangement is more stable than the alternating pattern. The free energy difference is in the range  $0.045 \pm 0.015$  over the stability regime of the crystal and increases linearly with packing fraction. Different size initial configurations were chosen to test for finite size effects. The free energy calculation employs the Frenkel-Ladd method. (c) Melting and crystallization curves sketching out the hysteresis around the fluid-solid transition for hard irregular hexagon with  $B/A = 1$ . From the jump in the inverse packing density  $\Delta \phi^{-1}$  and the transition pressure  $P_{\text{melt}}^*$  we estimate the jump in entropy between fluid and solid,  $\Delta S_{\text{melt}} / k_B = P_{\text{melt}}^* \Delta \phi^{-1}$ , to be  $1.7 \pm 0.1$ .

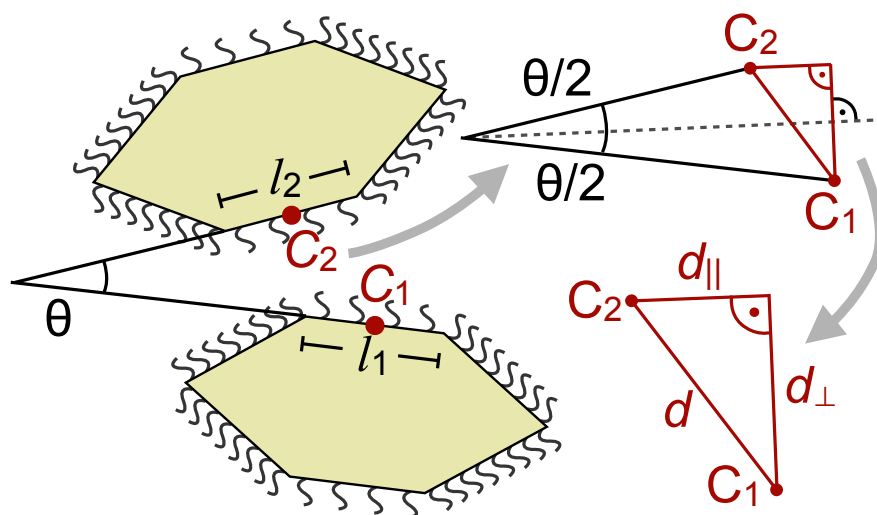


**Figure S31.** Modeling interacting rare earth fluoride nanoplatelets. Oleic acid tethers cause an effective interaction of nanoplatelet edges. The interaction strength depends on the orientation angle  $\theta$ , the shift  $d_{\parallel}$  parallel to the bisector of the two edges, and the normal distance  $d_{\perp}$  perpendicular to the bisector.

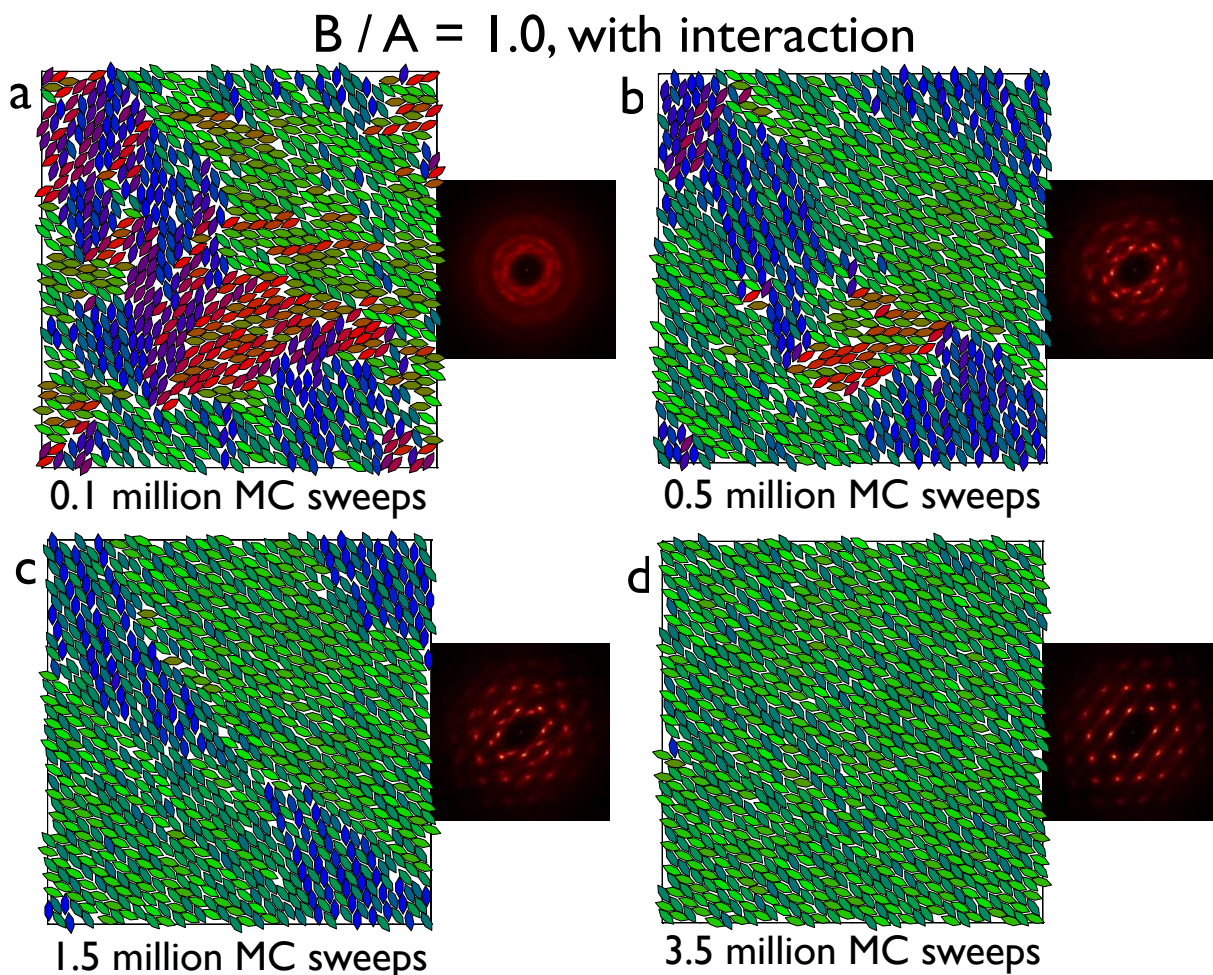


**Figure S32.** Equilateral elongated rhombs with an interaction that prefers the alternating tiling (b). The attraction between edges of different type (A-B) is stronger than the attraction between edges of the same type (A-A and B-B) as observed in the experimental systems of  $\text{LnF}_3$  nanoplates. Interaction speeds up the assembly compared to the hard systems. Between (c) and (d) the biggest crystalline grain takes over the whole simulation box. Note that in (d) one stacking fault still remains. This stacking fault cannot heal because of the periodic boundary conditions.

$B / A = 1.0$ , with interaction

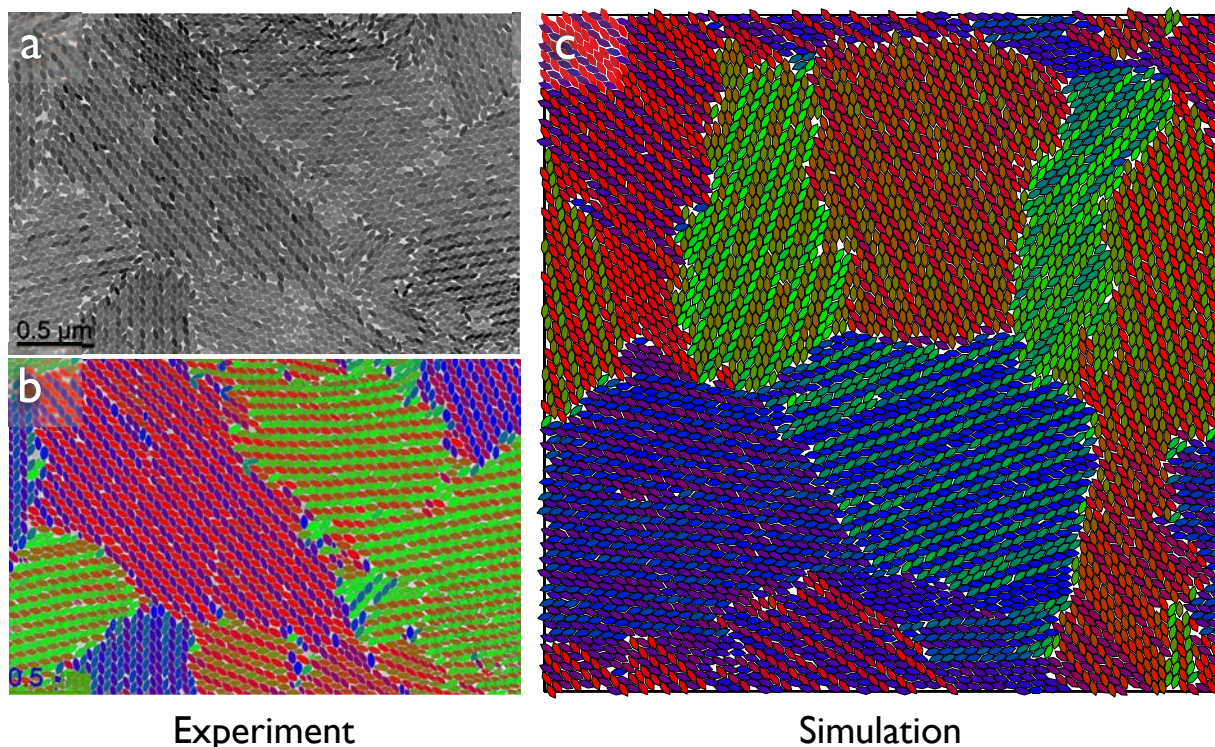


**Figure S33.** (a) TEM image of a multicrystalline state of  $\text{TbF}_3$  plates. (b) Coloring the plates based on their orientation using image analysis tools helps identifying coexisting grains. The plates assemble robustly into the alternating tiling. Note that impurities are abundant on the grain boundaries. (c) In the simulation of a large system (5000 particles), the formation of multiple grains with alternating patterns was also observed. This figure is a larger version of the subfigures 5i,k,l of the main text.

$B / A = 0.0$ , with interaction

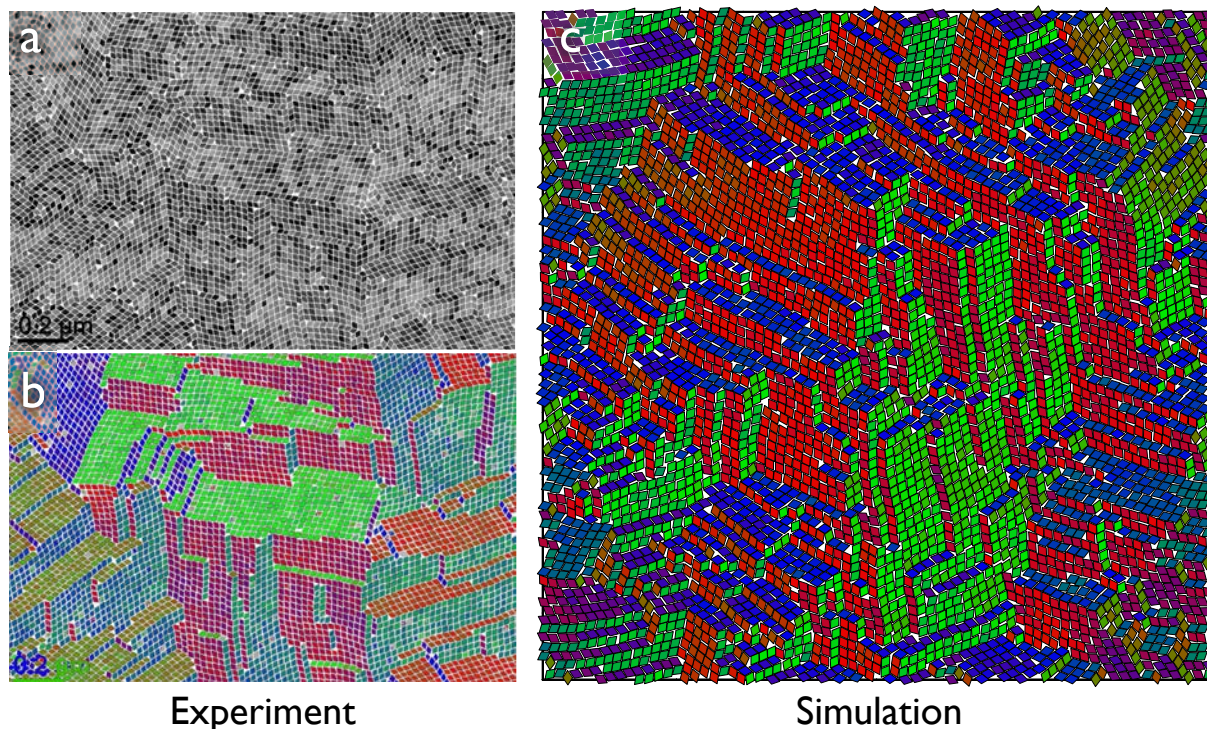


**Figure S34.** Comparison of experiment (a,b) and simulation in a larger system of interacting rhombs (c). (a) The TEM image shows the existence of multiple grains. (b) The experimental image is colored with an image analysis code. The orientation of rhombs is detected automatically by determining the inertia tensor. A clear tendency for forming parallel arrangements can be observed. (c) A large (5000 rhombs) simulation with interacting rhombs. The interaction makes it harder for the rhombs to crystallize. This figure is a larger version of the subfigures 5f,g,h of the main text.

## 9. Additional results from DFT calculations

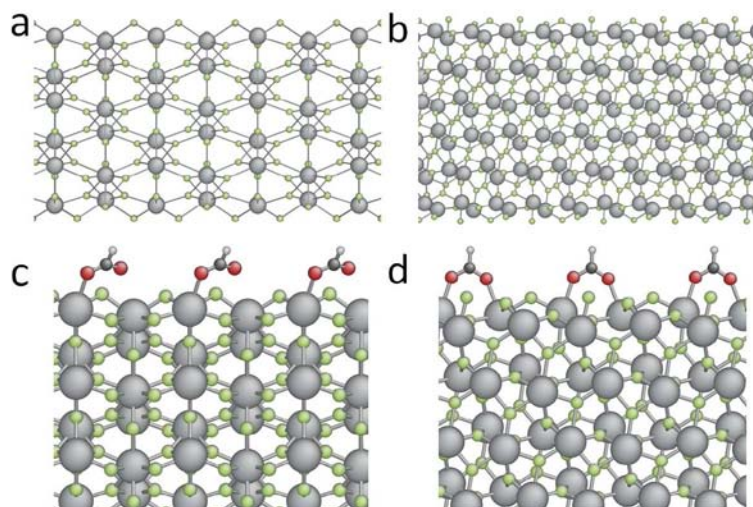


**Figure S35.** (a,b) Atomic structures of pristine DyF<sub>3</sub> (001) surface (a) and (101) surface (b) in side view. (c,d) Atomic structures of DyF<sub>3</sub> (001) surface (c) and (101) surface (d) with adsorbed HCOO (Grey: Dy. Green: F. Black: C. Red: Oxygen. White: H).

## 10. Experimental results for particle forces and interactions

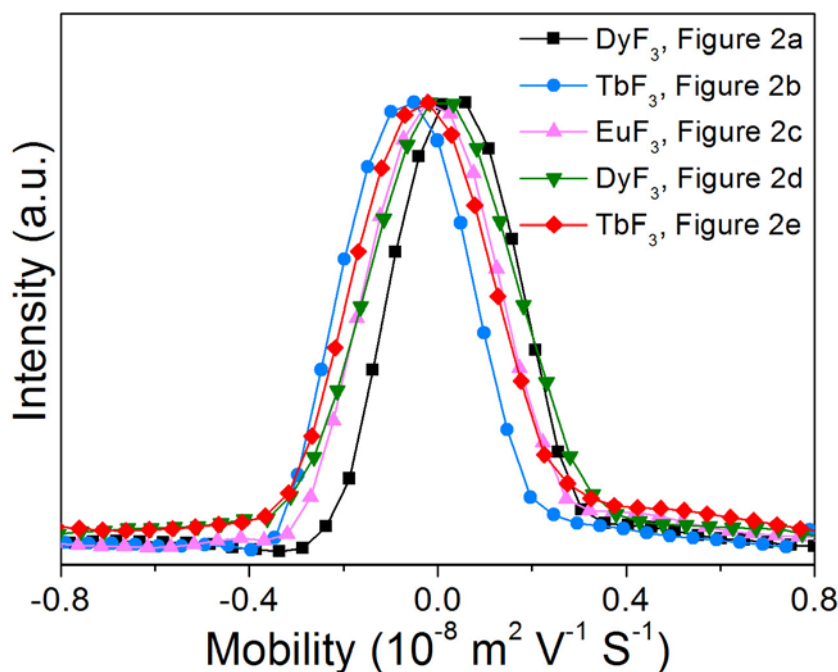


**Figure S36.** Electrophoretic mobility measurements of rare earth fluoride nanoplates performed in hexane solutions. We obtain a maximum peak mobility of  $-0.07 \times 10^{-8} \text{ m}^2 \text{ V}^{-1} \text{ s}^{-1}$  (blue curve), which can safely be attributed to be ‘nearly neutral’. The small charge only introduces a very weak repulsive interaction, much weaker than the attraction in the oppositely-charged sub-10nm spherical nanoparticle mixture that forms binary superlattices<sup>11</sup>. In light of the electrophoretic mobility results, we believe that Coulomb interactions can be excluded as a major driving force for assembly.

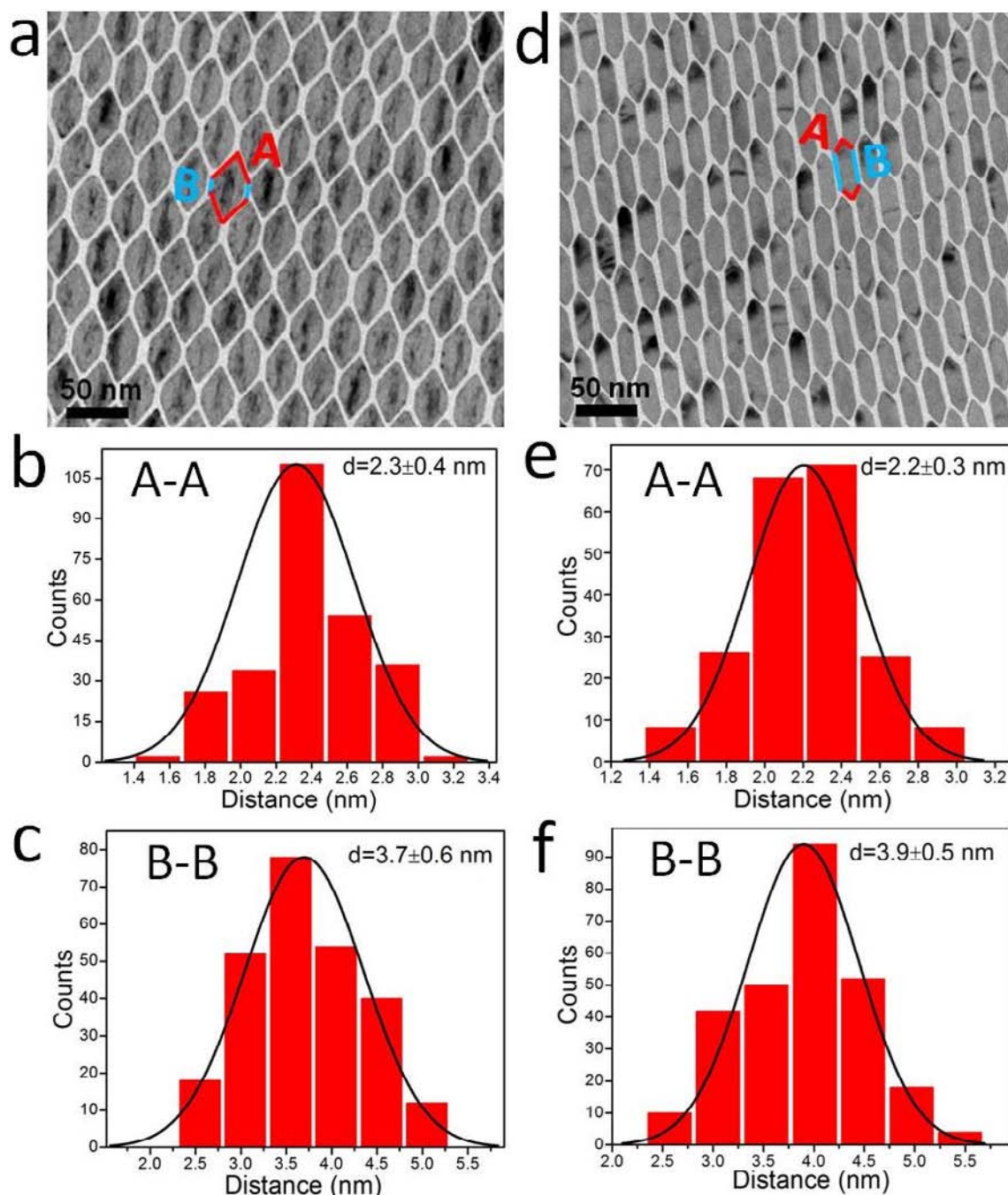


**Figure S37.** Representative TEM images of (a) TbF<sub>3</sub> and (d) EuF<sub>3</sub> nanoplate superlattices and the corresponding (b, c and e, f) statistical analysis of interparticle distance. “A” denotes {101} facets and “B” denotes {002} facets. For each histogram, at least two hundred measurements are carried out. It is noteworthy that in both parallel configurations, A-A separation is much smaller than B-B separation.

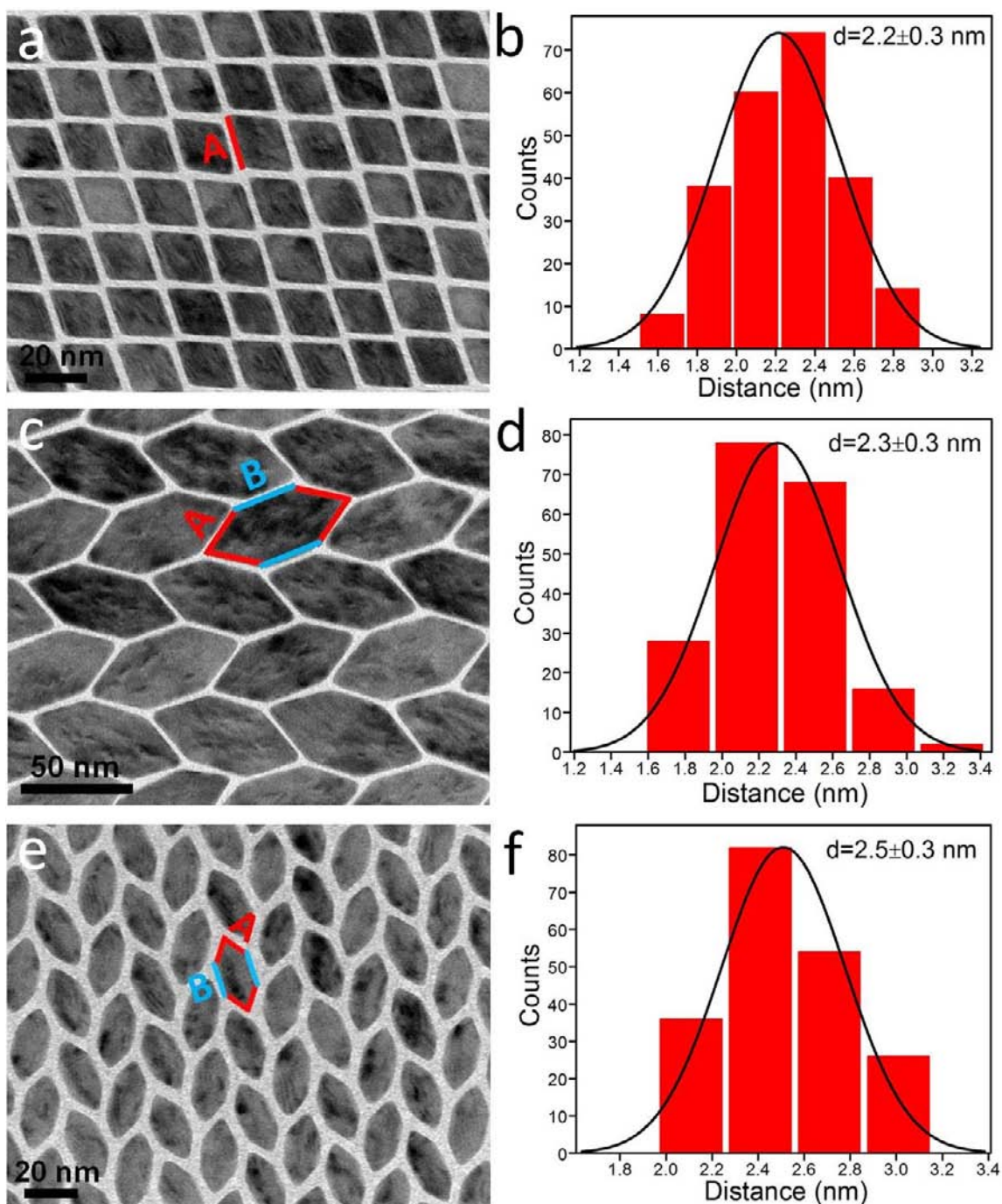


**Figure S38.** Representative TEM images of (a) DyF<sub>3</sub> rhombohedral nanoplate, (c) TbF<sub>3</sub> nanoplate and (e) DyF<sub>3</sub> nanoplate superlattices and the corresponding (b, d and f, respectively) statistical analysis of interparticle distance. “A” denotes {101} facets and “B” denotes {002} facets. For each histogram, at least two hundred measurements are carried out. It is noteworthy that in both alternating configuration (c and e), each nanoplate is surrounded by nearly uniform interparticle separations (2 A-A contacts and 4 A-B contacts).

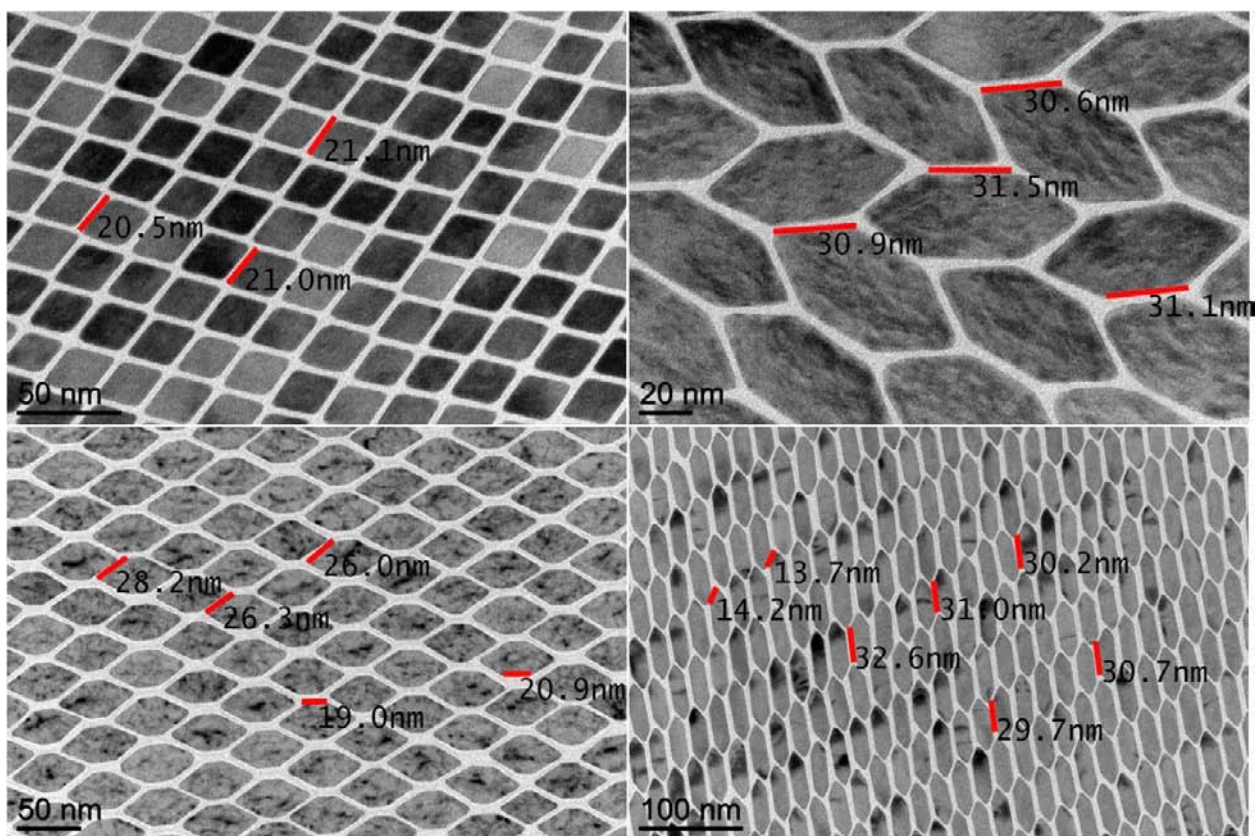


**Figure S39.** Typical values for the contact edge lengths of the nanoplates range from 13 nm to 33 nm, depending on the exact shape of the nanoplates as well as their packing configuration.